THE UNIVERSITY *of* EDINBURGH

Acoustic tomography imaging for atmospheric temperature and wind velocity field reconstruction

Yong Bao

A thesis submitted for the degree of Doctor of Philosophy

The University of Edinburgh

June 2019

Declaration

I hereby declare that the research recorded in this thesis and the thesis itself was composed and originated entirely by myself in the School of Engineering at The University of Edinburgh.

Acknowledgements

First of all, I would like to express my sincere gratitude to my supervisor, Dr Jiabin Jia, for his support and guidance throughout my PhD research. He had a very active role in my research and gave me the freedom to explore and take the work in new directions. His encouragement and suggestions gave me the confidence to progress my own academic career. It has been an absolute privilege to work with him during the challenging doctoral period.

I also want to thank my assistant supervisor, Dr Nick Polydorides, for his valuable suggestions and help on my PhD project. I have learned a lot from his profound knowledge of signal processing and inverse problem techniques.

Many thanks go to my colleagues in the Agile Tomography Group. I am especially grateful to Dr Yunjie Yang, Hancong Wu and Dr Shengheng Liu for their inspiration and advices about tomographic image reconstruction algorithms. I also want to say a big thank you to Dr Hao Wu for his kind suggestions during the development of the acoustic tomography system. Similar, profound gratitude goes to Dr Dimitris Kamilis, Dr Alex Tsekenis and Dr Taweechai Ouypornkochagorn for their valuable advices and continuous help.

I gratefully acknowledge the funding received towards my PhD from the School of Engineering.

Last but not least, I would like to express my deepest gratitude and best wishes to my family. Special thanks go to my parents for their love, encouragement and support.

Lay Summary

Acoustic tomography is an imaging technique to visualize the internal structure of the sensing area based on time-of-flight (TOF) measurements. Compared to other sensing techniques, acoustic tomography has the advantage of non-invasive nature, fast imaging speed, low equipment cost, scalability for a variety of measurement range, and ability to simultaneously monitor the temperature and wind velocity fields. Therefore, it has been widely used in various applications including seismic imaging, ocean currents monitoring, forestry, industrial processing tomography, and meteorology for the atmospheric imaging of the temperature and wind velocity fields.

This thesis aims to improve the reconstruction quality of the acoustic tomography system for temperature and wind velocity fields imaging. Focusing on this goal, the thesis demonstrates the design and implement of acoustic tomography, from the perspective of data collection system development, robust and accurate TOF estimation method, high-quality scalar and vector tomographic image reconstruction methods for temperature and wind velocity fields respectively. Their performance will be validated through simulation and experimental study.

Contents

List of Figures

List of Tables

Abbreviations

ADMM-Alternating direction method of multipliers

AI-Analogue input

AO-analogue output

AIC-Akaike Information Criterion

AR-Autoregressive

CLB-Cramer-Rao lower bound

CT-Computer tomography

DAQ-Data acquisition

ERT-Electrical resistance tomography

FBS-Forward–backward splitting

FFT-Fast Fourier Transform

FMM-Fast marching method

GUI-Graphical user interface

IHT-Iteratively hard thresholding

ISTA-Iterative shrinkage-thresholding algorithms

KLT-Karhunen Louve transform

LIDAR-Light detection and ranging

MAP-Maximum a posteriori

MER-Modified energy ratio

MLS-Maximum Length Sequence

MSFM-Multistencils fast marching method

NCGD-Nonlinear conjugate gradient descent

NGD-Nonlinear gradient descent

NI-National instrument

OTRR-Online time-resolved reconstruction

PAIK-Phase arrival identification-kurtosis

PCAIC-Phase corrected AIC TOF estimation

PCB-Printed circuit board

RBF-Radial basis function

rRMSE-Relative root mean square error

SIRT-Simultaneous iterative reconstruction technique

SI-Stochastic inversion

SNR-Signal to noise ratio

SODAR-Sound detection and ranging

STA/LTA-Short and long-time averaged ratio

TDSI-Time-dependent stochastic inversion

TOF-Time-of-Flight

TSVD-Truncated singular value decomposition

TV-Total variation

WGN-White Gaussian Noise

List of symbols

τ -Time of flight (TOF)

$\mathbb{u}$ -Group velocity of sound wave

$\mathbf{c}_L$ -The Laplace sound speed

$\mathbf{s}_L$ -The Laplace sound speed slowness

$\mathbb{v}$ -Wind velocity

γ -Ratio of specific heats for ideal gas

R -Gas constant

$\mathbf{T}$ -Temperature

N -Number of pixels

M -Number of measurements

$\mathbf{A} \in \mathbb{R}$ -The ray length matrix for temperature reconstruction

$\mathbf{S} \in \mathbb{R}$ -The ray length matrix for wind velocity reconstruction

λ -Regularization parameter

μ -Step size

MS/s- Mega samples per second

Publication List

Journal papers

1. Bao, Y. and Jia, J. (2019) Improved time-of-flight estimation methods for acoustic tomography system, IEEE Transactions on Instrumentation and Measurement, doi: 10.1109/TIM.2019.2908704.

2. Bao, Y. and Jia, J. (2019) Online time-resolved reconstruction method for acoustic tomography system, IEEE Transactions on Instrumentation and Measurement, doi: 10.1109/TIM.2019.2947949.

3. Bao, Y. Jia, J. and Polydorides, N. (2017) Real-time temperature field measurement based on acoustic tomography, Measurement Science and Technology, Vol. 28, pp. 1-12.

Book chapter

1. Bao, Y. and Jia, J. (2018) Chapter 8: Real-time Wind Velocity Monitoring based on Acoustic Tomography, Geological Disaster Monitoring Based on Sensor Network, Editors: Durrani, Tariq S, Wang, Wei, Forbes, Sheila (Eds.), Published by Springer Singapore, ISBN 978-981-13-0992-2.

Conference papers

1. Bao, Y. and Jia, J (2018) Temperature Field Reconstruction based on Acoustic Travel-time Tomography, 9th World Congress on Industrial Process Tomography, Bath, UK, 2-6 September 2018.

2. Bao, Y. and Jia, J. (2017) Nonlinear temperature field reconstruction using acoustic tomography, 2017 IEEE International Conference on Imaging Systems and Techniques, Beijing, China, 18-20 October 2017.

3. Bao, Y., Jia, J. and Polydorides, N. (2016) Simulation study of temperature field reconstruction based on acoustic tomography, 8th

World Congress on Industrial Process Tomography, Iguassu Falls, Brazil, 26-29 Sep 2016.

Abstract

Owing to its non-invasive nature, fast imaging speed, low equipment cost, scalability for a variety of measurement ranges, and ability to simultaneously monitor both temperature and wind velocity fields, acoustic tomography has attracted considerable interest in the field of atmospheric imaging. This thesis aims to improve the reconstruction quality of the acoustic tomography system for temperature and wind velocity field imaging. Focusing on this goal, the contribution of the thesis can be summarised from the perspectives of data collection system development, robust and accurate TOF estimation method, and high-quality scalar and vector tomographic image reconstruction methods for temperature and wind velocity fields respectively. Details are given below.

Firstly, in order to facilitate the experimental study of acoustic tomography imaging, the design and evaluation of the data collection system and TOF estimation method was presented. The evaluation results indicate that the presented data acquisition system and TOF estimation method has good quantitative accuracy in the lab-scale experiments.

The temporal resolution is of great significance for the real-time monitoring of the fast-changing temperature field. To improve the temporal resolution, a novel online time-resolved reconstruction (OTRR) method is presented, which can reconstruct high quality time-resolved images by using fewer TOFs per frame. Compared to state-of-the-art dynamic reconstruction algorithms such as the Kalman filter reconstruction, the proposed algorithm demonstrated superior spatial resolution and preferable quantitative accuracy in the reconstructed images. These features are necessary for the real-time monitoring of the fast-changing temperature field.

The forward modelling of most acoustic tomography problems is based on a straight ray model, which may result in large modelling errors due to the refraction effect under a large gradient temperature field. In order to reduce the inaccuracy of using the straight ray model, a bent ray model and nonlinear reconstruction algorithm is applied, which allows the sound propagation ray

paths and temperature distribution to be reconstructed iteratively from the TOFs.

Using acoustic tomography to reconstruct large-scale temperature and wind velocity fields, a fully parallel TOF measurement scheme is necessary. To achieve this goal, a set of orthogonal acoustic waveforms based on the filtered and modulated Kasami sequence is designed and a cross-correlation based TOF estimation method is used for data collection. Besides, to overcome the invisible field problem and improve the image quality of the wind velocity reconstruction, a divergence-free regularised vector tomographic reconstruction algorithm is studied. The proposed method is able to provide accurate tomographic reconstruction of the 2D horizontal wind velocity field from the TOF measurements.

In summary, this thesis focuses on the improvement of acoustic tomography techniques for temperature and wind velocity fields, including the phase corrected Akaike information criterion (AIC) TOF estimation for accurate and robust TOF estimation, the online time-resolved reconstruction method for real-time monitoring of the fast changing temperature field, the nonlinear reconstruction based on the bent ray model to reconstruct the temperature field with a large gradient, and the divergence-free regularised reconstruction method to visualise the 2D horizontal wind velocity field.

Chapter 1 Introduction

1.1 Background and motivation

The principle of acoustic tomography is similar to that of X-ray computed tomography (CT), which is to send acoustic signals through the sensing area and visualise the internal structure based on the corresponding interactions with the received signals. There are three major interactions amenable to acoustic measurements: including the sound speed, the attenuation, and the scattering [1]. Among these interactions, the sound speed distribution is the most critical property, which can be reconstructed based on acoustic Time-of-Flight (TOF) measurements. With a small number of acoustic sensors placed around the sensing area, multiple TOF measurements along different acoustic propagation ray paths can be used for the tomographic reconstruction of the 2D or 3D sound speed distribution.

Acoustic tomography has proved to be an effective sensing technique for a variety of applications. Relevant cases include the large scale ocean currents [2-5], the seismic imaging of the geometrical properties of the subsurface at depth [6], medical ultrasound imaging for breast cancer detection [7-11], the non-destructive testing for tree decay detection [12] and stored grain deterioration detection [13].

In addition to these applications, acoustic tomography also gains a great deal of interest in atmospheric imaging to monitor the temperature and wind velocity distributions of air. Reported research on atmospheric imaging based on acoustic tomography includes the atmosphere vertical temperature structure monitoring using acoustic waves from powerful explosions on the ground [14, 15], the horizontal temperature and wind velocity field monitoring of the near surface atmosphere [16, 17], the indoor climate monitoring system [18-21], and the furnace or boiler temperature field monitoring system [22-24].

Among all the acoustic tomography application areas, the work described in this thesis mainly focuses on exploiting the acoustic tomography technique for atmospheric imaging, including the large-scale (from tens to several hundred metres) wind velocity imaging system, the small-scale (from several metres to tens metres) and lab-scale (within 1 metre) air temperature imaging system.

There are several efforts in developing robust and accurate temperature and wind velocity measurement techniques. For the non-invasive temperature measurement device, laser-based techniques, such as the Rayleigh scattering technique with the aid of particle image velocimetry and laser Doppler velocimetry, have the disadvantages of being expensive and difficult to be implemented. Passive optical tomography with a multi-camera tomography system is able to provide non-invasive 3D flame monitoring and characterization on laboratory scale furnaces with good spatial resolution. However, it also requires the object to be luminous and translucent in order to get the side view measurements [25]. For the wind velocity measurement, SODAR (SOund Detection And Ranging) and LIDAR (LIght Detection And Ranging), the two remote sensing techniques which both employ the Doppler effect to acquire wind observations, have the disadvantages of being expensive, relatively power hungry [26] and difficult to implement for small scale measurement setups. Despite its advantages of having a non-intrusive nature, high-speed, and low equipment cost, acoustic tomography has two major benefits compared to other temperature and wind velocity measurement techniques: (1) acoustic tomography is one of few techniques that can deliver accurate quantitative estimation results of the temperature and wind velocity fields simultaneously; and (2) acoustic tomography has a scalable sensing area, which ranges from a few metres to hundreds of metres.

1.2 Aims and objectives

Aiming at improving the performance of acoustic tomography for the atmospheric imaging of temperature and wind velocity fields, the primary targets of this thesis are to develop robust and accurate TOF estimation algorithm, scalar tomographic reconstruction algorithm for temperature field

imaging, and vector tomographic reconstruction algorithm for wind velocity field imaging. An acoustic tomography system is developed to validate the proposed methods in lab-scale applications. Due to the implemental limitation, simulation study is conducted to investigate the large-scale wind velocity field reconstruction. To accomplish these targets, the following research objectives were established:

- To develop a lab-scale acoustic tomography system with a transducer array which are capable of providing multiple ray paths for TOF measurements, configurable transmitter excitation, and received data acquisition, denoising and storage.

- To improve the accuracy of the TOF estimation against noise and interference to ensure that the relative root mean square error (rRMSE) of the TOF estimation is no more than 0.4% (in order to meet the requirement that tomographic reconstruction error is no more than 5%)

- To improve the performance of scalar tomographic reconstruction algorithms for effective reconstruction of two specific temperature field: one with a dynamic characteristic where the frame rate of the conventional system is not sufficient; and another with a large gradient where the commonly used straight ray model and linear reconstruction algorithm cannot be used.

- To investigate the vector tomographic reconstruction algorithm for effective reconstruction of the large-scale 2D horizontal wind velocity field.

1.3 Main contributions

The main contributions of this PhD study are summarised as follows:

- The data acquisition system for acoustic tomography. The key features of the presented system include: (1) a transducer array, which consists of 16 acoustic transmitters and 16 acoustic receivers around the

sensing area, to provide 192 TOFs for each frame's reconstruction; (2) a switching circuit for the semi-parallel data acquisition scheme; (3) the National instruments data acquisition card (NI DAQ) for excitation signal generation and received waveform measurement; and (4) a central control software for system configuration, received waveform monitoring and data storage.

- An improved TOF estimation method based on the AIC detection. Two improvements are studied in comparison with the conventional weighted AIC TOF estimation methods to reduce crosstalk interference and sound reflections: (1) an adaptive window is applied for accurate AIC TOF estimation; and (2) a phase correction method is developed to further improve the temporal resolution and noise robustness of the TOF estimation.

- A novel online time-resolved reconstruction method using fewer TOFs per frame. Firstly, by exploiting the redundancy of information in the temporal domain, a temporal regularisation is designed based on an adaptive auto aggressive (AR) model to reduce the required amount of TOF data per frame. A sliding overlapping window is applied to further improve the reconstruction accuracy. Secondly, a non-iteration scheme is used for the time-resolved reconstruction. Instead of conducting an iterative calculation upon each data set until convergence, the recursive reconstruction process performs a sliding iteration over each data segment. For the reconstruction of each frame, the online computation is non-iterative.

- A nonlinear reconstruction method is used to visualise a temperature field with a large temperature gradient. Instead of using the straight ray model and linear reconstruction algorithm, the bent ray model and the nonlinear reconstruction algorithms are applied. This allows the sound propagation ray paths and temperature distribution to be reconstructed iteratively from the TOFs. During the nonlinear reconstruction process,

the ray tracing process is greatly accelerated using fast marching method (FMM). Compared to the conventional shooting method ray tracing, which can only provide the ray path between one transmitter and one receiver, the FMM can calculate all the ray paths from one transmitter to all the receivers at the same time.

- A set of orthogonal acoustic waveforms based on the filtered and modulated Kasami sequence and the divergence-free regularised vector tomographic reconstruction method. The orthogonal excitation waveforms are used for the fully parallel data collection scheme to accelerate TOF measurements for large scale acoustic tomography. The divergence-free regularised vector tomographic reconstruction method is studied to overcome the invisible field effect of vector tomography problem. The 2D horizontal wind velocity field can be reconstructed with good accuracy using TOF measurements only.

1.4 Overview of the Thesis

The thesis is composed of 7 chapters and the remaining parts are structured as follows. Following the introductory part in this chapter, Chapter 2 reviews the foundations of acoustic tomography, the existing acoustic tomography systems for atmospheric imaging, the state-of-the-art acoustic tomography reconstruction algorithms, and the emerging applications of acoustic tomography where the TOF estimation method and image reconstruction methods can also be used.

In the first part of Chapter 3, the details of the lab-scale acoustic tomography system are presented. This includes the design and implementation of the transducer array, switching circuit, excitation and data collection, and the central control software. The second part of the chapter illustrates the phase corrected AIC TOF estimation method in terms of adaptive window selection, weighted AIC TOF estimation, phase correction, and ray length calibration. The performance of the data acquisition system and TOF estimation method is evaluated in the experiments.

Chapter 4 proposes a novel online time-resolved reconstruction algorithm for acoustic tomography. Details about the reconstruction algorithm are presented including: (1) a temporal regularisation based on an adaptive AR model to reduce the required amount of TOF data per frame; (2) a sliding overlapping window is applied to further improve the reconstruction accuracy; and (3) a recursive calculation scheme for non-iterative online reconstruction. The performance of the proposed online time-resolved reconstruction method is evaluated in the simulations and experiments.

Chapter 5 presents a nonlinear acoustic tomographic reconstruction algorithm using a bent ray model, when the temperature field has a large gradient and the refraction effect cannot be ignored. The reconstruction algorithm has following steps: (1) using the nonlinear conjugate gradient descent method to solve the nonlinear inverse problem; (2) fast acoustic ray tracing given the sound speed distribution using FMM; and (3) a line search for optimal step size. The performance of the proposed nonlinear acoustic tomographic reconstruction method is evaluated in the simulations.

Chapter 6 consists of two parts. The first part discusses the parallel TOF measurements using the cross-correlation TOF estimation and the design of the acoustic excitation signal based on the filtered and modulated Kasami sequence. The second part studies a vector tomographic reconstruction algorithm. The construction of the inverse problem applies the divergence-free regularisation and the vector Laplacian regularisation. The inverse problem is solved with the alternating direction method of multipliers (ADMM). The performance of the proposed reconstruction method is evaluated in the simulations.

Chapter 7 summarises the scientific contributions of the thesis and discusses the potential work in the future with an emphasis on further development on the basis of the developed acoustic tomography system and tomographic reconstruction algorithms.

Chapter 2 Review of acoustic tomography

2.1 Introduction

This thesis focus on the development of the TOF estimation and image reconstruction methods of acoustic tomography. The specific application area is the atmospheric imaging of temperature and wind velocity fields. Following the introduction, a detailed illustration is first given about the foundations of acoustic tomography, including the basics of acoustic wave propagation and the corresponding acoustic tomography forward problem. On that basis, a brief description about the acoustic tomography system will be presented and the state-of-the-art acoustic tomography systems for atmospheric imaging will be discussed. Furthermore, recent advances in acoustic tomography image reconstruction algorithms are briefly summarised. Finally, a brief review on other acoustic tomography applications will be given, where our TOF estimation and image reconstruction methods can also be used.

2.2 Foundations of acoustic tomography

Acoustic tomography can deliver accurate quantitative reconstruction of the covered temperature and wind velocity distributions with low equipment cost. With a small number of acoustic sensors placed around the sensing area, the TOF measurements can be obtained. Subsequently, the temperature image can be derived from the TOF measurements, since the group velocity of the sound in the sensing area is correlated with the temperature and wind velocity of the imaged medium. The TOF τ_Γ of ray path Γ is given by:

$$\tau_\Gamma = \int_\Gamma \frac{dl}{u} \tag{2.1}$$

where $\boldsymbol{u}$ denotes the group velocity of sound wave, and $\boldsymbol{l}$ represents the unit vector of the sound ray path, which is given by $\boldsymbol{l} = \boldsymbol{u}/u$.

The group velocity of sound in air is primarily affected by the Laplace sound speed (the speed of sound in ideal gas) c_L and the wind velocity $\boldsymbol{v}$ along the ray path.

$$\boldsymbol{u} = c_L \boldsymbol{n} + \boldsymbol{v} \tag{2.2}$$

where $\boldsymbol{n}$ denotes the unit vector normal to the wave front. A brief illustration of sound wave propagation in a moving inhomogeneous medium is given in Figure 2-1, where ***U*** represents the phase velocity (the velocity of the wave front) and *Φ* is the wave front.

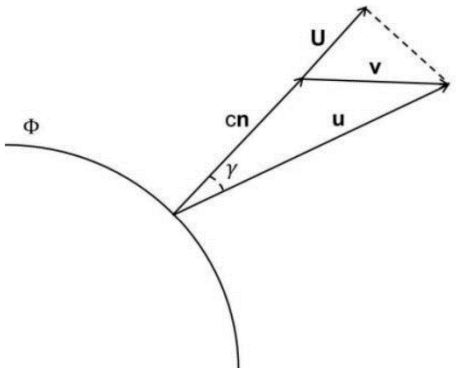

Figure 2-1: The sound wave propagation in inhomogeneous medium

According to [27], c_L in the atmosphere is given by

$$c_L = \sqrt{\gamma R T} \tag{2.3}$$

where γ=1.4 is the ratio of specific heats for dry air, $\mathrm{R} = 287.085\ \mathrm{m}^2/(\mathrm{s}^2\mathrm{K})$ is the gas constant for dry air, and *T* denotes the temperature distribution.

For equation (2.3), the effect of humidity on sound speed is ignored. The reason is twofold: (1) the effect of humidity on the Laplace sound speed is

relatively smaller than that of the temperature; and (2) this thesis mainly focuses on the applications of atmosphere imaging in dry air environment, for instance, the combustion chamber, the furnace and the near surface atmosphere.

Substituting equation (2.2) into equation (2.1), a nonlinear deterministic observation model can be used.

$$\tau_\Gamma = \int_\Gamma \frac{dl}{\left(c_L \boldsymbol{n} + \boldsymbol{v}\right)\boldsymbol{l}} \tag{2.4}$$

The sound propagation ray path depends on the unknown distribution of the Laplace sound speed and the wind velocity. As a result, the line integral in equation (2.4) becomes nonlinear. This creates a lot of difficulty for the reconstruction. Throughout the literature, the straight ray model has been widely used to approximate the true propagation ray path with a straight line connecting the transmitter and receiver.

The modelling error for using the straight ray model was quantitatively investigated in 2001 [28]. This research shows that the straight ray model can be applied for small-scale measurement setups (where the maximum ray length is less than a few hundreds of metres). As concluded, the straight ray model may lead to large modelling error due to the refraction effect, the presence of a large horizontal and vertical gradient in the temperature distribution, or the presence of a relatively large wind velocity field compared to Laplace sound speed c_L. Specifically, for ocean tomography, which uses the acoustic tomography principle to study the ocean current temperature, refraction due to the vertical gradient of c_L cannot be ignored. Example are listed below.

- For ultrasonic tomography designed for breast cancer detection, the large gradient of sound speed in the fat layer in the breast will causes a refraction effect to bend the ray path [7, 29]. The same issue happens

in the furnace environment and the combustion chamber, where the temperature field may have a relatively large gradient and the refraction effect cannot be ignored.

- For ocean tomography designed to monitor the ocean temperature and current, the vertical gradient of the sound speed will also result in multiple curved ray paths between transmitters and receivers [3]. Under these circumstances, the bent ray model should be used. This may require *priori* knowledge for the sound speed map, i.e. the sound speed profile for depth in ocean tomography. Alternately it would require a nonlinear reconstruction method which can reconstruct not only the distribution from the TOF measurements, but also the corresponding ray paths.

Given the sound propagation ray path, the relationship between the TOF measurements and the unknown temperature and wind velocity distribution can be determined.

For the application of temperature reconstruction where the wind velocity $\boldsymbol{v}$ can be ignored, the vectors $\boldsymbol{n}$ and $\boldsymbol{l}$ coincide since $\boldsymbol{l} = \dfrac{\boldsymbol{n} + \boldsymbol{v}/c}{\left|\boldsymbol{n} + \boldsymbol{v}/c\right|} = \boldsymbol{n}$. Therefore, equation (2.4) can be linearised as

$$\tau_\Gamma = \int_\Gamma \frac{dl}{c_L} = \int_\Gamma s_L \, dl \tag{2.5}$$

where $s_L = 1/c_L$ denote the sound speed slowness distribution.

Due to the limitation of a finite number of TOF measurements, the reconstruction process of acoustic tomography is only able to recover a finite number of unknowns. In this thesis, the square mesh is used to divide the sensing area into *N* pixels. Therefore, for both of the linearised line integrals given in equation (2.5), the forward problem should be written in discrete form as

$$\boldsymbol{\tau} = \boldsymbol{A}\boldsymbol{s} \tag{2.6}$$

where $\boldsymbol{s} \in \mathbb{R}$ describes the slowness distribution. $\boldsymbol{A} \in \mathbb{R}$ is the ray length matrix and its element $a_{i,j}$ is the segment length for the i-th ray path across the j-th pixel. $\tau \in \mathbb{R}$ represents the TOF measurements. N is the number of pixels and M is the number of TOFs

For the application of simultaneously reconstructing the temperature and wind velocity distributions, the linearization is different. Given c_0 and Δc_L are the reference mean value and the perturbation of the c_L, respectively. Therefore equation (2.4) can be linearised as:

$$\begin{aligned}
\tau_\Gamma &= \int_\Gamma \frac{ds}{\left(\left(c_0 + \boldsymbol{\Delta} c_L\right)\boldsymbol{n} + \boldsymbol{v}\right)\boldsymbol{s}} \\
&= \int_\Gamma \frac{\left(c_0\boldsymbol{n} - \boldsymbol{\Delta} c_L\boldsymbol{n} - \boldsymbol{v}\right)d\boldsymbol{s}}{\left(\left(\left(c_0 + \boldsymbol{\Delta} c_L\right)\boldsymbol{n} + \boldsymbol{v}\right)\boldsymbol{s}\right)\left(\left(\left(c_0 - \boldsymbol{\Delta} c_L\right)\boldsymbol{n} - \boldsymbol{v}\right)\boldsymbol{s}\right)} \\
&= \int_\Gamma \frac{\left(c_0\boldsymbol{n} - \boldsymbol{\Delta} c_L\boldsymbol{n} - \boldsymbol{v}\right)d\boldsymbol{s}}{\left(c_0\boldsymbol{n}\boldsymbol{s}\right)^2 - \left(\boldsymbol{\Delta} c_L\boldsymbol{n}\boldsymbol{s} + \boldsymbol{v}\boldsymbol{s}\right)^2} \\
&\overset{(a)}{\approx} \int_\Gamma \frac{d\,s}{c_0\boldsymbol{n}\boldsymbol{s}} - \int_\Gamma \frac{\left(\boldsymbol{\Delta} c_L\boldsymbol{n} + \boldsymbol{v}\right)d\boldsymbol{s}}{\left(c_0\boldsymbol{n}\boldsymbol{s}\right)^2} \\
&\approx \tau_0 - \frac{1}{c_0^2}\int_\Gamma \left(\boldsymbol{\Delta} c_L\boldsymbol{n} + \boldsymbol{v}\right)d\,\boldsymbol{s}
\end{aligned} \tag{2.7}$$

where in (a) we assume that group velocity perturbations caused by temperature and wind velocity changes $\boldsymbol{\Delta} c_L\boldsymbol{n} + \boldsymbol{v}$ should be much smaller than c_0.

which can be simplified to

$$\left(\tau_0 - \tau\right)c_0^2 = \int_\Gamma \left(\Delta c_L\boldsymbol{n} + \boldsymbol{v}\right)d\boldsymbol{s} \tag{2.8}$$

Based on this straight line assumption, reciprocal tomography is employed in the acoustic tomography system and the influence brought by $\Delta c_L \boldsymbol{n}$ and $\boldsymbol{v}$ can be separated using the back and forth measurements τ_+ and τ_-.

$$\frac{(\tau_+ + \tau_-)c_0^2}{2} = \int_\Gamma \Delta c_L \, ds \tag{2.9}$$

$$\frac{(\tau_+ - \tau_-)c_0^2}{2} = \int_\Gamma \boldsymbol{v} \, d\boldsymbol{s} \tag{2.10}$$

The discretisation of equation (2.9) is similar to equation (2.6) and for equation (2.10), it can be discretised as

$$\boldsymbol{l} = \boldsymbol{S}\boldsymbol{V} \tag{2.11}$$

where $\boldsymbol{l} \in \mathbb{R}^N$, its elements are $l_i = \frac{(\tau_{i,+} - \tau_{i,-})c_0^2}{2}$ and N is the number of ray paths; $V = [\boldsymbol{V_x}; \boldsymbol{V_y}]$, $V \in \mathbb{R}^{2M}, \boldsymbol{V_x}, \boldsymbol{V_y} \in \mathbb{R}^M$, and M is the number of pixels; $\boldsymbol{S} = [\boldsymbol{Sx};\ \boldsymbol{Sy}]$, and $\boldsymbol{Sx}, \boldsymbol{Sy} \in \mathbb{R}^{N*M}$ are the directional ray length matrix whose elements are $s_{i,j}\cos(\theta)$ and $s_{i,j}\sin(\theta)$ respectively.

2.3 Acoustic tomography system

2.3.1 System architecture and function

An acoustic tomography system is generally composed of three sub-systems, i.e., an acoustic transducer array, the central control system, and the tomographic image reconstruction system. The acoustic transducer array consists of several transmitters and receivers placed at the boundary of the sensing area. They form multiple transducer pairs for the TOF measurements. The central control system consists of four modules, including the excitation signal generation module, the data acquisition module, the digital signal processing module and the TOF estimation module. The obtained TOF measurements will be sent to the tomographic visualization system for image

reconstruction, visualization and analysis. In this thesis, the development of a lab-scale acoustic tomography system will be demonstrated in chapter 3.

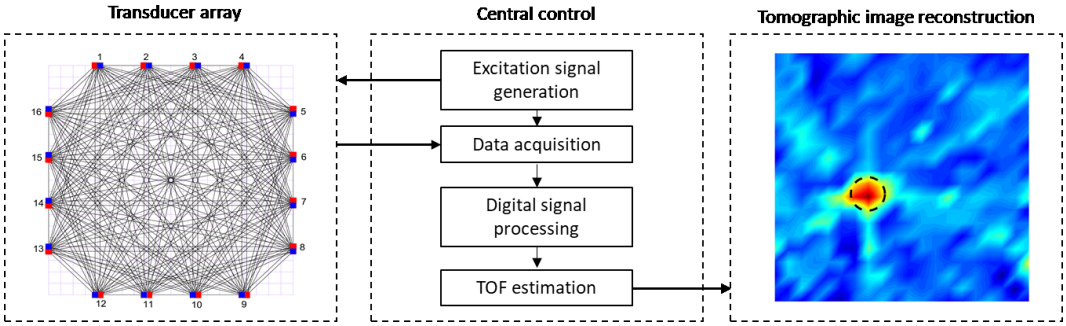

Figure 2-2: Functional system diagram

2.3.2 Existing acoustic tomography system

This review mainly focuses on the application of atmospheric imaging, which uses the acoustic tomography system to reconstruct the temperature and wind velocity fields. Several tomographic systems listed in Table 2-1 have been developed to perform imaging in this area, including the large-scale (from tens to several hundred metres) atmospheric imaging system, the small-scale (from several metres to tens metres) indoor climate and combustion chamber monitoring system, and lab-scale (within 1 metre) acoustic tomography system. For large scale system, the number of acoustic transducers is very limited (usually less than 10) due to high implemental cost of data acquisition system. The signal frequency is less than 2kHz for long sound propagation distance. On the contrary, increased number of transducers and high frequency of acoustic signals can be used in the small scale and lab scale system, which in return improve the tomographic reconstruction quality.

The first acoustic tomography system for large-scale atmospheric imaging was developed at Pennsylvania State University at the beginning of the 1990s[16]. Their transducer array consists of three speakers and five microphones placed a few metres above the ground. This transducer array covers a square sensing area with a side length of 200 m and provide 15 TOFs for reconstruction. The transmitted signals are frequency modulated waveforms with their frequencies swept from 100 to 1000 Hz over a duration of 0.1 seconds. In the mid-1990s,

a portable array for acoustic tomography of the atmosphere surface layer (ASL) was built at the Institute of Meteorology, University of Leipzig, Germany. In this array, 8-12 speakers and microphones were mounted on tripods 2 m above the ground. The size of the sensing area varied from tens to several hundreds of metres. The transmitted acoustic signals were two short bursts of 1 kHz sinusoid wave separated by 20 ms. In 2008, [30] at New Mexico State University, an acoustic tomography system with a three-layer transducer array was built, which consisted of three transmitter and five receiver towers covering a square sensing area with side length of 80 m. In each tower, transmitters or receivers were placed at three levels ranging from 3 to 9 m, which allowed the measurement of TOFs between transmitters and receivers at different levels. In total, this three-layer array can provide 56 TOF measurements for reconstruction.

The small-scale acoustic tomography system used for the gas boiler was first discussed in Green's work in 1986 [31]. Since then, numerous efforts have been made to improve the acoustic tomography system for the boiled furnace, the combustion chamber and many other applications. In 1996, the PYRA system was developed for temperature imaging inside power plant boiler [22]. This used 7 acoustic transceivers operating at 1800 Hz to cover a 5.929 by 5.313 m sensing area, and 13 TOF measurements were used for reconstruction. The North China Electric Power University developed an acoustic tomography system for the online monitoring of the coal-fired boiler [24] and Ash fouling [23]. Their transducer array consisted of 4 loudspeakers and 8 microphones whose frequency swept from 500 Hz to 8000 Hz over a duration of 0.1 seconds.

Table 2-1: Comparison of some recent acoustic tomography systems for atmospheric imaging.

Researchers	Date	Receiver	Transmitter	Frequency	Sensing area	Ray path	Spatial resolution
Wilson *et al.*	1994	5	3	100 to 1000 Hz	200×200 m^2	15	50 m
Bramanti *et al.*	1996	1	1	1800	5.929×5.313 m^2	13	0.5 m
Ziemann *et al.*	1997	4	6	1000 Hz	200×260 m^2	15	20 m
Ziemann *et al.*	2002	12	8	1000 Hz	300×440 m^2	79	75 m
Holstein *et al.*	2004	4	8	1000 Hz to 10 kHz	15×20 m^2	32	4 m
Jovanovi´c *et al.*	2008	12	12	40 kHz	1 m^2circular	72	0.15 m
Ostashev *et al.*	2008	15	9	Non mentioned	300×440 m^2	36	75 m
Yan *et al*	2012	16	16	500 to 2000 Hz	1.19×1.19 m^2	96	0.06 m
Zhang *et al*	2015	8	4	500 to 8000 Hz	18.89×17.85 m^2	12	1.2 m
Liu *et al*	2017	20	20	40 kHz	0.215×0.215 m^2 circular	100	0.07m

Later, various lab-scale acoustic tomography systems have been developed to measure room temperature distribution [18, 20, 32, 33] and the wind velocity of a wind tunnel [19, 34, 35]. Compared to the acoustic tomography system for large scale atmospheric and small-scale boiler monitoring, the lab-scale acoustic tomography system usually has a smaller sensing area (varying from 0.3 to 2 m) and consists of a large number of transducers (more than 16). The small sensing area results in a higher TOF estimation accuracy on the short ray path, therefore transducers with higher operating frequency (40 kHz) are used. Benefiting from the low implementation cost, the lab-scale system is able to use more acoustic transducers placed on the boundary. This can provide more ray paths for TOF measurements, and an improved reconstruction with higher image quality. However, previous lab-scale acoustic tomography system utilized a sequential data collection scheme, which increased the data collection time per frame and reduce the temporal resolution. Besides, the commonly used piezoelectric transducers has a relative small beam angle, which reduced the number of ray paths for the tomographic reconstruction.

2.4 TOF estimation

The major challenge in employing acoustic tomography for temperature field monitoring is to achieve high TOF measurement accuracy. An accurate TOF estimation is also essential in other applications, for example, ultrasonic ranging, positioning and synchronisation systems [36, 37], ocean tomography [3], ultrasonic breast cancer detection [7], and seismic wave arrival time estimation. To date, a number of TOF estimation methods have been developed in other disciplines.

Methods based on cross-correlation are usually used for TOF estimation. Such methods assume that the received signal is the time-shifted replica of the reference signal. The TOF is considered as the time delay [38, 39]. However, measurement accuracy is limited because 1) the received signal is corrupted by White Gaussian Noise (WGN) and interference due to channel crosstalk and sound reflections; and (2) the received signal waveform is not a time-

shifted replica of the reference signal due to waveform distortion under a complex internal structure of the medium.

Estimating the TOF through parametric approximation through envelope extraction [38, 40, 41] has been widely used in ultrasound ranging and non-destructive testing. The received signal is usually modelled as a delayed Gaussian echo signal, and the TOF can be estimated after its envelope is extracted [42]. However, this Gaussian echo model is based on the assumption that the received signal is a backscattered echo from a flat surface reflector.

Numerous automatic arrival time estimation methods have been developed for seismic wave data analysis in geophysical applications. Short and long time-averaged ratio (STA/LTA) [43], phase arrival identification- kurtosis (PAI-K) [44] and other window-based methods calculate the characteristic function (waveform energy, absolute amplitude, kurtosis values, and many other characteristic functions) within a predetermined window. The arrival times are estimated based on the maximum value of the derivative. Variations of the aforementioned methods are the modified energy ratio (MER) [45], the modified Coppens' method (MCM) [46], and the short-term or long-term kurtosis ratio (S/L-Kurt) [47]. These methods calculate the characteristic function from post- and pre-sample windows. The temporal index associated with the maximum ratio represents the arrival time. There are also numerous hybrid approaches based on these algorithms that attempt to more accurately estimate the TOF and these include the wavelet transform approaches [48] and the joint energy ratio (JER) [49].

The Akaike Information Criterion (AIC) and autoregressive (AR) techniques were first applied to TOF estimation of seismic wave data [50]. The arrival time is considered as a transition point that separates the signal into two different stationary processes. Therefore, the AIC function can be used to determine the transition point while the minimum AIC value indicates the optimum TOF estimate. However, the AR model's order should be determined heuristically and considering the noise level. To overcome this problem, Zhang [48]

proposed a wavelet–AIC picker in which the AIC values are calculated directly from the seismogram using Maeda's formula [51], the latter of which computes the AIC directly from the waveforms without using the AR model coefficients. With some modification, the algorithms used in seismology can be applied to ultrasound signals [8].

Two issues remain before the AIC TOF estimation method is applied to our acoustic TOF tomography data. Firstly, the accuracy of the AIC TOF estimation method is affected by crosstalk interference and reflection echoes, both of which manifest in the received ultrasound signal. Secondly, the method is not robust against random noise, especially for the noise in close temporal proximity to the arrival time.

To solve these two problems, a modified phase corrected AIC TOF estimation method (PCAIC) is proposed for the acoustic tomography system. Two improvements are developed compared to the conventional weighted AIC TOF estimation methods; the first improvement is an adaptive window applied to the received ultrasonic signal to reduce the effect of crosstalk interference and reflection echoes. The second one is phase correction to improve the temporal resolution and accuracy of the TOF measurements.

2.5 The state-of-art image reconstruction algorithm

The acoustic tomography reconstruction is a process to calculate an unknown distribution from a limited number of TOF measurements. In this section, a review of the fundamentals of acoustic tomography reconstruction will be given. Reconstruction methods are based on the forward problem defined in equations (2.6) and (2.11), which use a straight ray model to approximate the true ray path. The nonlinear reconstruction for a bent ray model will be discussed later in Chapter 5.

Although the forward problem of the acoustic tomography can be considered as the Radon transform if the straight ray model is used, the transform-based reconstruction method, including the inverse Radon transform, the Fourier

slice theorem, and the filtered back projection, are not discussed in this section. This is because the transform-based method requires full knowledge of the line integral measurements (TOF) from all lines and direction. In fact, for a typical acoustic tomography system set up, the number of TOFs is very limited and the transform-based reconstruction may suffer from the lack of quantitative accuracy[52].

2.5.1 Algebraic-based algorithms

The algebraic-based algorithms are the most widely used approach throughout the literatures [13, 17, 18, 20, 21, 28, 32, 33, 53-56]. Generally, this approach minimises a cost function to evaluate the mismatch between the unknown distribution (c_L , v) and the TOF measurements. For the algebraic-based method, the measurement noise is usually modelled as the additive white Gaussian. If accurate knowledge about the noise distribution is available, for instance, the Poisson noise model, the statistical-based algorithm should be used to formulate the inverse problem. Therefore, the inverse problem of the acoustic tomography can be formulated as a simple least square problem as follows:

$$\min_{x} \left\| \boldsymbol{y} - \boldsymbol{A}\boldsymbol{x} \right\|_2^2 \tag{2.12}$$

where $\boldsymbol{y} \in \mathbb{R}$ denotes the TOF measurement, $\boldsymbol{x} \in \mathbb{R}$ represents the unknown distribution (c_L or $\boldsymbol{v}$ for specific application) and $\boldsymbol{A} \in \mathbb{R}$ is the corresponding ray length matrix as is defined in equation (2.6). The least square equation (2.12) has the explicit solution $\boldsymbol{x}_{ls}$.

$$\boldsymbol{x}_{ls} = \left(\boldsymbol{A}^T \boldsymbol{A} \right)^{-1} \boldsymbol{A}^T \boldsymbol{y} \tag{2.13}$$

However, there are two difficulties before this least square solution is applied. Recall the forward problem of acoustic tomography, the TOF measurements take the form of Fredholm integral equations of the first kind. Therefore the corresponding inverse problem defined in equation (2.12) is ill-posed, and the

solution in equation (2.13) is very sensitive to measurement noise. Small perturbations in the TOF measurement will incur large artefacts in the reconstructed image.

Besides, the inverse problem is usually under-determined, which means the number of TOF measurements *M* is much smaller than the number of unknowns *N*. It is difficult to recover the desired distribution with good spatial resolution from the limited number of TOFs.

Numerous algebraic-based reconstruction methods are developed to solve this under-determined and ill-posed inverse problem, which can be divided into two categories, the subspace projection method [13, 34, 57-59], and the regularisation method [1, 17-19, 28, 29, 32, 53, 60-62]. Both of these approaches are able to: (1) improve the ill-posedness of the inverse problem and provide tomographic images which are less sensitive to noise; and (2) improve the image quality in terms of spatial resolution, temporal resolution and quantitative accuracy by incorporating *priori* knowledge of the target image.

Subspace-projection

The general idea of the subspace projection method is to consider a suitable basis of function to approximate the target distribution with fewer parameters. The reconstruction accuracy relies on the assumption that there exists a potentially low-dimensional basis set to capture the key feature the dominant features of the desirable image. The optimal basis function can be obtained from *priori* knowledge [20] or learned from the available data set [10]. But in most cases, the radial basis function (RBF) can be used for simplicity [13, 34, 54, 57, 58].

For the RBF representation, it takes the form as

$$x(\boldsymbol{r}) = \sum_{k=1}^{K} b_k e^{-\omega \|\boldsymbol{r}-\boldsymbol{r}_c\|^2} \tag{2.14}$$

Equation (2.14) in matrix form:

$$\boldsymbol{x} = \boldsymbol{\Phi b} \tag{2.15}$$

where $\boldsymbol{b} \in \mathbb{R}$ is the RBF weights and $\boldsymbol{\Phi} \in \mathbb{R}$ is the matrix form of the RBF representation operator. *K* is the number of RBF functions used for representation, usually in most applications *K* is much smaller than the number of pixels *N*. b_k is the unknown RBF weights, $\boldsymbol{r}_c$ represents the centres position of RBF, and in this thesis the RBF centres are uniformly distributed inside the sensing area. ω is the shape parameter of the RBF function.

Combining equations (2.12) and (2.14), equation (2.12) becomes a low dimensional inverse problem

$$\min_{\boldsymbol{b}} \left\| \boldsymbol{y} - \boldsymbol{A\Phi b} \right\|_2^2 \tag{2.16}$$

With the use of RBF basis functions, the number of unknowns has been reduced to K, which is usually much less than the number of measurements. The inverse problem defined in equation (2.16) has become an over-determined problem. However, the use subspace projection, i.e. RBF, may lead to a rank deficient inverse problem [52]. The new system matrix $\boldsymbol{A\Phi}$ has a dispersed singular value and results in a larger condition number compared to $\boldsymbol{A}$. The solution to equation (2.16) is very sensitive to noise.

Then the modified inverse problem with fewer unknowns can be solved with the truncated singular value decomposition (TSVD) method, which supresses the noise effect by discarding the image component corresponding to the smaller singular value. Besides, a regularisation method can be used to solve the ill-posed inverse problem, and a discussion will be given in next subsection.

And the solution using RBF subspace projection and TSVD reconstruction is[63]:

$$\boldsymbol{x}_{rbf} = \boldsymbol{\Phi V \Sigma}_p^{-1} \boldsymbol{U}^T \boldsymbol{y} \tag{2.17}$$

where $\boldsymbol{A\Phi = U\Sigma V^T}$ and $\boldsymbol{U} \in \mathbb{R}$, $\boldsymbol{\Sigma} = [diag(\sigma_1, \sigma_2, ..., \sigma_M), \boldsymbol{0}^{M\times(K-M)}]$ and $\boldsymbol{V} \in \mathbb{R}$. p is the number of largest singular values kept for reconstruction. The inverse matrix of singular value is given by:

$$\Sigma_p^{-1} = [diag(\frac{1}{\sigma_1}, \frac{1}{\sigma_2}, ..., \frac{1}{\sigma_p}), \boldsymbol{0}^{M\times(K-P)}] \tag{2.18}$$

In summary, the subspace projection method utilises the *priori* knowledge to solve ill-posed inverse problem. From equation (2.18) it can be seen that the small singular values, which has $\sigma_i < \sigma_p$, are discarded in the reconstruction. Consequently, the reconstruction will be less sensitive to noise.

Regularisation method

Another approach to solve the ill-posed and underdetermined inverse problem is to add a regularisation in the cost function. A general form of the cost function consists of two functions, the data fidelity term that measure the distance between the measurements $\boldsymbol{y}$ and the back-projected image $\boldsymbol{Ax}$; and a regularisation term which penalises the potential solution with an undesired property. The solution to the inverse problem can be obtained by solving the convex minimisation problem as shown in equation (2.19).

$$\min_{\boldsymbol{x}} \|\boldsymbol{y} - \boldsymbol{Ax}\|_2^2 + \lambda R(\boldsymbol{x}) \tag{2.19}$$

where $R(\boldsymbol{x})$ is the regularisation term built based on the *priori* knowledge for the unknown distribution $\boldsymbol{x}$. λ is the regularisation weight. Regularisation is used for two reasons:

- The regularisation term enforce regularity to suppress the unwanted noise component and make the reconstruction less sensitive to noise.
- The regularisation term interprets the *priori* knowledge of the distribution, which may help to improve the spatial resolution and reduce the reconstruction error of the reconstruction result.

Typical selections of the regularisation term are the l_2 regularisation for smoothness constraints, the l_1 regularisation for sparsity constraints, and the nuclear norm regularisation for low-rank structure constraints.

For the l_2 regularisation, which is used as a smoothness constraint, the general form is defined below:

$$\boldsymbol{R}(\boldsymbol{x}) = \|\boldsymbol{F}\boldsymbol{x}\|_2^2 \tag{2.20}$$

where $\boldsymbol{F}$ is the regularisation matrix. The matrix $\boldsymbol{F}$ can be the identity matrix ($\boldsymbol{F} = \boldsymbol{I}$) as the Tikhonov regularisation [63]. Besides, the regularisation matrix can be built based on other differential operators to enforce smoothness of the reconstructed image. An example is the four-connected region second-order Laplacian operator matrix ($\boldsymbol{F} = \boldsymbol{L}$) for the Laplacian regularisation [64].

The solution to the l_2 regularised inverse problem is

$$\boldsymbol{x}_{l2} = \left(\boldsymbol{A}^T\boldsymbol{A} + \lambda\boldsymbol{F}^T\boldsymbol{F}\right)^{-1}\boldsymbol{A}^T\boldsymbol{y} \tag{2.21}$$

The regularisation parameter λ is usually chosen empirically, which is to ensure (1) the matrix $\boldsymbol{A}^T\boldsymbol{A} + \lambda\boldsymbol{F}^T\boldsymbol{F}$ is full-ranked with an smaller condition number, and (2) the reconstruction can provide desired results . The solution $\boldsymbol{x}_{l2}$ is therefore more robust against random noise.

For better image quality, the l_2 regularised inverse problem can also be solved iteratively through many well-established optimization algorithms such as gradient descent, conjugate gradient descent, and quasi-newton methods. The gradient descent optimization, which in the acoustic tomography field is commonly known as the simultaneous iterative reconstruction technique (SIRT) [19, 62], can be expressed below

$$\begin{aligned} \boldsymbol{x}_i &= \boldsymbol{x}_{i-1} - \mu \boldsymbol{P}\boldsymbol{A}^T\boldsymbol{W}(\boldsymbol{A}\boldsymbol{x}_{i-1} - \boldsymbol{y}) - \mu\lambda \boldsymbol{P}\boldsymbol{F}^T\boldsymbol{F}\boldsymbol{x} \\ \boldsymbol{P} &= diag(1/LP_1, 1/LP_2, ..., 1/LP_N) \\ \boldsymbol{W} &= diag(1/LR_1, 1/LR_2, ..., 1/LR_M) \end{aligned} \tag{2.22}$$

where i denotes the iteration index and μ represents the step size, in our case it can be set as 1. Generally, a step size of $\mu < 2/\sigma_{\max}(\boldsymbol{A})$, where $\sigma_{\max}(\bullet$ denotes the maximum singular value of matrix. $LP_i = \sum_{i=1}^{N} a_{i,j}$ which denotes the total length of all the ray paths cross the i-th pixel. $LR_j = \sum_{j=1}^{M} a_{i,j}$ which represent the length of j-th ray path. The diagonal preconditioner $\boldsymbol{P}$ is used to improve the reconstruction convergence performance and the geometrical weight operator $\boldsymbol{W}$ is used so that the TOFs for the rays that traverse longer paths can tolerate larger errors.

For the l_1 regularisation, the general form is defined as:

$$\boldsymbol{R}(\boldsymbol{x}) = \|\boldsymbol{F}\boldsymbol{x}\|_1 \tag{2.23}$$

where the regularisation matrix $\boldsymbol{F}$ can be the identity matrix($\boldsymbol{F} = \Psi$) as the sparsity regularisation, with *priori* knowledge that the target distribution of temperature and wind velocity has sparse representation using a specific model [4, 60]. The commonly used are the sparsity regularisation ($\boldsymbol{F} = \boldsymbol{I}$) and TV regularisation ($\boldsymbol{F} = \mathrm{TV}(\bullet$, $TV(\bullet$ is the 2D total variation norm operator) for ultrasound tomography for medical imaging [10, 65] for edge preserving property.

The l_1 regularised inverse problems are usually solved iteratively, based on a number of well investigated methods, such as the Gradient Projection [66, 67], the iterative shrinkage-thresholding algorithms (ISTA) [68, 69], the Proximal Gradient [70, 71], and Augmented Lagrange Multiplier [72]. For the widely

used iterative shrinkage-thresholding algorithm (ISTA), the iteration process for sparse regularised inverse problems ($\boldsymbol{F} = \boldsymbol{I}$) is expressed as:

$$\mathbf{x}_i = \mathbf{P}_{\lambda t}\left(\mathbf{x}_{i-1} - 2\mu\mathbf{A}^T(\mathbf{A}^T\mathbf{x}_{i-1} - \mathbf{y})\right) \tag{2.24}$$

where the thresholding operator is defined as

$$\mathbf{P}_{\alpha}(\mathbf{x}) = \left(|\mathbf{x}| - \alpha\right)_+ \operatorname{sgn}(\mathbf{x}) \tag{2.25}$$

The nuclear norm regularisation is mainly used for the dynamic imaging of the temperature and wind velocity fields, based on the low rank structure of several successive scans. The low rank structure can be expected if successive tomographic images are stacked as the columns of a temporal-spatial image matrix. The similarities between the successive tomographic images ensure that the corresponding temporal-spatial image matrix is a rank deficient matrix. This low rank property can be used as the *priori* knowledge to reduce the number of measurements required per frame or to enhance the quality of the follow up images. Since the rank penalty is nonconvex, it is often replaced with the nuclear norm, which is the closest convex relaxation [73]. Generally, the inverse problem can be defined as:

$$\boldsymbol{X} = \arg\min_{X} \|\boldsymbol{Y} - \boldsymbol{AX}\|_F + \lambda\|\boldsymbol{X}\|_* \tag{2.26}$$

where the TOFs and images for all the frames of the tomographic images are stacked as columns and denoted as $\boldsymbol{X} = [\boldsymbol{x_1}, \boldsymbol{x_2}, ..., \boldsymbol{x_T}]$ and $\boldsymbol{Y} = [\boldsymbol{y_1}, \boldsymbol{y_2}, ...\boldsymbol{y_T}]$, $\|\bullet\|_F$ is the Frobenius norm, $\|\bullet\|_*$ represents the nuclear norm and T is the number of frames. Then, the forward problem can be written as $\boldsymbol{Y} = \boldsymbol{AX}$, where the block diagonal matrix $\boldsymbol{A}$ is given as $\boldsymbol{A} = diag\{\boldsymbol{A_1}, \boldsymbol{A_2}, ..., \boldsymbol{A_T}\}$.

The solution of the nuclear norm regularised inverse problem is computed iteratively based on the iteratively hard thresholding method (IHT) [74].

$$\begin{aligned} \boldsymbol{X}_{i+1/2} &= \boldsymbol{X}_i - \mu_i \boldsymbol{A}^T (\boldsymbol{AX} - \boldsymbol{Y}) \\ \boldsymbol{X}_{i+1} &= \boldsymbol{P}_r(\boldsymbol{X}_{i+1/2}) \end{aligned} \tag{2.27}$$

$\boldsymbol{P}_r(\boldsymbol{X})$ computes a rank-r approximation as

$$\boldsymbol{P}_r(\boldsymbol{X}) = \boldsymbol{U}\boldsymbol{\Sigma}_r\boldsymbol{V}^T \tag{2.28}$$

where $\boldsymbol{X} = \boldsymbol{U}\boldsymbol{\Sigma}\boldsymbol{V}^T$ and $\boldsymbol{U} \in \mathbb{R}$, $\boldsymbol{\Sigma} = [diag(\sigma_1, \sigma_2, ..., \sigma_T); \boldsymbol{0}^{(N-T)\times T}]$ and $\boldsymbol{V} \in \mathbb{R}$. r is the number of largest singular values kept for reconstruction. The shrinkage matrix of singular value is given by:

$$\boldsymbol{\Sigma}_r = [diag(\sigma_1, \sigma_2, ..., \sigma_r); \boldsymbol{0}^{(N-r)\times r}] \tag{2.29}$$

Table 2-2: Iterative hard thresholding algorithm for low rank reconstruction

Input: $\boldsymbol{Y}$ $\boldsymbol{A}$ IterNo, r, ε

Ourput: $\boldsymbol{X}$

Initialise: $\boldsymbol{X}_o = \boldsymbol{0}$

For i=1 : IterNo

$$\boldsymbol{X}_{i+1/2} = \boldsymbol{X}_i - \mu_i \boldsymbol{A}^T (\boldsymbol{AX} - \boldsymbol{Y})$$

$$\boldsymbol{X}_{i+1} = \boldsymbol{P}_r(\boldsymbol{X}_{i+1/2})$$

If $\left\|\boldsymbol{X}_{i+1} - \boldsymbol{X}_i\right\|_F \le \varepsilon$ break

End

2.5.2 Statistical-based algorithms

The statistical-based reconstruction methods have been developed to solve the acoustic tomography inverse problem since decades ago [35, 55, 75-77]. Generally, this approach considers the tomographic inverse problem in the

framework of Bayesian statistics, that all the variables in the model are random variables and the solution is calculated based on the Maximum a posteriori (MAP) estimator[78]. Compared to the algebraic-based method, especially the regularisation method, this allows for better modelling of the *priori* knowledge for both the measurement noise distribution and the unknown distribution. This review mainly focuses on the additive noise model, which is preferred throughout literatures.

$$\boldsymbol{y} = \boldsymbol{A}\boldsymbol{x} + \boldsymbol{n} \tag{2.30}$$

where the measurement contaminant with zero mean Gaussian additive noise $\boldsymbol{n} \sim \quad \boldsymbol{0} \quad \boldsymbol{I})$.

Then the MAP inversion is defined as:

$$\boldsymbol{x}_{MAP} = \arg\min_{\boldsymbol{x}} \{-\log(P(\boldsymbol{x} \mid \boldsymbol{y}))\} \tag{2.31}$$

According to the Bayesian theory, $P(\boldsymbol{x} \mid \boldsymbol{y}) = \frac{P(\boldsymbol{y} \mid \boldsymbol{x}) p(\boldsymbol{x})}{P(\boldsymbol{y})}$. Since the measurement data $\boldsymbol{y}$ is given, $P(\boldsymbol{y}) = 1$, then equation 错误!未找到引用源。 become

$$\boldsymbol{x}_{MAP} = \arg\min_{\boldsymbol{x}} \{-\log(P(\boldsymbol{y} \mid \boldsymbol{x}))\} - \log(P(\boldsymbol{x})) \tag{2.32}$$

where $P(\boldsymbol{y} \mid \boldsymbol{x})$ is the conditional probability of $\boldsymbol{y}$ given $\boldsymbol{x}$, which is the likelihood function. $P(\boldsymbol{x})$ is the *priori* probability of the $\boldsymbol{x}$.

The construction of the likelihood function is the key of statistical inversion. The likelihood function comprises the forward model of the measurement process as well as the information about the measurement noise. For the most frequent case, the additive noise, a brief illustration is given below.

Assume the noise probability distribution $P_{noise}(\boldsymbol{n})$ is known, and the noise $\boldsymbol{n}$ is independent with the target distribution $\boldsymbol{x}$, then the conditional probability of $\boldsymbol{y}$ given $\boldsymbol{x}$ is distributed like $\boldsymbol{n}$.

$$P(\boldsymbol{y} \mid \boldsymbol{x}) = P_{noise}(\boldsymbol{y} - \boldsymbol{A}\boldsymbol{x}) \tag{2.33}$$

For the commonly used zero mean Gaussian noise model,

$$P_{noise}(\boldsymbol{n}) \propto \exp\left(-\frac{1}{2\sigma_n^2}\|\boldsymbol{n}\|_2^2\right) \tag{2.34}$$

Therefore, the corresponding likelihood function becomes

$$P(\boldsymbol{y} \mid \boldsymbol{x}) \propto \exp\left(-\frac{1}{2\sigma_n^2}\|\boldsymbol{y} - \boldsymbol{A}\boldsymbol{x}\|_2^2\right) \tag{2.35}$$

Considering the special case that the *priori* model is ignored and $\boldsymbol{x}$ follow a uniform distribution, then the MAP inversion defined in equation 错误!未找到引用源。 becomes the standard least square problem defined in equation (2.12), which is underdetermined and ill-posed.

The construction of the *priori* probability $P(\boldsymbol{x})$ will help to improve the reconstruction accuracy and image quality. Different construction methods have been developed and used successfully in tomographic inverse problems. Their *priori* probability models are listed in Table 2-3. This section focuses on the Gaussian *priori* model, since it is undoubtedly the mostly used probability density for statistical inversion.

Let the target distribution $\boldsymbol{x}$ and measurement noise $\boldsymbol{n}$ be mutually independent Gaussian random variables

$$\begin{aligned} \boldsymbol{x} &\sim \quad\quad {}_{x}) \\ \boldsymbol{n} &\sim \quad\quad) \end{aligned} \tag{2.36}$$

where $\boldsymbol{\Gamma}_x \in \mathbb{R}$ and $\boldsymbol{\Gamma}_n \in \mathbb{R}$ are the covariance matrix of $\boldsymbol{x}$ and $\boldsymbol{n}$ respectively. $\boldsymbol{x}_0$ denotes the mean vector. According to [78] the posteriori probability become

$$P(\boldsymbol{x} \mid \boldsymbol{y}) \propto \exp\left(-\frac{1}{2} \left\| \boldsymbol{x} - \bar{\boldsymbol{x}} \right\|^2_{\Gamma^{-1}_{post}} \right) \tag{2.37}$$

Table 2-3: Priori probability models

Method	$P(\boldsymbol{x})$ **model**
Gaussian *priori*	$P(\boldsymbol{x}) = \left(\frac{1}{2\pi \lvert \boldsymbol{\Gamma} \rvert} \right)^{N/2} \exp\left(-\frac{1}{2} (\boldsymbol{x} - \boldsymbol{x}_0)^T \boldsymbol{\Gamma}^{-1} (\boldsymbol{x} - \boldsymbol{x}_0) \right)$
Impulse *priori*	$P(x) = \left(\frac{\alpha}{2} \right)^{\mathrm{N}} \exp\left(-\alpha \lVert \boldsymbol{x} \rVert_1 \right)$
Discontinuity	$P(\boldsymbol{x}) = \left(\frac{\alpha}{\pi} \right)^{N} \frac{1}{1 + \alpha^2 (x_j - x_{j-1})^2}$
Total variation	$P(\boldsymbol{x}) \propto \exp(-\alpha \boldsymbol{TV}(\boldsymbol{x}))$

Under this purely Gaussian assumption, the condition mean $\bar{\boldsymbol{x}}$ is simultaneously the MAP estimator

$$\boldsymbol{x}_{MAP} = \bar{\boldsymbol{x}} = (\boldsymbol{\Gamma}_x^{-1} + \boldsymbol{A}^T \boldsymbol{\Gamma}_n^{-1} \boldsymbol{A})^{-1} (\boldsymbol{A}^T \boldsymbol{\Gamma}_n^{-1} \boldsymbol{y} + \boldsymbol{\Gamma}_x^{-1} \boldsymbol{x}_0) \tag{2.38}$$

and

$$\boldsymbol{\Gamma}_{post} = (\boldsymbol{\Gamma}_x^{-1} + \boldsymbol{A}^T \boldsymbol{\Gamma}_n^{-1} \boldsymbol{A})^{-1} \tag{2.39}$$

The problem can be further simplified by setting $\boldsymbol{\Gamma}_x = \gamma^2 \boldsymbol{I}$ and $\boldsymbol{\Gamma}_n = \sigma^2 \boldsymbol{I}$, and both the target distribution $\boldsymbol{x}$ and $\boldsymbol{n}$ are zero mean Gaussian distribution. In this case,

$$\boldsymbol{x}_{MAP} = \gamma^2 \boldsymbol{A}^T \left(\gamma^2 \boldsymbol{A}\boldsymbol{A}^T + \sigma^2 \boldsymbol{I}\right)^{-1} \boldsymbol{y} = \boldsymbol{A}^T \left(\boldsymbol{A}\boldsymbol{A}^T + \lambda^2 \boldsymbol{I}\right)^{-1} \boldsymbol{y} \qquad (2.40)$$

where $\lambda = \frac{\sigma}{\gamma}$ is the ratio of the noise and *priori* variances. The solution defined in equation (2.40) is known as the Wiener Filter solution, which was first used in acoustic tomography reconstruction in 1994 by Wilson, known as stochastic inversion (SI) [16]. This method was extended to the time-dependent stochastic inversion (TDSI) in [75], which uses the spatial-temporal covariance to incorporate the data set at different times for dynamic reconstruction. The SI and TDSI methods assume that the target distribution, the temperature and wind velocity, are statistically homogeneous in space, which allows us to use the zero mean Gaussian model to approximate the *priori* and noise distribution and therefore use the Wiener Filter solution for reconstruction.

Besides, these Wiener filter based reconstruction algorithms are actually the same as the classical Tikhonov regularised inversion, a brief illustration based on SVD is given in (2.41)

$$\begin{aligned}
\boldsymbol{x}_{MAP} &= \boldsymbol{A}^T \left(\boldsymbol{A}\boldsymbol{A}^T + \lambda^2 \boldsymbol{I}\right)^{-1} \boldsymbol{y} \\
&= \boldsymbol{V}\boldsymbol{\Sigma}\boldsymbol{U}^T \left(\boldsymbol{U}\boldsymbol{\Sigma}^2\boldsymbol{U}^T + \lambda^2 \boldsymbol{U}\boldsymbol{U}^T\right)^{-1} \boldsymbol{y} \\
&= \boldsymbol{V}\boldsymbol{\Sigma} \left(\boldsymbol{\Sigma}^2 + \lambda^2 \boldsymbol{I}\right)^{-1} \boldsymbol{U}^T \boldsymbol{y} \\
&= \boldsymbol{V} \left(\boldsymbol{\Sigma}^2 + \lambda^2 \boldsymbol{I}\right)^{-1} \boldsymbol{\Sigma}\boldsymbol{U}^T \boldsymbol{y} \\
&= \boldsymbol{V} \left(\boldsymbol{\Sigma}^2 + \lambda^2 \boldsymbol{I}\right)^{-1} \boldsymbol{V}^T \boldsymbol{V}\boldsymbol{\Sigma}\boldsymbol{U}^T \boldsymbol{y} \\
&= \left(\boldsymbol{A}^T \boldsymbol{A} + \lambda^2 \boldsymbol{I}\right)^{-1} \boldsymbol{A}^T \boldsymbol{y} \\
&= \boldsymbol{x}_{tik}
\end{aligned} \qquad (2.41)$$

Recently, an improved statistical-based method was introduced for acoustic tomography reconstruction. It formulates the tomographic inverse problem as a state estimation and employs an unscented Kalman filter (UKF) to reconstruct the temperature and wind velocity fields [77, 79]. This Kalman filter method has the advantages of (1) dynamic reconstruction, which is able to

track the dynamic feature of the temperature and wind velocity fields; and (2) computational efficiency, which has the potential for online implementation. Details about this Kalman filter reconstruction will be given in the Chapter 4.

2.5.3 Waveform tomography reconstruction

The advancement of computing power enables us to solve the wave equation directly instead of constructing the forward problem based on ray theory. Not only the sound speed but also the attenuation can be reconstructed [80, 81], based on the waveform tomography reconstruction. The waveform tomography reconstruction records the boundary acoustic pressure measurements to fully reconstruction wave information, compared to TOF measurements for the ray theory reconstruction.

Furthermore, the rise of high throughput data acquisition hardware leads to the potential of the tomographic fully parallel data collection systems containing large numbers of transducers [82]. The improvement of the data collection system provides a large amount of data for better reconstruction accuracy using waveform tomography reconstruction method.

There are various advantages of the waveform tomography reconstruction, compared to the reconstruction method based on ray theory, including (1) better reconstruction accuracy when large diffraction as well as refraction occurs; and (2) better image resolution by using the full information of the wave propagation.

There are two ways to formulate the waveform tomography reconstruction methods, depending on whether the inverse problem is formulated in the time domain or in the frequency domain. Among the waveform reconstruction methods in the time domain, remarkable work includes the Propagation and Back Propagation method (PBP) [83, 84] and GPU implemented reconstruction [9]. In the frequency domain, they are split-step Fourier propagator [80] and Frequency-Domain Waveform Inversion [85]. Although this method is currently mostly discussed and investigated within the area of

medical imaging and seismology, it has the potential to be used for atmospheric imaging area in the future.

2.6 Acoustic tomography applications

In the past decades, acoustic tomography using TOF measurements has been continuously gaining interest in seismic imaging [6], medical ultrasound imaging [7-11], atmospheric imaging [17-19, 32, 34, 57, 58], ocean current monitoring [2-4] and many other areas [13, 86]. Examples of the acoustic tomography applications and the corresponding operating frequency ranges are listed in Table 2-4.

Table 2-4: Examples of the acoustic tomography applications

Application	Imaging targets	Transducer frequency
Civil infrastructure	Flaws	1-500 kHz
Forestry	Tree decay	10-100 kHz
Ocean tomography	Ocean currents	100-200 kHz
Atmosphere	Temperature and wind velocity	40 kHz
Agriculture	Spoilage/insects	0.5-3 kHz
Geophysical	Oil	1 Hz -2 kHz
Medical	Tissues	1-5 MHz

Among these applications, acoustic tomography, or more precisely ultrasound tomography has drawn much attention in the area of medical imaging. When the ultrasonic wave propagates through the tissue, the sound speed distribution can be reconstructed from TOF measurements. This sound speed distribution can be used to describe the tissue structure, which is similar to the acoustic tomography for atmospheric imaging the temperature and wind velocity. An important application of ultrasound tomography is breast cancer

detection, where the sound speed is used to detect cancerous tissue from normal breast tissue [80].

2.7 Summary

This chapter briefly reviewed the acoustic tomography technique from the perspectives of existing systems and applications, to fundamental theory, and to the cutting-edge acoustic tomography image reconstruction algorithms. The purpose of the chapter was to help understand the state-of-the-art acoustic tomography techniques, and the emerging or potential applications with maximum utilization of the many merits of acoustic tomography. The innovative work and scientific contribution of the thesis from these perspectives will be demonstrated subsequently in the following chapters.

Chapter 3 System design for lab-scale acoustic tomography system

3.1 Introduction

In this chapter, the design of the data acquisition system for acoustic tomography is presented first. The key features of the presented system include: (1) a transducer array, which consists of 16 acoustic transmitters and 16 acoustic receivers around the sensing area, to provide 192 TOFs for each frame's reconstruction; (2) a switching circuit for the semi-parallel data acquisition scheme; (3) NI DAQ for excitation signal generation and received waveform measurement; (4) a central control software for system control, received waveform monitoring and data storage. Secondly, an improved TOF estimation method based on the Akaike Information Criterion (AIC) is developed. Two improvements are studied in comparison with conventional weighted AIC TOF estimation methods to reduce crosstalk interference and sound reflections: (1) an adaptive window is applied for accurate AIC TOF estimation; (2) a phase correction method is developed to further improve the temporal resolution and noise robustness of the TOF estimation. The performance of the data acquisition system and TOF estimation method is evaluated in the lab-scale experiments.

3.2 Data acquisition system

3.2.1 System architecture

Figure 3-1 illustrates the block diagram of the acoustic tomography system architecture. The system consists of four parts, including the ultrasound transducer array, the switching circuit, and excitation and data collection module based on NI DAQ and the central control software on the PC. The ultrasound transducer array contains 16 transmitters and 16 receivers, placed with uniform spacing around the boundary of the sensing area. The 120° beam

angle (-12 dB) of the transducers allows the ultrasound signals from each transmitter to reach all 12 receivers on opposite boundary side. They form 16*12=192 different transducer pairs which are used to measure the TOFs. The switching circuit connects the transducer array with the NI DAQ card with a multiplexer array. Through the multiplexer array, a semi-parallel scanning scheme is applied that all transmitters are selected sequentially and waveforms from the receivers are measured simultaneously in two group. The NI DAQ card is used to provide the digital control signal for the multiplexer array of the switching circuit from the digital output (DO) channels. It also provides one analogue output (AO) channel for the excitation signal and 6 analogue input (AI) channels for received signal measurement. The central control software provides the switching scheme control, the received signal sampling, the excitation waveform generation and other measurement parameters can be setup in the central control software. The TOF estimation is then processed in the host computer.

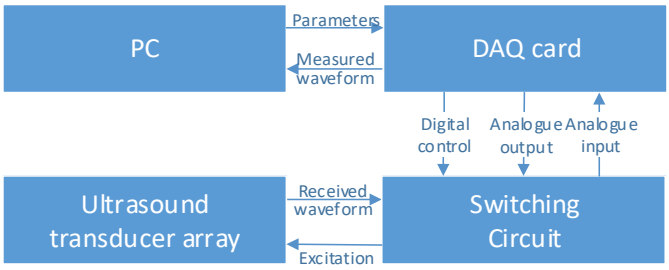

Figure 3-1: System diagram

3.2.2 Transducer array

The measurement setup of the transducer array is illustrated in Figure 3-2. Piezoelectric transducers model 400ST120 and 400SR120 were used to generate and receive the ultrasound signals respectively. The 120° beam angle (-12 dB) of the transducers allows the ultrasound signals from each transmitter to reach all 12 receivers on opposite boundary side, even for the transducer-receiver pair with large departure and arrival angle, for instance, the ray path between transmitter 4, and receivers 5 and 16. Besides, although

in each spot a pair of transmitter and receiver are placed next to each other, the corresponding back and forth ray paths cannot be considered as the same path. An example is the two ray paths, one from transmitter 4 to receiver 5 and the other from transmitter 5 to receiver 4. It can be seen from Figure 3-2 that these two ray paths cover different pixels. Therefore, a complete measurement for each temperature field comprises 192 TOF measurements from all transmitter-receiver pairs.

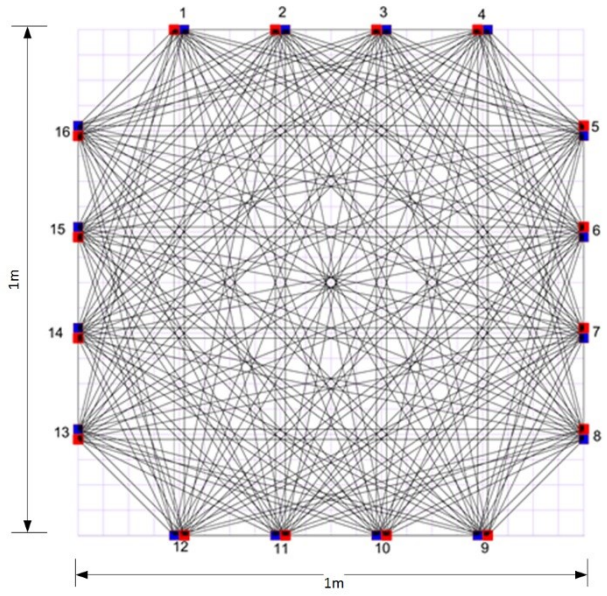

Figure 3-2: The transducer array with 16 transmitters (blue box) and 16 receivers (red box), which provides 192 ray path for TOF measurements.

The transducers operate at a resonant frequency of 40 kHz with 2 kHz bandwidth and the ultrasound transmission distance between the transducer pairs is up to 1.2 m in the experiment. To ensure the received waveforms have good SNR for TOF estimation, a 40 kHz sinusoid pulse with 20 Vpp amplitude and 200 μs duration, is used to activate the transmitter. Besides, for the TOF estimation for each transducer pair, the repetition period of two successive ultrasound transmission should be more than 20 ms. This 20 ms repetition period should be able to cover the travel time which varies from 1 ms to 5 ms for different ray distances, and the received ultrasound signal duration, which is about 15 ms (2 ms for the width of the received waveform main lobe and 12

ms for possible reflection echoes). If the repetition period is less than 20 ms, there will be considerable interference from the previous signal sent from another transmitter. An example of the excitation signal and the received signal is shown in Figure 3-3.

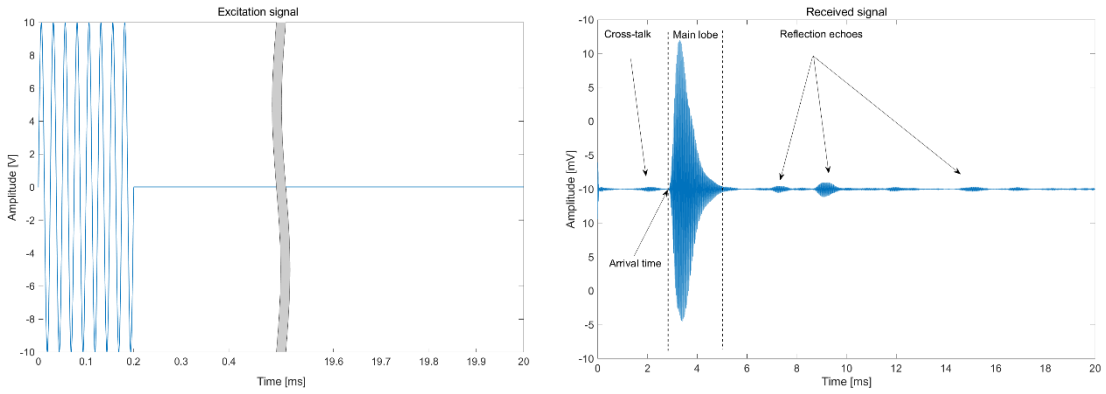

(a) (b)

Figure 3-3: An example of the excitation signal (a) and corresponding measured received signal (b).

3.2.3 Switching circuit

The switching circuit of the data collection system is a customised PCB. It provides a power supply connector, multiplexers connected to the NI DAQ for excitation signal generation and received waveform measurement, a sensor block for connection with all the transducers. The PCB is powered by a Tenma power supply.

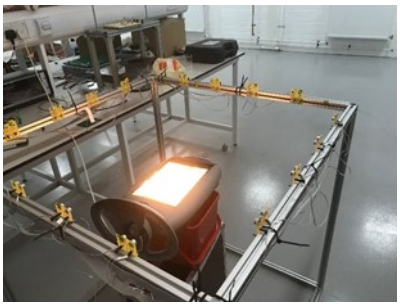

Figure 3-4: The experiment rig

The multiplexers perform the switching for the transmitters and receivers. The switching scheme is illustrated in Table 3-1. All transmitters are connected to

the analogue output (AO) channel through a 16-to-1 multiplexer and the excitation signal is sent to a selected transmitter sequentially. The maximum sampling frequency of the NI DAQ analogue input channel is 1.4 MHz, while the 40 kHz received signals require 200 kHz sampling frequency for each input channel. Therefore, only 6 waveforms can be measured at the same time using the NI DAQ, while there are 12 waveforms to be measured for each transmitter. In the experiments, all the transmitters are activated twice in a 40 ms time slot. During this 40 ms time slot, all the received waveforms at different receivers are measured in two groups. The total measuring time for each frame is 40 ms *16=640 ms.

Table 3-1: The semi-parallel switching scheme.

AO	AI1	AI2	AI3	AI4	AI5	AI6
T1-T4	R5	R6	R7	R8	R9	R10
	R11	R12	R13	R14	R15	R16
T5-T8	R1	R2	R3	R4	R9	R10
	R11	R12	R13	R14	R15	R16
T9-T12	R1	R2	R3	R4	R5	R6
	R7	R8	R13	R14	R15	R16
T13-T16	R1	R2	R3	R4	R5	R6
	R7	R8	R9	R10	R11	R12

As shown in Table 3-1, the analogue output (AO) is connected to all 16 transmitters and each of the 6 analogue inputs (AI) channels are connected to 4 specific receivers. For the transmitter selection, a 16-to-1 analogue multiplexer (AD7506) is used to channel the excitation signal from the DAQ analogue output channel to each transmitter. The transition time is around 0.7 μs. For the receiver selection, 6 4-to-1 differential analogue multiplexers (MPC509A) are used. The transition time of MPC509A is around 0.5 μs and

the connection between the input channels of differential multiplexers and the ultrasound receivers is shown in Table 3-2.

Table 3-2: Connection between the input channels of differential multiplexers to ultrasound receivers

	MUX1	**MUX2**	**MUX3**	**MUX4**	**MUX5**	**MUX6**
In 1	R1	R2	R3	R4	R5	R6
In 2	R5	R6	R7	R8	R9	R10
In 3	R7	R8	R9	R10	R11	R12
In 4	R11	R12	R13	R14	R15	R16

The multiplexers are digitally controlled by the NI DAQ card using 11 I/O ports P0.0 to P0.10. It is worth noting that the pairs of multiplexers 1 and 2, 3 and 4 and 5 and 6 can share 2 bits digital control variable. Therefore, among the control digits, there is a 1 bit enabling variable for all 7 multiplexers, ports (P0.1 to P0.4) for the control of the 16-to-1 transmitter multiplexer and ports (P0.5 to P0.10) for the control of 6 4-to-1 receiver multiplexers. The digital control ports are updated every 20 ms. The connection between the digital output and the multiplexer is shown in Figure 3-5.

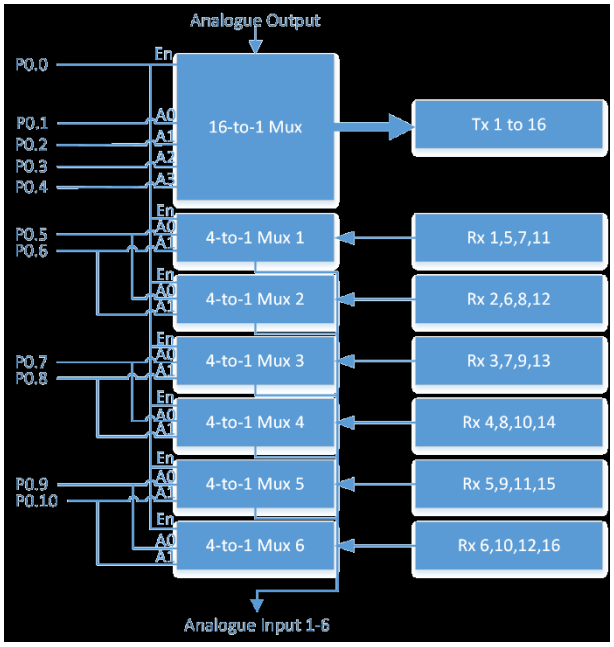

Figure 3-5: The connection of the between NI DAQ, the multiplexers and the transducers.

3.2.4 NI DAQ and central control software

The NI DAQ module used in this system is NI 6353, which coordinates the switching control, excitation signal generation and data collection of the ultrasound received waveform. The DAQ card has a multi-channel sampling rate up to 1.25 MS/s and 16 bits ADC resolution for the voltage reading of the received waveforms. Its analogue output channel, with the sampling rate of 2.86 MS/s and voltage range of ±10 V, generates the excitation signal for the ultrasound transmitters.

The central control software is programmed in the NI LabVIEW 2016 and NI 6353 DAQ card. Explanation of the key part of the system control and data collection module is based on the graphical user interface (GUI) shown in Figure 3-6.

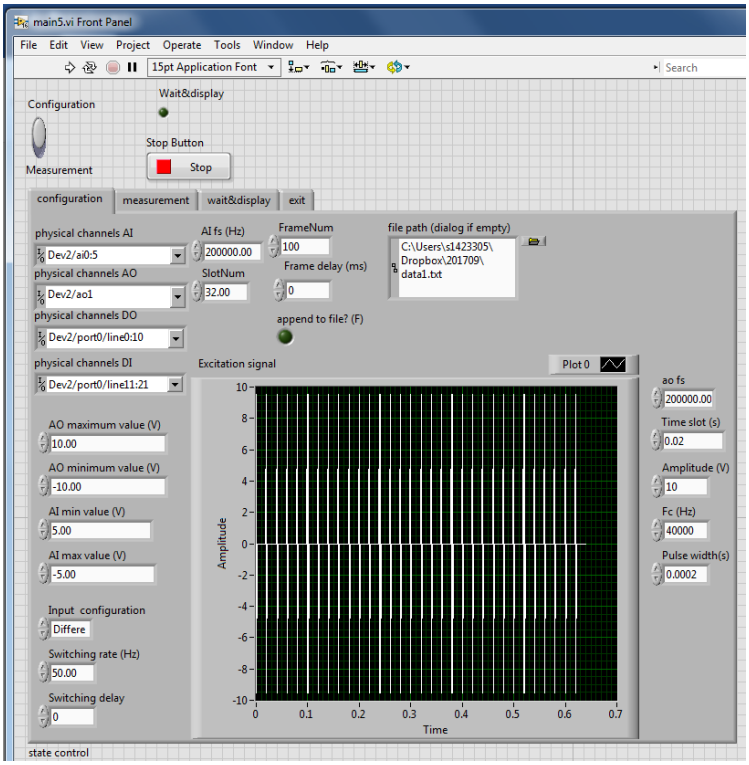

Figure 3-6: The front panel of the GUI

The top-level structure of the software is a state machine, which consists of 4 states, Configuration, Measurement, Display and Exit. Configuration is the default state and the software is waiting for the new command sent from the GUI. The state transition control is shown in Figure 3-7.

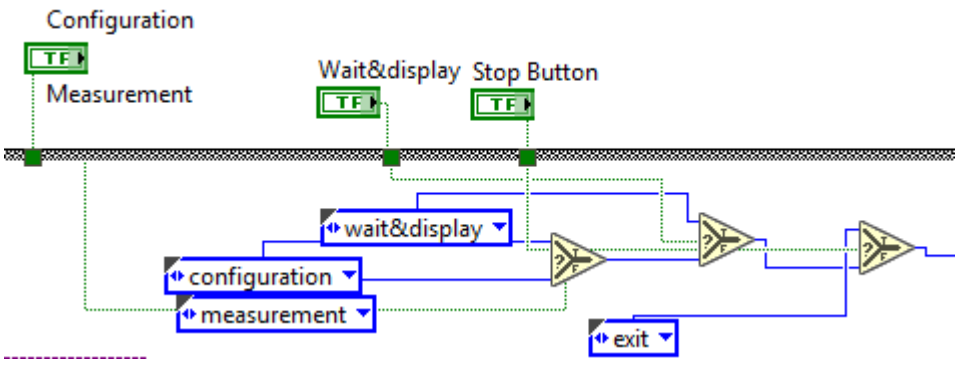

Figure 3-7: The control of the state transition

In the configuration state, the input waveform measurement, the excitation signal generation, the digital control signal generation, and other measurement

parameters are configured at the first time. Except for the channels' names and the receiver number 'RxNum', all other parameters can be modified and updated with a frequency of 500 ms, if the measurement process is complete. The excitation signal waveform generation is controlled by several parameters including the pulse width, time slot duration, sinusoid pulse central frequency and amplitude, and slot number. The generated excitation signal is displayed in the front panel and all the 32 pulses are directed to 16 transmitters during the measurement state. The frame delay controls the measured frame rate. The maximum frame rate is achieved if the frame delay is set to be 0. The start triggers of the two output channels, including the analogue out for excitation signal and the digital output for the control signal, are controlled by the start trigger of the analogue input channel. Therefore, the two output channels are synchronised with the analogue input channel.

In the measurement state, Producer/Consumer design pattern is used. After all the channels are configured, the data acquisition is executed in the producer loop. Then the data acquired in the producer loop are thrown into the queue. In the consumer loop, all the waveform data are saved into a text file. The Producer/Consumer design pattern provides a buffered communication between the data acquisition and data storage process, which helps to minimise the data loss.

Once the display button is pressed, the data acquisition in the producer loop is stopped immediately. After all the waveform data are saved in the consumer loop, the application turns to the display state. All the measured waveforms from different channels of different frames can be selected and displayed. Based on the displayed waveforms, the extent of the waveform distortion and the measurement SNR can be roughly estimated for system hardware debugging.

After the exit button is clicked, the repetition loop of the whole program is stopped. If the exit button is clicked during the measurement process, both the data acquisition loop and the data saving loop are stopped immediately.

3.3 Improved AIC TOF estimation

3.3.1 TOF estimation for acoustic tomography system

The major challenge in employing acoustic tomography for temperature field monitoring is to achieve high TOF measurement accuracy. An accurate TOF estimation is also essential in other applications, for example, ultrasonic ranging, positioning and synchronisation systems [36, 37], ocean tomography [3], ultrasonic breast cancer detection [7], and seismic wave arrival time estimation. To date, a number of TOF estimation methods have been developed in other disciplines.

Methods based on cross-correlation are usually used for TOF estimation. Such methods assume that the received signal is the time-shifted replica of the reference signal. The TOF is considered as the time delay [38, 39]. However, measurement accuracy is limited because 1) the received signal is corrupted by White Gaussian Noise (WGN) and interference due to channel crosstalk and sound reflections; and (2) the received signal waveform is not a time-shifted replica of the reference signal due to waveform distortion under a complex internal structure of the medium.

Estimating the TOF through parametric approximation through envelope extraction [38, 40, 41] has been widely used in ultrasound ranging and non-destructive testing. The received signal is usually modelled as a delayed Gaussian echo signal, and the TOF can be estimated after its envelope is extracted [42]. However, this Gaussian echo model is based on the assumption that the received signal is a backscattered echo from a flat surface reflector.

Numerous automatic arrival time estimation methods have been developed for seismic wave data analysis in geophysical applications. Short and long time-averaged ratio (STA/LTA) [43], phase arrival identification- kurtosis (PAI-K) [44] and other window-based methods calculate the characteristic function (waveform energy, absolute amplitude, kurtosis values, and many other

characteristic functions) within a predetermined window. The arrival times are estimated based on the maximum value of the derivative. Variations of the aforementioned methods are the modified energy ratio (MER) [45], the modified Coppens' method (MCM) [46], and the short-term or long-term kurtosis ratio (S/L-Kurt) [47]. These methods calculate the characteristic function from post- and pre-sample windows. The temporal index associated with the maximum ratio represents the arrival time. There are also numerous hybrid approaches based on these algorithms that attempt to more accurately estimate the TOF and these include the wavelet transform approaches [48] and the joint energy ratio (JER) [49].

The Akaike Information Criterion (AIC) and autoregressive (AR) techniques were first applied to TOF estimation of seismic wave data [50]. The arrival time is considered as a transition point that separates the signal into two different stationary processes. Therefore, the AIC function can be used to determine the transition point while the minimum AIC value indicates the optimum TOF estimate. However, the AR model's order should be determined heuristically and considering the noise level. To overcome this problem, Zhang [48] proposed a wavelet–AIC picker in which the AIC values are calculated directly from the seismogram using Maeda's formula [51], the latter of which computes the AIC directly from the waveforms without using the AR model coefficients. With some modification, the algorithms used in seismology can be applied to ultrasound signals [8].

Two issues remain before the AIC TOF estimation method is applied to our acoustic TOF tomography data. Firstly, the accuracy of the AIC TOF estimation method is affected by crosstalk interference and reflection echoes, both of which manifest in the received ultrasound signal. Secondly, the method is not robust against random noise, especially for the noise in close temporal proximity to the arrival time.

To solve these two problems, a modified phase corrected AIC TOF estimation method (PCAIC) is proposed for the acoustic tomography system. Two improvements are developed compared to the conventional weighted AIC TOF

estimation methods; the first improvement is an adaptive window applied to the received ultrasonic signal to reduce the effect of crosstalk interference and reflection echoes. The second one is phase correction to improve the temporal resolution and accuracy of the TOF measurements.

3.3.2 Conventional AIC TOF estimation

The TOF of an ultrasound pulse from the transmitter to the receiver is considered as a temporal transition point dividing the signal into two different stationary processes. The received signal is modelled as an autoregressive process (AR), and an AR-AIC TOF estimator was developed [50], which is defined as:

$$\mathrm{AIC} = 2P - 2\log(L(P,s,k)) \tag{3.1}$$

Where *P* denotes the number of AR coefficients and $L(P,s,k)$ is the likelihood function for the received signal *s*, and transition point k.

Later, Maeda directly calculated the AIC function without using the AR coefficients [51] to determine the transition point. The AIC function is defined as follows and the minimum AIC value indicates the optimum TOF estimate.

$$\mathrm{AIC}(k) = k\log(\mathrm{var}(s(1,k))) + N\log(\mathrm{var}(s(k+1,N))) \tag{3.2}$$

where N is the number of data samples in the received signal, $s(1,k)$ and $s(k+1,N)$ are the signal segments before and after the k-th point. The terms $\mathrm{var}(s(1,k))$ and $\mathrm{var}(s(k+1,N))$ represent the variances of the two signal segments.

An example of AIC TOF estimation is shown in Figure 3-8. The corresponding true arrival time is determined based on the sound speed at room temperature and the distance between the transmitter and the receiver. The AIC value was calculated from the signal within an adaptive temporal window for better AIC estimation performance. The enlarged figure shows that the true and

calculated TOFs are not identical. From Figure 3-8, it can be seen that the AIC function is not smooth and contains several local minima resulting in unreliable TOF estimation. Errors in the TOF estimation will exacerbate reconstruction errors. This is due to the fact that the reconstruction of acoustic tomography is an ill-conditioned inverse problem, whose solution is sensitive to small input perturbations [63].

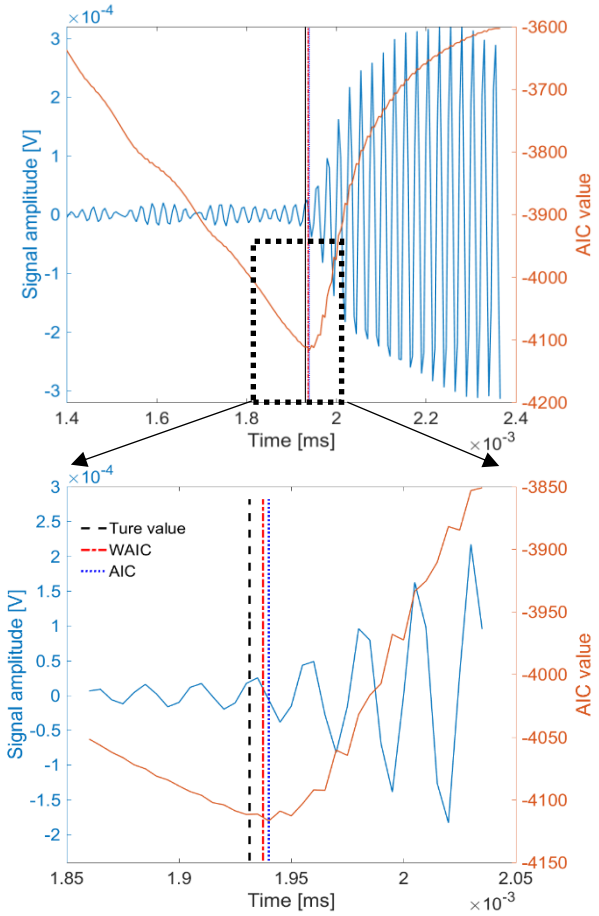

Figure 3-8: An example of AIC TOF estimation. The dashed vertical lines indicate the global minimum of the AIC value (blue), the weighted AIC value (red) and the true arrival time (black).

A weighted-average model was introduced by [8], to further improve the TOF estimation accuracy and noise robustness compared to using the global

minimum of the AIC function. The AIC weight is utilised to stabilise the estimation [87]. The normalised AIC weight is defined as follows.

$$w(k) = \frac{\exp\{-\Delta AIC(k)\}}{\sum_{i=1}^{N} \exp\{-\Delta AIC(i)\}} \tag{3.3}$$

where

$$\Delta \mathrm{AIC}(k) = \mathrm{AIC}(k) - \mathrm{AIC}(\min) \tag{3.4}$$

Then the weighted AIC (WAIC) TOF picker k_{WAIC} is calculated from the weighted average as shown in equation (3.5). A TOF estimation example using WAIC is shown in Figure 3-8.

$$k_{WAIC} = \sum_{k=1}^{N} w(k)k \tag{3.5}$$

However, as stated previously, two problems remain unsolved. Firstly, the WAIC TOF picker cannot accurately determine the TOF as crosstalk interference and multiple reflection echoes will temporally shift the WAIC picks. In this work, crosstalk interference is located at the beginning of the received signal due to ghosting effects in the data acquisition system. More specifically, a multiplexer array was used to switch between the transmitters and receivers. Due to the high switching rate and relatively large voltage swings (20 Vpp for transmission and 2-10 mVpp for reception), residual signals transfer across sequential channels. An example of TOF measurement using WAIC is shown in Figure 3-9. Without a proper temporal window to exclude the crosstalk interference, as shown in the top figure, the WAIC TOF estimation result will have a large estimation error. Similarly, when the reflection echoes are included for the WAIC TOF estimation, as shown in the bottom figure, the WAIC picks will not represent the correct first arrival time of the ultrasound pulse.

Moreover, the WAIC TOF estimation method is still not robust against random noise, especially against noise near the arrival time. Since the AIC picker finds the first arrival time by separating two locally stationary segments, it is difficult to decide which segment local noisy data samples belong to. Consequently, the TOF estimation error and variance increase. Figure 3-10 shows a histogram of WAIC TOF estimation results from 180 measurements when the travel distance and speed of sound are known. The standard deviation is 7.6 μs, and the relative root mean-square error (rRMSE) is 0.721%. According to the simulation results, a good reconstruction accuracy with image error less than 2% (with respect to Kelvin degree), requires that the rRMSE of the TOFs estimation should be no more than 0.4%. Therefore, the performance of the WAIC TOF estimation method must be further improved.

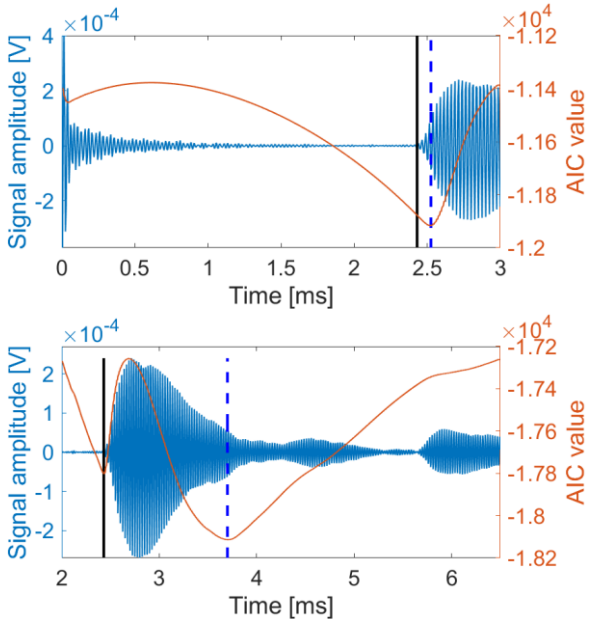

Figure 3-9: An example of WAIC TOF estimation, when there is crosstalk interference (top) or reflection echoes (bottom). The solid black line indicates the true arrival time whereas the blue dashed line represents the TOF estimation result.

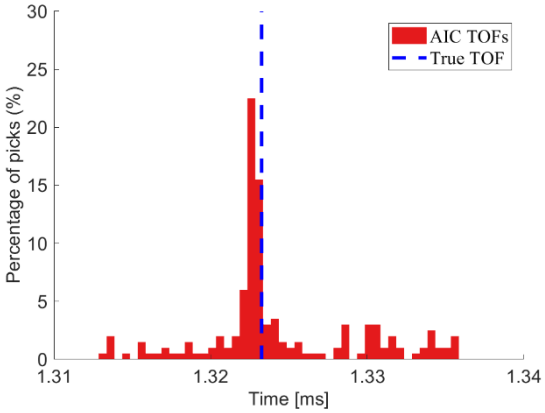

Figure 3-10: An example of WAIC TOF estimation results. The dashed blue line indicates the true TOF given the travel distance and sound speed.

The WAIC TOF estimation is improved in two aspects: (1) an adaptive window is employed to determine the search region before the WAIC estimation; and (2) a phase correction using time-domain interpolation is applied to further improve the accuracy and noise robustness. Details of these improvements are discussed in the following sections.

The SNR of the received waveform can be estimated using the ratio of the power of the two signal segments within the window, separated by the obtained TOF picks. Assuming the noise within the window is stationary and uncorrelated with the ultrasound signal, the SNR is defined as follows:

$$\mathrm{SNR}=10\log_{10}\left(\frac{\mathrm{var}(s(k+1,N))}{\mathrm{var}(s(1,k))}\right) \tag{3.6}$$

This SNR is determined by the TOF estimation results, and it can be used to eliminate unreliable TOF picks. When the SNR is lower than an experimental pre-defined threshold, 30 dB for the data set in this study, the corresponding TOF picks are discarded.

3.3.3 Adaptive window

The objective of the AIC estimation is to maximise the statistical feature difference between the signal segments received before and after the first

arrival time. Crosstalk and reflection interference should be reduced before AIC TOF estimation. Since reflection interference can be easily discriminated from the first arrival time, an adaptive window is designed primarily for the crosstalk interference. The adaptive window should include sufficient data samples around the time of arrival and exclude the crosstalk interference at the beginning of the received signal waveform.

An example of the window selection is shown in Figure 3-11. The received signal envelope $A(\tau)$ is extracted based on the Hilbert transform and its highest peak can help to find the signal's main lobe which corresponds to the first pulse arriving. The right side boundary of the search window, τ_{right}, is set to coincide roughly with the peak of the main lobe to exclude the reflection echoes. The left side boundary, τ_{left} is set to exclude large crosstalk interference. Assuming that the maximum temperature inside the sensing area is $T_{\max}$ and the corresponding TOF measurement is $\tau_{\min}$, a temporal point following the crosstalk interference event can identified as τ_{left}. To mark the onset of crosstalk interference, the instantaneous SNR_{inst} of the signal is used. The instantaneous SNR_{inst} is defined as follows:

$$SNR_{inst}(\tau) = 20\log(\frac{A(\tau_p)}{A(\tau)}) \tag{3.7}$$

where $A(\tau_p)$ is the peak value of signal amplitude in the main lobe, and $A(\tau)$ is the local sample amplitude at time τ.

The left boundary can be determined by searching for the point that τ_{left} is the furthest away from $\tau_{\min}$. All data samples within the interval $[\tau_{left}, \tau_{\min}]$ should have $SNR_{inst} > 25\ dB$.

The adaptive window is determined using the following steps.

Step 1: Extract the signal envelop $A(\tau)$ based on the Hilbert transform.

Step 2: Find the peak amplitude and set its corresponding arrival time as the right side boundary τ_{right} of the adaptive window.

Step 3: Calculate $\tau_{\min}$ from the known distance between transmitter and receiver and the maximum temperature measurement using equation(2.3).

Step 4: Calculate the instantaneous signal SNR within the temporal interval $[0, \tau_{\min}]$.

Step 5: Search for the left side boundary τ_{left}. Initially, let $\tau_{left} = 0$, then advance to the right until all the data samples within $[\tau_{left}, \tau_{\min}]$ have an $SNR_{inst} > 25\ dB$. If such a point cannot be found, for example, if the received signal's SNR is very poor within the interval $[0, \tau_{\min}]$, then set $\tau_{left} = \tau_{\min}$.

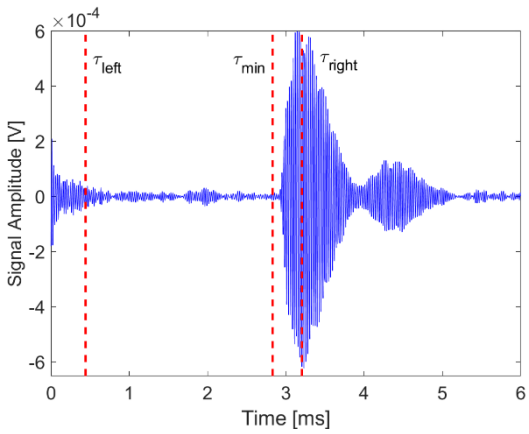

Figure 3-11: An example of the adaptive window selection. The data samples within $[\tau_{left}, \tau_{right}]$ are selected for TOF estimation. τ_{min} indicates the earliest arrival time of the ultrasound pulse.

3.3.4 Phase correction

The random noise in the temporal vicinity of the arrival time will affect the AIC estimation accuracy. Qu [11] took advantage of the similar characteristics of waveforms captured by neighbouring receivers and developed an AIC

neighbour cross correlation (AICNCC) method to improve the noise robustness of the TOF estimation. However, the transducer array in our experiment rig cannot provide the reference signal from neighbouring receivers to achieve the TOF estimation using cross-correlation. The phase information at the arrival time is exploited instead, which is not previously utilised by any AIC TOF estimation methods. Since the initial phase of the source signal is zero, the initial phase of the first arrival pulse should be zero as well. Therefore, the time of arrival is taken as the point closest to the AIC TOF pick whose instantaneous phase is zero. The temporal shift according to the instantaneous phase is subtracted from all estimated AIC TOF measurements to give the temporal index for the zero-phase points, i.e. the phase corrected AIC (PCAIC) TOF picks. As a result, the TOF estimation variance caused by the random noise is greatly suppressed.

The instantaneous phase estimation is also sensitive to the random noise. An example is shown in Figure 3-12 and Figure 3-13, respectively illustrating the instantaneous frequency and phase of the received signal. With reference to Figure 3-11, the signal segment before the main lobe contains wide-band random noise. The signal SNR of the data samples around the time of arrival is relatively low, thus the accuracies of the instantaneous frequency and phase are limited by the random noise. Therefore, it is challenging to use the instantaneous phase of the samples around the time of arrival for TOF correction. Instead, the phase offset of the main lobe can be used to find the zero-phase point for the PCAIC TOF estimation. The main lobe of the first arrival pulse represents a relatively narrowband signal having a frequency variation centred on the ultrasonic sensors' centre frequency f_c of 40 kHz. Its phase is changing periodically. The main lobe formulated by $A(\tau)\cos(2\pi f_c t+\varphi)$ can be decomposed using the Hilbert transform into a temporal envelope $A(\tau)$ and a temporal fine structure $\cos(2\pi f_c t+\varphi)$ [88]. The phase offset φ of the main lobe can be determined by calculating the phase delay between the temporal fine structure and the reference waveform $\cos(2\pi f_c t)$.

Moreover, it is possible to further improve the TOF estimation accuracy using interpolation techniques for data samples having a high SNR, especially within the signal's main lobe [89]. In order to improve the temporal resolution of the TOF estimate, time-domain interpolation is applied. Commonly used interpolation up-sampling methods cannot be directly used to improve the temporal resolution in this study as they rely on an antialiasing filter to reduce the artificial TOF variance [89]. Such an antialiasing filter will smooth the edge of the ultrasound pulse at the time of arrival, which results in undesirable estimation error for the TOF picker.

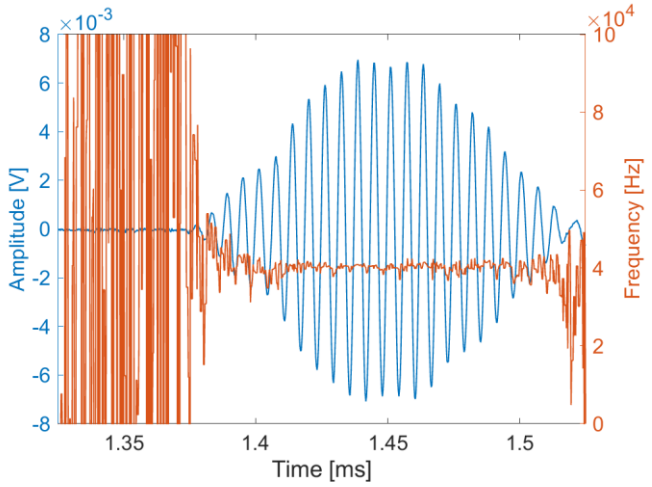

Figure 3-12: The instantaneous frequency (red) of the received signal (blue) around the arrival time. The signal is sampled at 200 kHz.

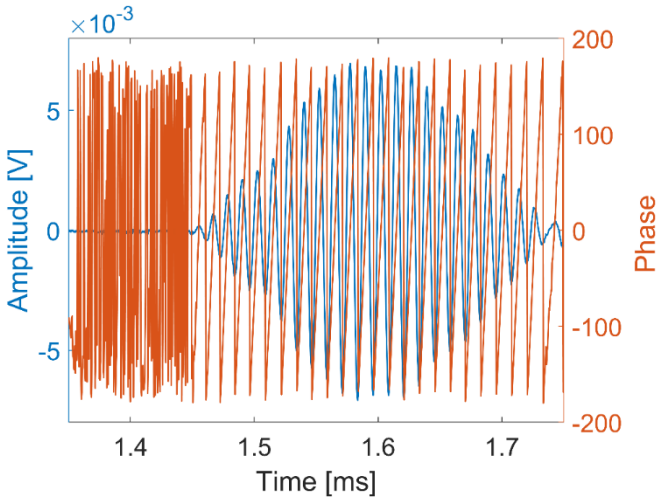

Figure 3-13: The instantaneous phase (red) of the received signal (blue).

Interpolation is only applied to the main lobe after the time of arrival for phase correction because: (1) within the main lobe, the signal segment has the required high SNR, and (2) the edge of the ultrasound pulse will not be smoothed. For the narrowband signal here, time-domain interpolation by a factor of 10 is applied using zero-padding and the Fast Fourier Transform (FFT) method.

The phase correction of the AIC TOF estimation is implemented in the following steps. An example is shown in Figure 3-14.

Step 1. Use a window-scaled Hilbert transform to extract a noisy, instantaneous phase $\theta(t)$ from the signal's main lobe (start from the TOF point determined by the AIC estimation).

Step 2: Calculate the temporal fine structure $s_c(\tau) = \cos(\theta(\tau))$. Apply the time-domain interpolation to increase the temporal resolution by a factor of 10.

Step 3: Build the reference cosine wave $s_{ref}(\tau) = \cos(2\pi f_c \tau)$. Calculate the phase delay $\Delta\theta$ between $s_c(\tau)$ and $s_{ref}(\tau)$ using the cross-correlation method.

Step 4: Correct the TOF using the phase delay $\tau = \tau_{AIC} - \frac{\Delta\theta}{2\pi f_c}$

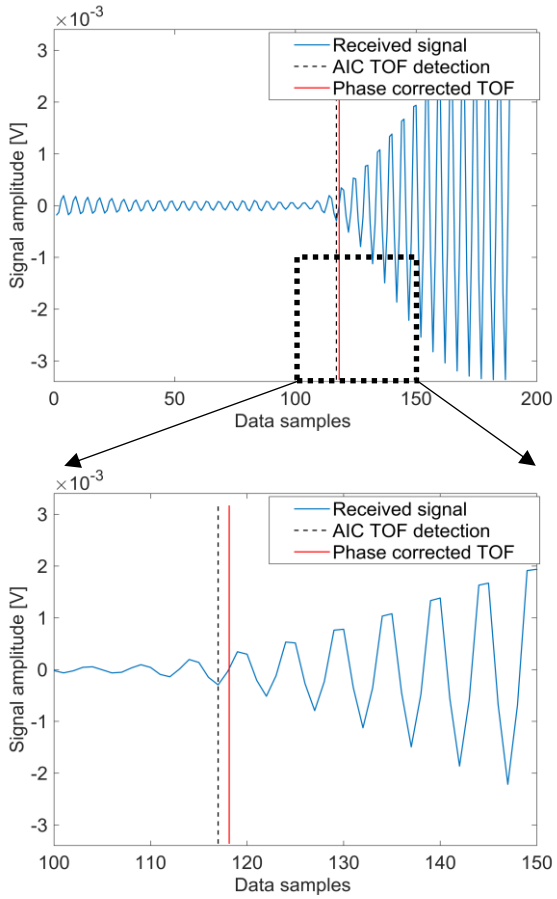

Figure 3-14: An example of phase correction of the AIC TOF estimation result.

3.4 Experimental evaluation

3.4.1 Ray length calibration

In the reconstruction procedure, the transducers are modelled as an equivalent point-transducer. Knowing the exact position of the transducers in the practical measurement setup plays a key role in achieving accurate tomographic image reconstructions. The transducer's acoustic centre, which is the location of the equivalent point-transducer, is not the same as the geometric centre. Therefore, it is difficult to measure the centre-to-centre distance L_{cc} between the transducers by measuring their physical separation. Instead, the TOFs can be exploited to estimate the centre-to-centre distance between transducers. The TOFs are measured 20 times using a constant and known speed of sound.

The averaged TOFs $\bar{\tau}$ and the corresponding speed of sound c (calculated based on the temperature) are used to calculate the distance $L_{cc} = \bar{\tau}c$.

It is difficult to calculate the ray length matrix $\boldsymbol{A}$ based on the transducer centre-to-centre distance L_{cc}. Alternatively, the L_{cc} can be used to correct the TOFs. The actual ray path (according to the centre-to-centre distance obtained from calibration) and the ideal ray path (according to the ray length matrix $\boldsymbol{A}$ used in the tomographic reconstruction) are usually within close physical proximity. Therefore, it is assumed that both actual and ideal ray paths traverse the same pixels inside the sensing area and as such, the measured TOF of the actual ray paths can be used to calculate the ideal model TOFs.

Along each ray:

$$\tau_{ideal} = \tau_{meas} \frac{L_{ideal}}{L_{cc}} \tag{3.8}$$

where L_{ideal} is the ideal model ray length used in the inverse problem, L_{cc} is the transducer centre-to-centre distance calculated from the measurement τ_{meas}.

In summary, during the calibration procedure, accurate transducer centre-to-centre distances L_{cc} are calculated from averaged TOFs measurements $\bar{\tau}$. In the measurement procedure, the L_{cc} of all the ray paths are used to estimate the ideal model TOFs, τ_{ideal}. Then, τ_{ideal} instead of τ_{meas} is used for the tomographic image reconstruction procedure.

The calibration accuracy is determined by the TOF estimation accuracy and the thermal couple measurement accuracy. The standard deviation is

$$\sigma_{Lcc} = L_{cc}\sqrt{\left(\frac{\sigma_{\bar{\tau}}}{\bar{\tau}}\right)^2 + \left(\frac{\sigma_c}{c}\right)^2 + \frac{2\sigma_{\bar{\tau}c}}{\bar{\tau}c}} \tag{3.9}$$

where $\bar{\tau}$ is average TOF calculated from 20 times measurement and $\sigma_{\bar{\tau}}$ is the standard deviation of $\bar{\tau}$ which is around 0.05 us, c is sound speed calculated based on the thermal couple temperature measurement and σ_c is the standard deviation, which is about 1.16 m/s. Calibration is conducted under the room temperature (296.13 K), where $c = 344.96\,\mathrm{m/s}$. The standard deviation σ_L depends on the ray distance, and for the shortest ray (the ray length is around 0.28 m), $\sigma_{Lcc} = 0.946\ mm$.

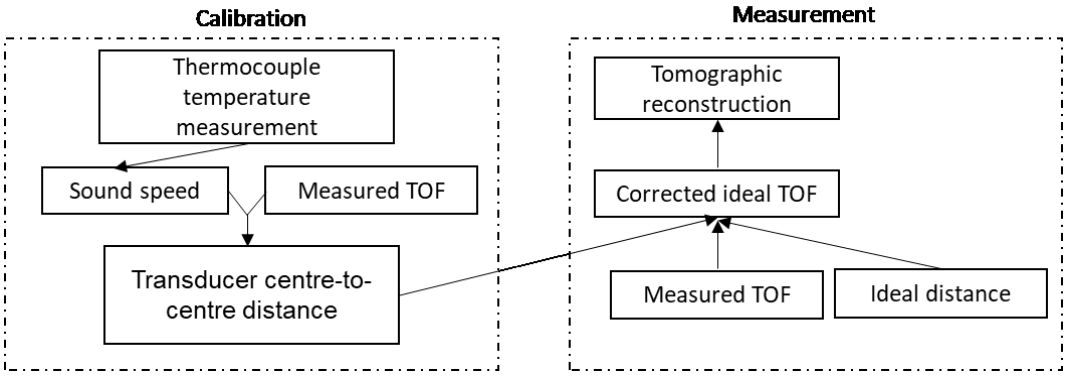

Figure 3-15: The diagram for calibration process

3.4.2 TOF estimation results

To assess the performance of the PCAIC TOF picker, the results using PCAIC is compared with those using the WAIC TOF picks. The tomographic system was tested on a known constant and uniform temperature field, and the true TOFs are calculated based on the temperature measured by thermal couple. A total of 200 waveforms were acquired from 4 receivers for the TOF estimation. The receivers were located at different distances and had a different angular orientation. The first 20 waveforms were used for calibration in both TOF estimation methods.

The examples of the TOF estimation from the received waveforms are shown in Figure 3-16. The adaptive window is able to locate the searching region excluding multiple reflection echoes and crosstalk interference. Sufficient data samples are selected using this adaptive window, enabling successful TOF estimation using both WAIC and the PCAIC methods.

Figure 3-17 shows the TOF picks histogram for the 180 waveforms from 4 ray paths. Compared to the WAIC picks, the PCAIC picks are more resilient to noise. The PCAIC method also achieves a significantly reduced estimation variance for all 4 ray paths. The improved performance is attributed to the phase correction procedure applied to the AIC TOF picks.

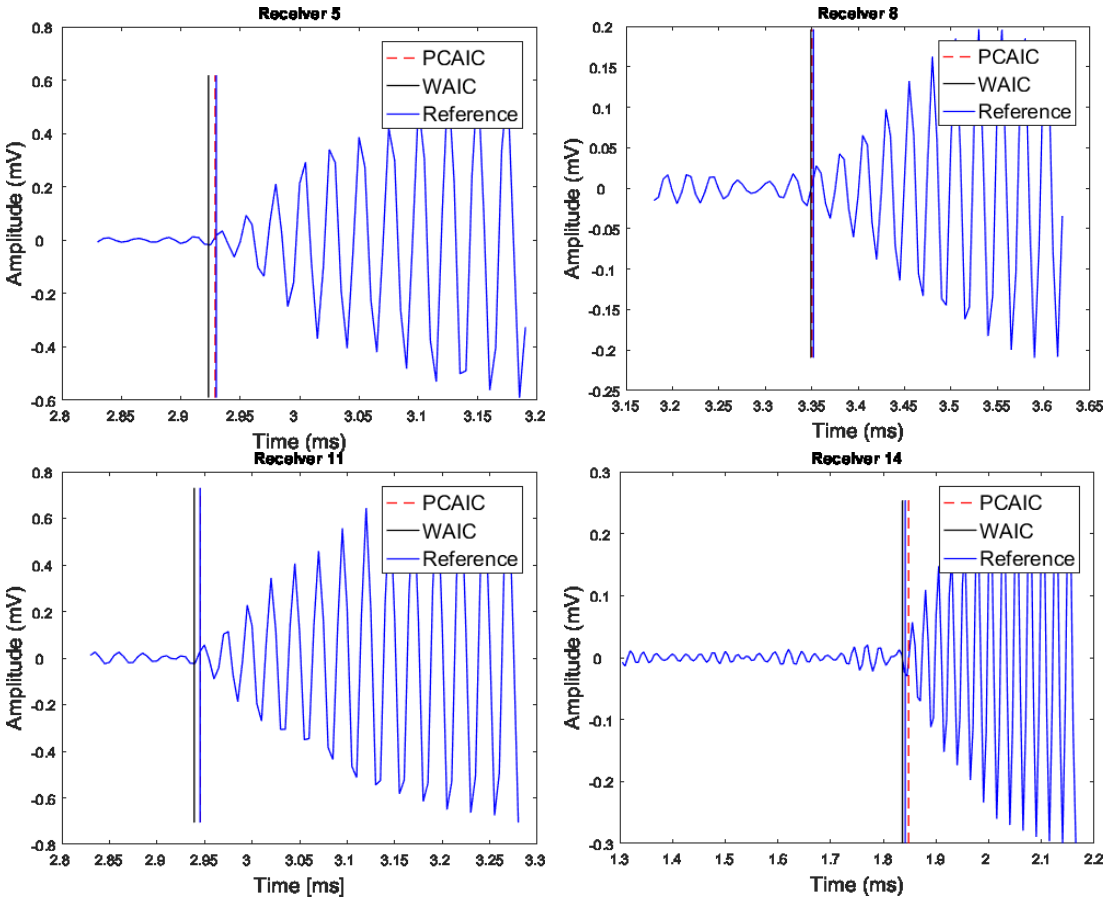

Figure 3-16: TOF estimation at 4 receivers (5th, 8th, 11th and 14th) from the 1st transmitter.

Table 3-3: TOF estimation comparison between WAIC and PCAIC method

Receiver	WAIC		PCAIC	
	rRMSE(%)	Std(ms)	rRMSE(%)	Std(ms)
5th	0.547	0.0128	0.163	0.00137
8th	0.358	0.0118	0.129	0.00101
11th	0.214	0.0063	0.127	9.1e-04
14th	0.573	0.0083	0.331	8.9e-04

Further details concerning the calibration results, the TOF estimation relative mean square error and standard deviation are listed in Figure 3-16.

Generally, the improved AIC TOF estimation method achieves better quantitative accuracy compared to the WAIC TOF picker in these experiments. As listed in Table 3-3, the rRMSE of the new method is much smaller than that of WAIC TOF methods. Furthermore, as shown in Figure 3-17, all TOFs picked by the PCAIC picker are within 1 sample point (5 μs) from the calculated TOF, whereas the TOFs picked by the WAIC method are spread over the range of 4-6 sample points. The standard deviation listed in Table 3-3 also suggests that our method has improved the noise robustness of the TOF estimation.

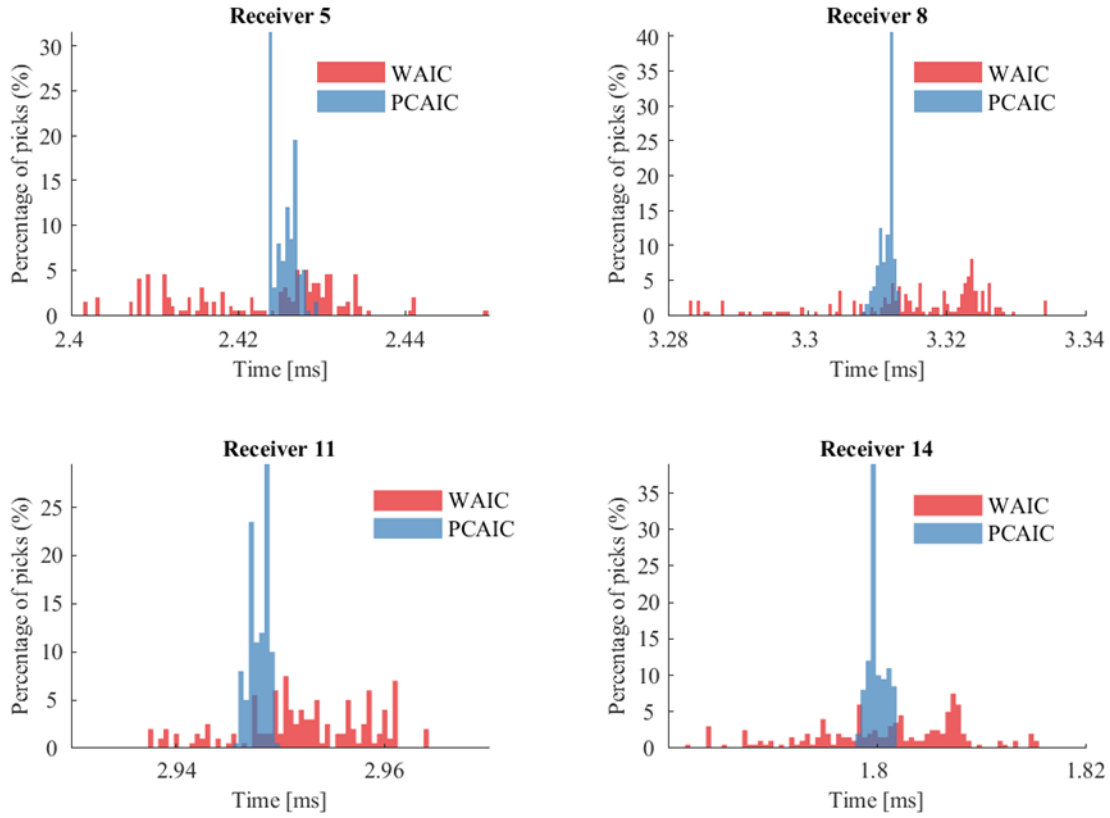

Figure 3-17 TOF picks histograms of WAIC and PCAIC methods using 180 waveforms from four ray paths measurements.

3.4.3 Tomographic reconstruction results

The performance of the proposed PCAIC TOF estimation method is validated experimentally. The regularisation parameters is set to be 0.1 for the experiments in this thesis. Using the corrected TOF measurements (after calibration) and the ray length matrix representing the ideal sensor array geometry, the Laplace's speed of sound distribution and the corresponding temperature field within the sensing area can be reconstructed.

In the experiments, two deterministic temperature fields were set up for reconstruction. In the first instance, an electric infrared heater was placed in the sensing area to heat the air slowly and create a smooth temperature field. In the second instance, a hair dryer was used to create a smaller hot spot in the sensing area. The acoustic tomography system was then used to reconstruct the temperature field.

It was difficult to evaluate the quantitative accuracy of the reconstruction results since the thermocouple was also heated by the infrared radiation, leading to a higher reading than the real temperature of the air. The heater was set at three power levels (400/800/1200W), heated the air for 5 minutes and then acquired measurements for each power level. Figure 3-18 shows the reconstructed temperature field. All reconstructions succeed in localising the heat source. The increasing air temperature is distinguishable as a function of increasing heater power. Using the TOF measurements based on the WAIC method, the reconstructed temperatures at the centre of the heated area are 28.86°C, 34.32°C and 35.48°C. Using the TOF measurements based on the PCAIC estimation method, the corresponding temperatures are 28.77°C, 29.86°C and 30.6°C. In line with our expectation, the tomographic reconstructions using the PCAIC method have fewer artefacts compared to the WAIC method.

In the second instance, a hair dryer was placed 5 cm above the sensing plane to blow hot air downwards into the sensing area and create a hotspot. A thermocouple was placed 5 cm beneath the sensing plane and at the centre of the heated air stream to compare the temperature reconstruction accuracy. After switching on the hair dryer and waiting until the temperature stabilised (34.8°C when the room temperature is 24.4°C), several measurements (20 frames) was taken to test the repeatability of the temperature field reconstruction. Figure 3-19 shows three consecutive reconstructions. The results indicate that the tomographic system has a good spatial resolution to resolve the small hot spot. The relative mean square error is 16.92% (with respect to Celsius) or 1.91% (with respect to Kelvin degree) at the centre of the reconstructed hotspot using TOF measurements based on the WAIC method. On the other hand, the relative means square error is significantly reduced using the PCAIC method; 5.12% (with respect to Celsius) or 0.58% (with respect to Kelvin degree). The standard deviation is 2.2 K using the WAIC method and 0.7 K using the PCAIC method. In conclusion, the proposed PCAIC TOF method can provide much better temperature field imaging performance.

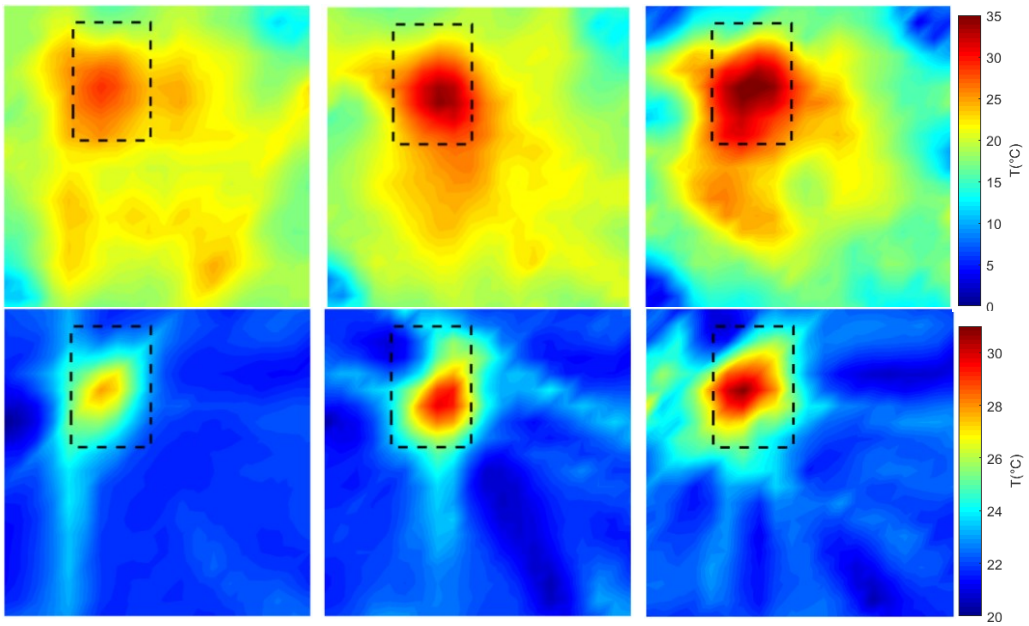

Figure 3-18: Reconstructed temperature fields at different heater power settings. From left to right, the power levels are 400 W, 800 W and 1200 W. The first row used the WAIC method and the second row used the PCAIC method. The dashed square indicates the physical position of the electric heater.

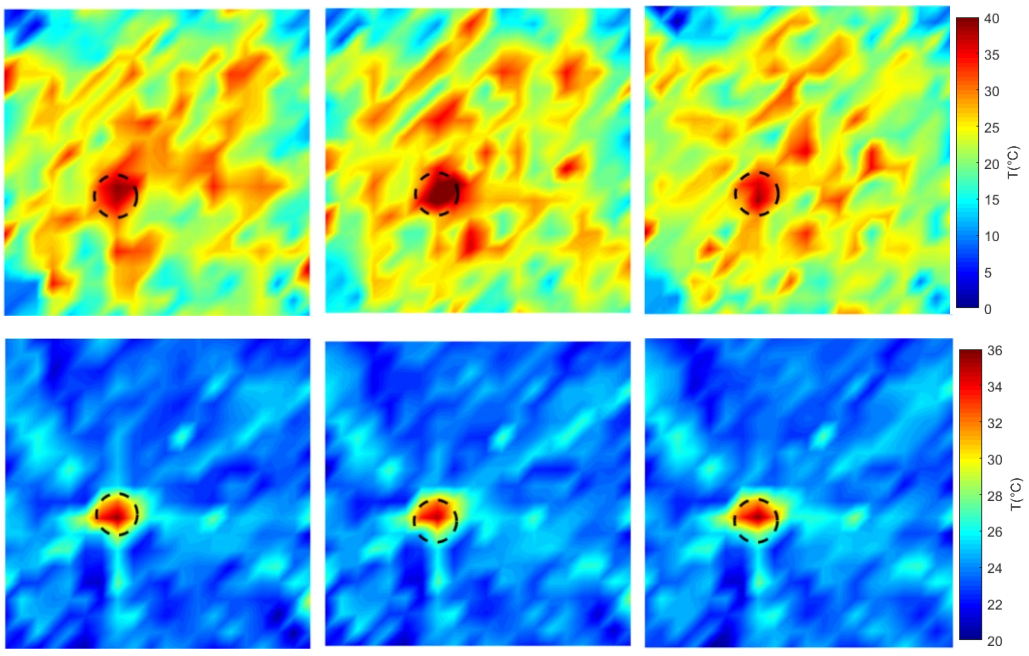

Figure 3-19: Three consecutive temperature field reconstructions using a hair dryer as a heater. The first row used the WAIC method and the second row used the PCAIC method. The dashed circle indicates the physical position of the heater.

3.5 Summary

In this chapter, the design of the data acquisition system and the TOF estimation method are presented. Their performance is thoroughly evaluated in terms of TOF estimation accuracy and image reconstruction quality. The data acquisition system provides 192 TOF measurements for each frame's reconstruction. The measuring time is 640 ms with the semi-parallel scanning scheme. The proposed PCAIC picker provides TOF estimation with a good quantitative accuracy (overall rRMSE less than 0.2%), high temporal resolution (0.25 μs) and robustness against the crosstalk interference and additional random noise. The TOF obtained from experimental data and using the proposed PCAIC method yielded temperature field reconstructions with improved quantitative accuracy and fewer image artefacts. In summary, the data acquisition and the proposed PCAIC picker together can produce accurate TOF data for the tomographic reconstruction of the lab-scale temperature field.

Chapter 4 Online time resolved reconstruction

4.1 Introduction

Concerns have been raised that the acoustic tomography system may lack a sufficient temporal resolution to reconstruct the dynamic features of some fast-changing temperature fields. Currently the system temporal resolution is 640 ms. The temperature changes during the 640 ms measuring time of each frame, for example, the motion of heat source, will blur the tomographic image and affect the temperature reconstruction accuracy. Research has tended to focus on accelerating the data acquisition process to improve the temporal resolution, with the use of broadband acoustic transducers and parallel data collection. Unfortunately, due to hardware limitations and the high implemental cost of the air ultrasonic transducers, it is generally difficult to apply a fully parallel data acquisition of measuring the TOFs along all transmission ray paths simultaneously. However, for large scale system, broadband acoustic transducers can be used for fully parallel data collection, details will be presented in chapter 6.

Besides, the minimum data acquisition time for each ray path is limited by the speed of sound and the size of sensing area. For our lab-scale experimental setup, the 1 m^2 sensing area requires a minimum of 20 ms measuring time for the longest ray path to propagate.

Besides reducing the data acquisition time, an alternative way is to use a smaller number of TOFs per frame and reconstruct an under-sampled tomographic image of the temperature field. Consequently, the measuring time per frame is largely reduced and the temporal resolution can be greatly improved.

Under-sampled reconstruction with fewer TOFs can improve the temporal resolution, but it also brings aliasing artefacts in image space. Compared to the conventional fully sampled tomographic reconstruction, this under-

sampled reconstructed image suffers from the lack of spatial resolution to resolve the temperature field distribution [73]. Fortunately, the redundancy of information in the temporal domain can be employed to solve this problem. The temporal redundancy provides additional information for the tomographic reconstruction of each frame. Serval time-resolved image reconstruction methods were developed [73, 90-94]. These time-resolved imaging algorithms were able to reconstruct the high-quality tomographic image from under-sampled data sets and resolved the dynamic changes which could not be recognised by the conventional fully-sampled tomographic reconstruction. Generally, these time-resolved reconstruction methods can be categorised into three main branches.

In the first branch, the temporal redundancy across consecutive frames is used to build different regularisation term in the algebraic-based reconstruction. These regularisations are designed for specific application, such as temporal smoothness regularisation for general cases, spatial-temporal total variation for the temporal piecewise constant data, temporal non-local means regularisation for the structural similarity between frames, and nuclear norm regularisation for the low rank structure of a time series data [92, 93, 95]. These methods are able to reconstruct images with good quantitative accuracy using very few data. However, most of the methods require iterative reconstruction, which is more suitable for offline reconstruction rather than online reconstruction for real-time monitoring.

Another approach of the time-resolved reconstruction method is based on the Karhunen Louve transform (KLT), where the temporal redundancy information is extracted from the data [73, 96-98]. It utilises the sparse representation of image series under KLT domain with the temporal basis functions. The temporal basis functions can be obtained from under-sampled reconstructed images. However, these methods rely on the implicit assumption that the principal basis functions estimated from the low-resolution data closely approximate the original KLT basis functions. Clearly, this approximation requires sufficient number of measurements in the training data. Besides, it is

also an offline iterative reconstruction method and not suitable for real-time monitoring.

Thirdly, there is also a statistical approach of time-resolved reconstruction based on the Kalman filter or the unscented Kalman filter [77, 79]. The tomographic reconstruction problem is formulated as a state estimation problem and the temporal redundancy can be interpreted into the state transition model of the Kalman filter. It has the advantages of fast reconstruction and online reconstruction potential. However, there is still a problem with this approach. The Kalman filter reconstruction is optimal estimator only when all the error is Gaussian and the mean and standard deviation of the error are known, but it is not always the case[99]. Besides, to solve the inverse problem here, it is not necessary to use the unscented Kalman filter.

In this chapter, a novel online time-resolved reconstruction (OTRR) method is presented, which is able to reconstruct high quality time-resolved images using fewer TOFs per frame. Our main novelties can be summarised as follow. Firstly, by exploiting the redundancy of information in the temporal domain, a temporal regularisation is designed based on an adaptive AR model to reduce the required amount of TOF data per frame. A sliding overlapping window is applied to further improve the reconstruction accuracy. Secondly, a non-iteration scheme is used for the time-resolved reconstruction. Instead of conducting iterative calculation upon each data set until convergence, the recursive reconstruction process performs a sliding iteration over each data segment. For the reconstruction of each frame, the online computation is non-iterative.

4.2 Online time-resolved reconstruction (OTRR)

4.2.1 Problem statement

The forward problem of acoustic tomography establishes the relationship between the TOF measurements and the speed of sound which is dependent on temperature. The forward problem for frame t is defined as:

$$\boldsymbol{y}_t = \boldsymbol{A}_t \boldsymbol{x}_t \tag{4.1}$$

Here $\boldsymbol{x}_t \in \mathbb{R}$ denotes the tomographic image vector which describes the travel speed reduction distribution and N is the pixel number. $\boldsymbol{y}_t \in \mathbb{R}$ as the TOFs measurement vector and M is the measurement number for each frame The temporal resolution of the acoustic tomography system can be greatly improved if fewer TOFs are used for the reconstruction per frame. However, the resolution is improved at the cost of spatial resolution. Reconstruction with fewer TOFs will introduce aliasing artefacts in the image space. To solve this problem, temporal regularisation is applied in the proposed time-resolved tomographic reconstruction method and more details are presented below.

The TOFs and images for all the frames of the tomographic images can be stacked as columns and denoted it as $\boldsymbol{X} = [\boldsymbol{x}_1, \boldsymbol{x}_2, ..., \boldsymbol{x}_T]$ and $\boldsymbol{Y} = [\boldsymbol{y}_1, \boldsymbol{y}_2, ... \boldsymbol{y}_T]$, where T is the number of frames. Then the forward problem can be written as $\boldsymbol{Y} = \boldsymbol{AX}$, where the block diagonal matrix $\boldsymbol{A}$ is given as $\boldsymbol{A} = diag\{\boldsymbol{A}_1, \boldsymbol{A}_2, ..., \boldsymbol{A}_T\}$.

The regularised inverse problem is defined below.

$$\min_{X} \|\boldsymbol{Y} - \boldsymbol{AX}\|_F + \alpha_1 \sum_{t=1}^{T} \|\boldsymbol{F}\boldsymbol{x}_t\|_2 + \alpha_2 \boldsymbol{R(X)} \tag{4.2}$$

where $\|\boldsymbol{F}\boldsymbol{x}_t\|_2$ is used to enforce spatial smoothness for each frame, and $\boldsymbol{F}$ is a linear differential operator, which is built based on the 3 by 3 differential kernel

$\begin{bmatrix} 0 & -1 & 0 \\ -1 & 4 & -1 \\ 0 & -1 & 0 \end{bmatrix}$ [62]. $\boldsymbol{R(X)}$ is used to enforce temporal regularity for the time series. α_1 and α_2 are two predefined regularisation parameters.

4.2.2 Temporal regularisation

Various temporal regularisation methods have been developed to improve the spatial resolution for the time-resolved tomographic reconstruction. For example, in the case of Electrical Resistance Tomography (ERT) where the consecutives frames can be well approximated by a piecewise constant function, the spatial-temporal Total Variation (TV) regularisation is selected for the tomographic reconstruction [92]. With dynamic MRI used for medical imaging, where the MRI sequence can be approximated by a low rank matrix, the nuclear norm can be used for tomographic reconstruction [95]. Another case is the 4D CT, where the structure similarity across consecutive frames is used to build the non-local mean regularisation for reconstruction. However, these regularisation are not suitable to be used here for two reasons: (1) the dynamic temperature field is generally smooth on the time domain, and it does not have the aforementioned features; and (2) spatial-temporal TV, non-local mean regularisation and low rank regularisation methods require iterative computation, which is not be suitable for fast online reconstruction.

Temporal smoothing regularisation is applied in the proposed Online time-resolved reconstruction (OTRR) method based on the assumption of similarity of the reconstructed frames [90]. Apart from this temporal smoothing regularisation, no other *priori* knowledge is used for any specific target temperature field. Generally, the temporal regularisation is designed based on the difference among successive frames.

$$\boldsymbol{R(X)} = \sum_{t=2}^{T} \left\| \boldsymbol{x}_t - \boldsymbol{x}_{t-1} \right\|_2^2 \tag{4.3}$$

In the cases when the dynamic characteristics happen within the region of interest and the motion is hard to predict, using more frames instead of only

adjacent time frames will significantly improve the reconstruction quality [90]. Here an adaptive AR model is applied. For a group of time series $\boldsymbol{X}=\left[\boldsymbol{x_1},\boldsymbol{x_2},...,\boldsymbol{x_T}\right]$ the AR prediction for frame t $\boldsymbol{x_t^*}$ is defined as

$$\boldsymbol{x_t^*}=\sum_{k=1}^{T} w_t(k)\boldsymbol{x_k}=\boldsymbol{X}\boldsymbol{w_t} \tag{4.4}$$

where $\boldsymbol{w_t}\in\mathbb{R}$ is a normalised AR weights defined as:

$$w_t(k)=\frac{e^{-(k-t)^2/\rho}}{\sum_{k=1}^{T} e^{-(k-t)^2/\rho}},\ k=1,2,...,T \tag{4.5}$$

T is the number of frames within the group and ρ is the smoothing parameter. Therefore, a penalty term based on this AR model is defined as

$$\boldsymbol{R(X)}=\sum_{t=1}^{T}\boldsymbol{R}(\boldsymbol{x}_t)=\sum_{t=1}^{T}\left\|\boldsymbol{X}\boldsymbol{w}_t-\boldsymbol{x}_t\right\|_2 \tag{4.6}$$

4.2.3 Iterative reconstruction

To solve the inverse problem, the inverse problem is firstly divided into two sub problems based on the forward–backward splitting method (FBS) [68].

$$\boldsymbol{X}^{i+1/2}=\arg\min_{\boldsymbol{X}}\left\|\boldsymbol{Y}-\boldsymbol{A}\boldsymbol{X}\right\|_{\boldsymbol{F}}+\alpha_1\sum_{t=1}^{T}\left\|\boldsymbol{F}\boldsymbol{x}_t\right\|_2 \tag{4.7}$$

$$\boldsymbol{X}^{i+1}=\arg\min_{\boldsymbol{X}}\left\|\boldsymbol{X}-\boldsymbol{X}^{i+1/2}\right\|_{F}+\alpha_2\boldsymbol{R(X)} \tag{4.8}$$

Sub-problem 1 involves the data fidelity and spatial regularisation term and does not include the temporal regularisation term. Therefore, each frame can be reconstructed independently.

$$x_t^{i+1/2}=\arg\min_{x}\left\|\boldsymbol{y}_t-\boldsymbol{A}_t\boldsymbol{x}_t\right\|_2+\alpha_1\left\|\boldsymbol{F}\boldsymbol{x}_t\right\|_2 \tag{4.9}$$

It can be solved by the modified SIRT method [62], which is defined in equation(2.22).

$$\boldsymbol{x}_t^{i+1/2,m} = \boldsymbol{x}_t^{i+1/2,m-1} + \mu \boldsymbol{P}\boldsymbol{A}_t^T \boldsymbol{W}(\boldsymbol{y} - \boldsymbol{A}_t \boldsymbol{x}_t^{i+1/2,m-1}) - \lambda\mu \boldsymbol{P}\boldsymbol{F}^T \boldsymbol{F}\boldsymbol{x}_t^{i+1/2,m-1} \quad (4.10)$$

$\boldsymbol{P}$ is the diagonal preconditioner $\boldsymbol{P} = diag(1/LP_1, 1/LP_2, ..., 1/LP_N)$, and $\boldsymbol{W}$ is the Normalised weight operator $\boldsymbol{W} = diag(1/LR_1, 1/LR_2, ..., 1/LR_M)$, where $LP_j = \sum_{i=1}^{M} a_{i,j}$, $LR_i = \sum_{j=1}^{N} a_{i,j}$. m denotes the inner iteration index for sub problem 1 and step size μ is set to 1.

Then the images are stacked as:

$$\boldsymbol{X}^{i+1/2} = \left[\boldsymbol{x}_1^{i+1/2}, \boldsymbol{x}_2^{i+1/2}, ..., \boldsymbol{x}_T^{i+1/2} \right] \quad (4.11)$$

Which can be used to solve the sub-problem 2.

For the sub-problem 2

$$\begin{aligned} \boldsymbol{X}^{i+1} &= \arg\min_{\boldsymbol{X}} \left\| \boldsymbol{X} - \boldsymbol{X}^{i+1/2} \right\|_F + \sum_{t=1}^{T} \alpha_2 \left\| \boldsymbol{X}\boldsymbol{w}_t - x_t \right\|_2 \\ &= \arg\min_{\boldsymbol{X}} \sum_{t=1}^{T} \left\{ \left\| x_t^{i+1/2} - x_t \right\|_2 + \alpha_2 \left\| \boldsymbol{X}\boldsymbol{w}_t - \boldsymbol{x}_t \right\|_2 \right\} \end{aligned} \quad (4.12)$$

Once the image series $\boldsymbol{X}^{i+1/2}$ is obtained, the sub-problem 2 can be solved using one step gradient descent. This is because that there is no need to solve this sub-problem 2 very precisely for each i-th outer iteration.

$$\boldsymbol{x}_t^{i+1} = \boldsymbol{x}_t^{i+1/2} + \alpha_2 (\boldsymbol{X}\boldsymbol{w}_t - x_t^{i+1/2}) \quad (4.13)$$

Then

$$\boldsymbol{X}^{i+1} = \left[\boldsymbol{x}_1^{i+1}, ..., \boldsymbol{x}_T^{i+1} \right] \quad (4.14)$$

In summary, the reconstruction process is illustrated in Table 4-1.

4.2.4 Segmentation for large group of data set

For the reconstruction of a large number of tomographic images, it is necessary to divide the whole data set into smaller segments and the reason is twofold. Firstly, the abovementioned time-resolved imaging method yields iterative procedures considering all the TOFs are measured and stored in advance, which will result in large computational cost. Secondly, it is not necessary to use all time frames to calculate the temporal regularisation term since the similarity between frames with large temporal distance is very weak. In this study, each data segment consists of 16 frames' TOFs, and the frames of each segment can be reconstructed separately.

Table 4-1: The iterative reconstruction process to solve equation (4.7) and (4.8)

Input: $\boldsymbol{Y}$ $\boldsymbol{A}$ IterNo, $\boldsymbol{F}$, w,K, ε

Ourput: $\boldsymbol{X}$

Initialise: $\boldsymbol{X^0 = 0}$

For i=1 : IterNo

For t=1:K

$$\boldsymbol{x}_t^{i+1/2,m} = \boldsymbol{x}_t^{i+1/2,m-1} + \mu \boldsymbol{P}\boldsymbol{A}_t^T \boldsymbol{W}(\boldsymbol{y} - \boldsymbol{A}_t \boldsymbol{x}_t^{i+1/2,m-1}) - \lambda\mu \boldsymbol{P}\boldsymbol{F}^{\boldsymbol{T}} \boldsymbol{F}\boldsymbol{x}_t^{i+1/2,m-1}$$

End

$$\boldsymbol{X}^{i+1/2} = \left[\boldsymbol{x}_1^{i+1/2}, \boldsymbol{x}_2^{i+1/2}, ..., \boldsymbol{x}_T^{i+1/2}\right]$$

$$\boldsymbol{x}_t^{i+1} = \boldsymbol{x}_t^{i+1/2} + \alpha_2(\boldsymbol{X}^{i+1/2}\boldsymbol{w}_t - x_t^{i+1/2})$$

$$\boldsymbol{X}^{i+1} = \left[\boldsymbol{x}_1^{i+1}, \boldsymbol{x}_2^{i+1}, ..., \boldsymbol{x}_T^{i+1}\right]$$

If $\left\|X^{i+1} - X^i\right\|_F \le \varepsilon$ break

End

However, with the use of AR weights for temporal regularisation, the reconstructed images at both ends of the segments will have a larger reconstruction error compared to the images in the middle. An example of the reconstruction errors of 16 frames within one segment is given in Figure 4-1. It is clear that the reconstruction errors of the middle frames are much smaller than the frames at both ends.

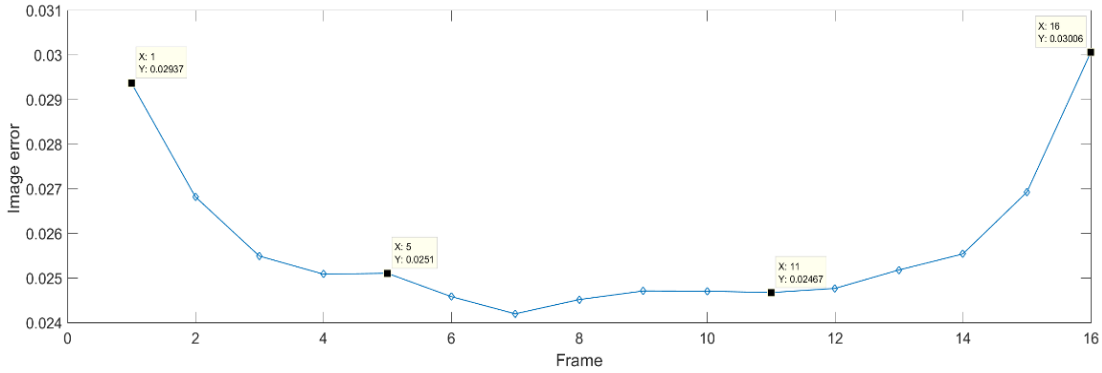

Figure 4-1: An example of the reconstruction image errors within the first segment of 16 frames.

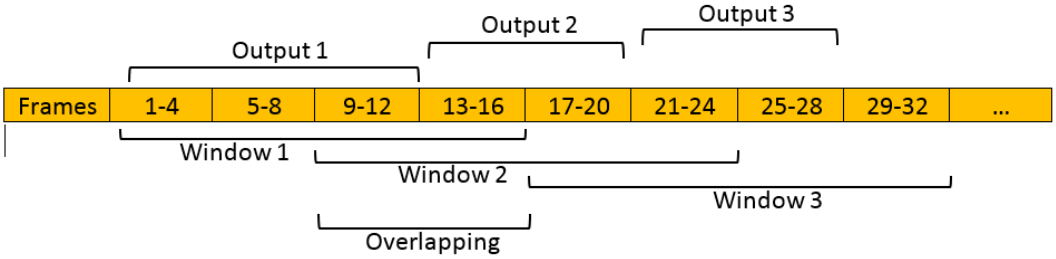

Figure 4-2: Data segmentation based on a sliding window.

For better reconstruction accuracy, it is necessary to make sure that all the frames are reconstructed when they are at the middle of the segments. Therefore, the overlapped windowing data segmentation is used instead of non-overlapped windowing. An example of the overlapped windowing data segmentation is shown in Figure 4-2. A sliding window with the length of 16 and 50% overlapping is applied to the TOF data sets. The 8 frames within the middle of each segments (i.e. the frame 5-12 for the window 1 and frame 13-

20 for the window 2) will be reconstructed, since they are considered to have lower reconstruction error. Special cases are the first and last segments, where the reconstruction outputs will also contain the frame in the beginning and ending. Due to the 50% overlapping sliding window, most of the frames are reconstructed when they behave as the middle frames of different segments. A comparison is shown in Figure 4-3. By using the overlapping window, the reconstruction errors of the frames at both ends of non-overlapping window are reduced.

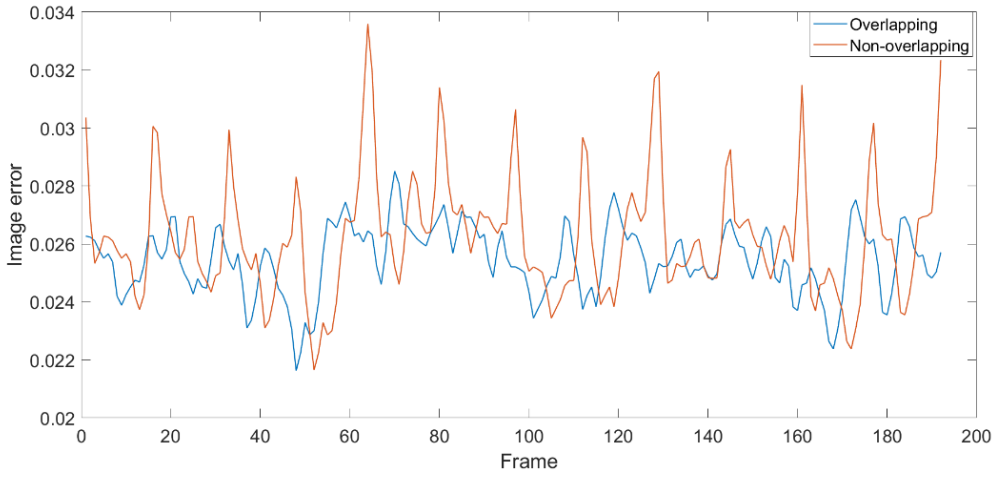

Figure 4-3: The comparison of the reconstruction error with non-overlapping segmentation (red) and 50% overlapping segmentation (blue)

The overlapping percentage is adjustable. A larger overlapping percentage helps to improve the temporal smoothness and continuity for the time series images, whereas, it also increases the computational cost. An appropriate overlapping percentage should be chosen for each specific application.

4.2.5 Non-iterative online reconstruction

Iterative computation is conducted to solve the two sub-problems on each data segment ($\boldsymbol{Y} = [\boldsymbol{y}_1, \boldsymbol{y}_2, ..., \boldsymbol{y}_T]$) until convergence, which is not suitable for online monitoring system due to the large computational cost. To accelerate the reconstruction process, a recursive online reconstruction is applied. As shown in Figure 4-4, the general idea is to use the reconstruction results of the

previous data segment as the initial guess to reconstruct the frames in next segment. Higher overlapping percentages help to improve the temporal correlation between segments. As a result, the outer loop iteration number IterNo in Table 4-1 and the computational cost can be greatly reduced. In this chapter, the overlapping percentage can be set to the highest level. For the 16 order AR model here, the overlapping percentage is increased to 15/16=0.9375, which enables us to cancel the outer loop and set the IterNo to one. Since both sub-problems are solved non-iteratively, the reconstruction of each data segment becomes non-iterative. A special case is the first segment, since it is solved iteratively.

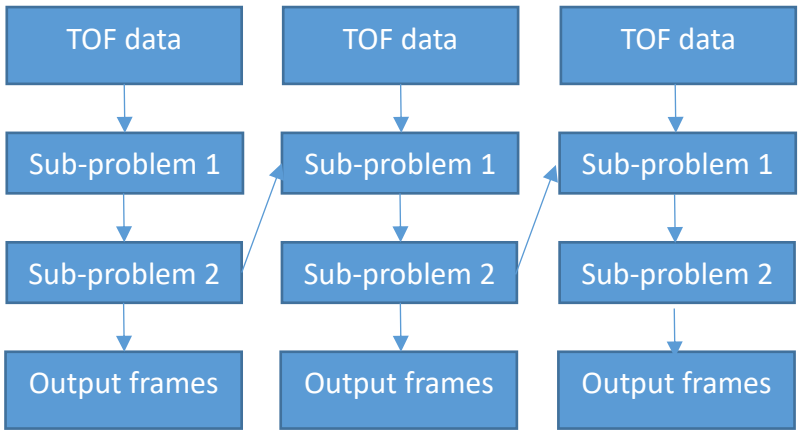

Figure 4-4: The recursive reconstruction process

4.3 Connection with previous works

The dynamic tomographic reconstruction method using the Kalman filter has been successfully applied in acoustic tomography, electrical tomography, dynamic MRI and etc [77, 79, 95, 100]. Different from algebraic-based algorithm, the Kalman filter reconstruction is a statistical-based method, which formulates the tomographic inverse problem as a state estimation. In the reconstruction the temperature distribution utilises both the information from TOFs measurements and the *priori* knowledge from the temporal evolution from the state transfer model [100]. Similar to the OTRR methods, this method also has the advantages of time-resolved imaging and non-iterative

reconstruction. Generally, the state transfer and measurement equations are presented below

$$\boldsymbol{x}_t = \boldsymbol{P}\boldsymbol{x}_{t-1} + \boldsymbol{w}_t \tag{4.15}$$

$$\boldsymbol{y}_t = \boldsymbol{A}_t\boldsymbol{x}_t + \boldsymbol{n} \tag{4.16}$$

vwhere $\boldsymbol{P} = \boldsymbol{I}$ is the random walk state transition matrix, which describes the relationship between consecutive frames [35]. For the estimation of temperature field is to minimise the following cost function:

$$x_t = \min_X \left\| \boldsymbol{y}_t - \boldsymbol{A}_t\boldsymbol{x}_t \right\|^2_{\Gamma_t^n} + \left\| \boldsymbol{x}_t - \boldsymbol{P}\boldsymbol{x}_{t-1} \right\|^2_{C_{t+1|t}} \tag{4.17}$$

where the measurement noise $_n$ is considered as a Gaussian white noise, so its covariance matrix is set as $\boldsymbol{\Gamma}_t^n = diag(\sigma_n)$, and $_{\sigma_n}$ is a predefined parameter. The prediction error w_t is considered as a Gaussian white noise too, so its covariance matrix is set as $\boldsymbol{\Gamma}_t^w = diag(\sigma_w)$ and $_{\sigma_w}$ is another predefined parameter. $\boldsymbol{C}_{t+1|t}$ is the time update covariance matrix, which is updated for each frame. The reconstruction for each frame is completed in two steps.

Step 1: Update in measurement

$$\boldsymbol{K}_t = \boldsymbol{C}_{t|t-1}\boldsymbol{A}_t^T(\boldsymbol{A}_t\boldsymbol{C}_{t|t-1}\boldsymbol{A}_t^T + \boldsymbol{\Gamma}_t)^{-1} \tag{4.18}$$

$$\boldsymbol{C}_{t|t} = [\boldsymbol{I} - \boldsymbol{K}_t\boldsymbol{A}_t]\boldsymbol{C}_{t|t-1} \tag{4.19}$$

$$\boldsymbol{x}_t = \boldsymbol{x}_{t|t-1} + \boldsymbol{K}_t(\boldsymbol{y}_t - \boldsymbol{A}_t\boldsymbol{x}_{t|t-1}) \tag{4.20}$$

Step 2: Update in prediction

$$\boldsymbol{C}_{t+1|t} = \boldsymbol{P}\boldsymbol{C}_{t|t}\boldsymbol{P}^T + \boldsymbol{\Gamma}_t^w \tag{4.21}$$

$$\boldsymbol{x}_{t+1|t} = \boldsymbol{P}\boldsymbol{x}_t \tag{4.22}$$

For the initial guess of the reconstruction, $\boldsymbol{x}_{1|0} = \boldsymbol{0}$ and $\boldsymbol{C}_{1|0} = \boldsymbol{0}$.

Compared to the algebraic time-resolved reconstruction, it also uses a temporal smoothing regularisation. The difference is that (1) only adjacent

frames are used to calculate the temporal regularisation; and (2) the temporal regularisation is weighted by the state transfer error covariance.

However, the Kalman filter reconstruction has a slow convergence, that the reconstruction error of a few frames in the beginning is relatively large. In comparison, the new method has the flexibility to modify the reconstruction process of the first segments to be iterative, which will significantly improve the reconstruction error at the beginning.

4.4 Results and discussion

4.4.1 Numerical simulation

In this section, the performance of the proposed method is evaluated with a series of numerical simulations. The sensor array setup is illustrated in Figure 3-2. The data collection is based on the semi-parallel scheme described in section 3.2. In this simulation, the temperature field changes are assumed to take place during each 120 ms repetition period and 36 TOFs from 3 transmitters are used for the reconstruction of each frame. As a result, the measuring time per frame is reduced to 120 ms. The proposed method is compared with the Kalman filter reconstruction. Although optimal parameters can be used to improve the reconstruction quality, all the tomographic reconstruction results in this section are obtained using the same parameters. These empirical reconstruction parameters are given in Table 4-2. The 1x1 m sensing area is segmented into 400 pixels in the image reconstruction process and the dimension of each pixel is 5x5 cm, as shown in Figure 3-2.

Table 4-2: Reconstruction parameters used in simulation

Parameter	Method	Value
N	OTRR/Kalman	400
M	OTRR/Kalman	36
α_1	OTRR/Kalman	0.01
α_2	OTRR	0.1
T	OTRR	16
IterNo	OTRR	200
ϵ	OTRR	1e-10
σ_1	Kalman	1e-12
σ_2	Kalman	1e-13

Three representative dynamic phantoms of the temperature field are simulated to evaluate the reconstruction performance, including the temperature field of a point heat source with periodic rapid temperature change, diffusive expanding shape change and rotational position change. There are 200 frames in total to be reconstructed, and the repetition period of the dynamic changes is 32 frames (3840 ms). The first 16 frames of the three simulated phantoms are shown in Figure 4-5.

To quantitatively evaluate the overall reconstruction quality using the two methods, image relative error (IE) is adopted. Besides the relative image error for tomographic reconstruction, another three metrics are used to evaluate the accuracy of the reconstructed temperature field.

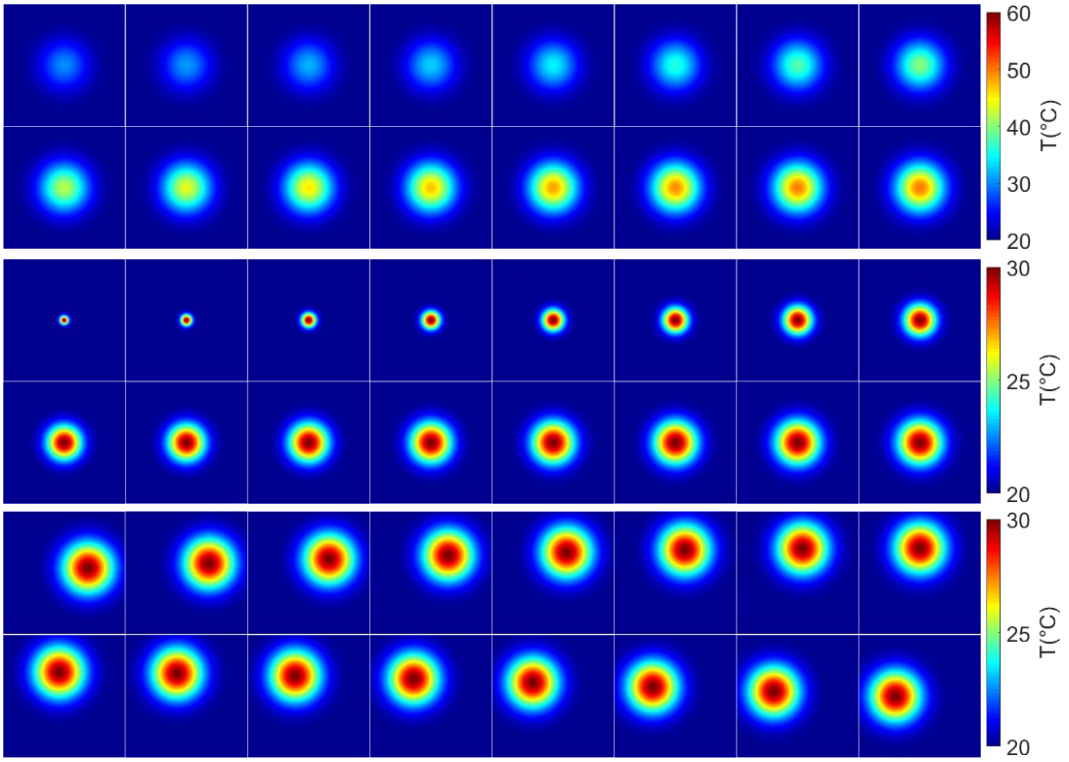

Figure 4-5: The three temperature phantoms of heating process of temperature field (top) heat source expanding (mid) and heat source rotation (bottom)

Dislocation (DL) evaluates the ratio of the distance between the heat source centre of the reconstructed and original temperature phantoms to the size of the sensing area. DL evaluates the performance of the time resolved reconstruction method on localising the centre of the heat source. As small DL shows that the reconstruction method has the ability to resolve the motion of the heat source.

Peak value (PV) evaluates the relative error of the reconstructed peak value of the temperature field to the original phantom. PV measures the quantitative accuracy of the temperature field reconstruction. As small PV shows that the reconstruction method can resolve the dynamic temperature changes.

Widening (WD) evaluates the ratio of the reconstructed heated area to the original heated area. The average temperature is used as a threshold to extract the heated area from the temperature field images. WD measures the

consistency of sizes of the estimated and target heated area. A high WD shows that the reconstruction method can resolve the dynamic heat source diffusion and expanding changes. Ideally, DL, PV and IE should be close to 0 but WD should be close to 1.

In this simulation, the measurement SNR is set to be 35 dB, which is close to the measurement noise level of the lab-scale acoustic tomography system. The mean values of the 4 quantitative metrics are presented in Table 4-3. The convergence performance with respect to the image error is shown in Figure 4-6. The evolution of all the four metrics with respect to different measurement noise level is plotted in Figure 4-7. The reconstructed images of the first 16 frames are shown in Figure 4-8 and Figure 4-9.

Firstly, for reconstruction image error of all three phantoms, the proposed OTRR method has much better performance compared to the Kalman filter method. Notably, both methods have smaller reconstruction IE for phantom 2 than the other two phantoms. The reason is that the dynamic changes of the expanding phantom here are much smaller than the other two phantoms, and the temporal redundancy of this phantom 2 was utilised by the two time-resolved methods for a better reconstruction accuracy.

Secondly, for the DL metric, the proposed OTRR method outperforms the Kalman filter method as well. Especially for phantom 3, where the dynamic change is mainly the rotation of the heat source. The OTRR method can accurately locate the dynamic heat centre with 4.57% location error. In comparison, the DL of Kalman filter method is 13.72%.

Thirdly, for the PV metrics, both methods lack the accuracy to provide quantitative reconstruction of the dynamic temperature change of the heat centre. Although the OTRR has a slightly better performance for phantom 3, where the peak value of temperature doesn’t change over time, its PV for the other two phantoms are larger than 8%. The possible reason for this PV inaccuracy is due to the over-smoothing on the temporal domain. Temporal

regularisation helps to reconstruct the temperature field images with fewer TOFs, but it also results in bias error in the reconstruction.

Table 4-3: The quantitative reconstruction metrics

		Phantom1	**Phantom2**	**Phantom3**
IE (%)	Kalman	7.3	4.34	7.67
	OTRR	4.25	2.99	4.21
DL (%)	Kalman	3.75	3.99	13.72
	OTRR	1.46	1.05	4.57
PV (%)	Kalman	12.79	11.65	15.93
	OTRR	8.82	8.86	5.92
WD (%)	Kalman	1.17	0.74	0.89
	OTRR	1.14	0.95	1.08

For the shape metric WD, the OTRR method also has better performance, especially for the reconstruction result of phantom 2, where the dynamic characteristics of the temperature are mainly about the expanding shape change. The WD of the OTRR method is 0.95, compared to the 0.74 of the Kalman filter method.

Figure 4-6 shows the convergence performance comparison of the two methods. Obviously, the OTRR method has a faster convergence compared to the Kalman filter method. This is because only the first segment is reconstructed iteratively using the OTRR method. As a result, it can converge much faster than the Kalman filter method. The averaged computational time for the OTRR method is 6.51 s, including 4.15 s used for the iterative computation of the first segment reconstruction, and 2.36 s for the reconstruction of the rest frames. The computation time for Kalman is 0.57 s for all 200 frames. Clearly the Kalman filter method has much lower computational time compared to the OTRR method. But consider that the time

duration of the 200 frames is 24 s, the 6.51 s computational time of the OTRR method is acceptable, even for the online monitoring system.

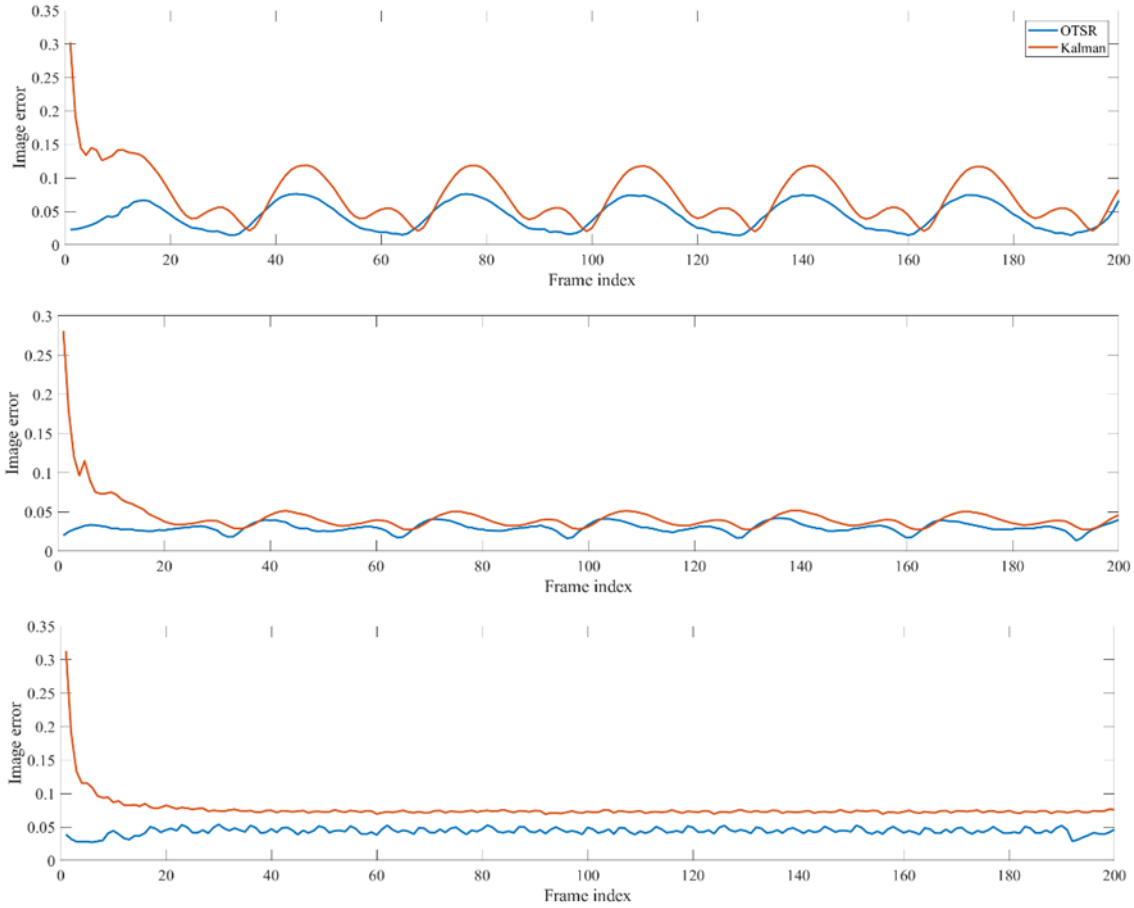

Figure 4-6: The reconstruction image errors of each frame for phantom 1 (top) phantom 2 (mid) and phantom 3 (bottom)

To evaluate the noise tolerance of the two methods, measurements at different noise level are used in the simulation. The averaged metrics under different SNR conditions are plotted in Figure 4-7. From the figure, it can be concluded the proposed OTRR method has a better noise tolerance than the Kalman filter method in terms of IE, DL and PV. For the shape metric WD, both methods have a good performance when the SNR is larger than 30 dB.

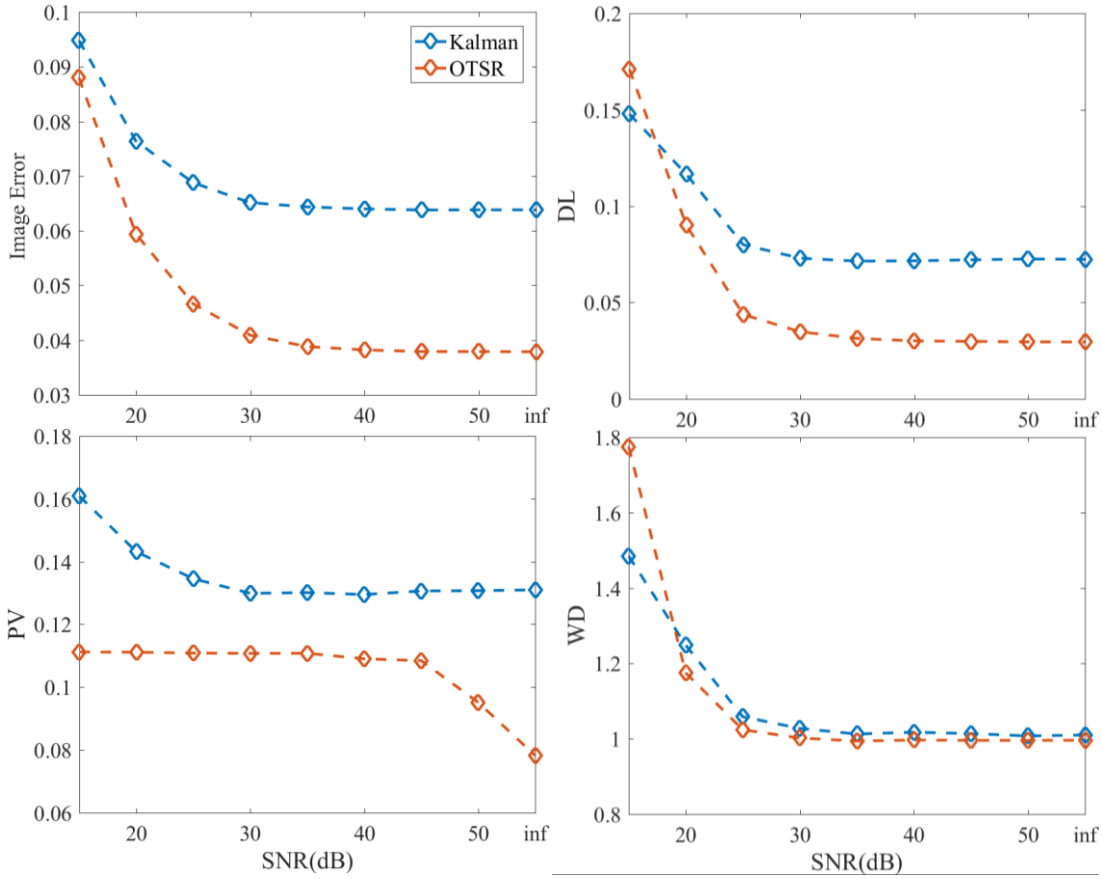

Figure 4-7: Quantitative metrics at different noise level

Figure 4-8 and Figure 4-9 show the reconstruction images of the first 16 frames. The proposed OTRR method has much better performance compared to the Kalman filter method. As can be seen from the figures, the Kalman filter method has a large reconstruction error in the first few frames. The artefacts are reduced in the following frames, but the dynamic characteristic details are poorly preserved, especially for the phantom 3. From the reconstructed images, it is very difficult to accurately locate the heat centre, estimate the peak value and track the shape changes of the temperature field. Compared to the Kalman filter method, the OTRR method can resolve the dynamic changes for all three phantoms. The temperature peak value increase, the heated area expansion, and the rotational location change of the heat centre are clearly described in the reconstructed images.

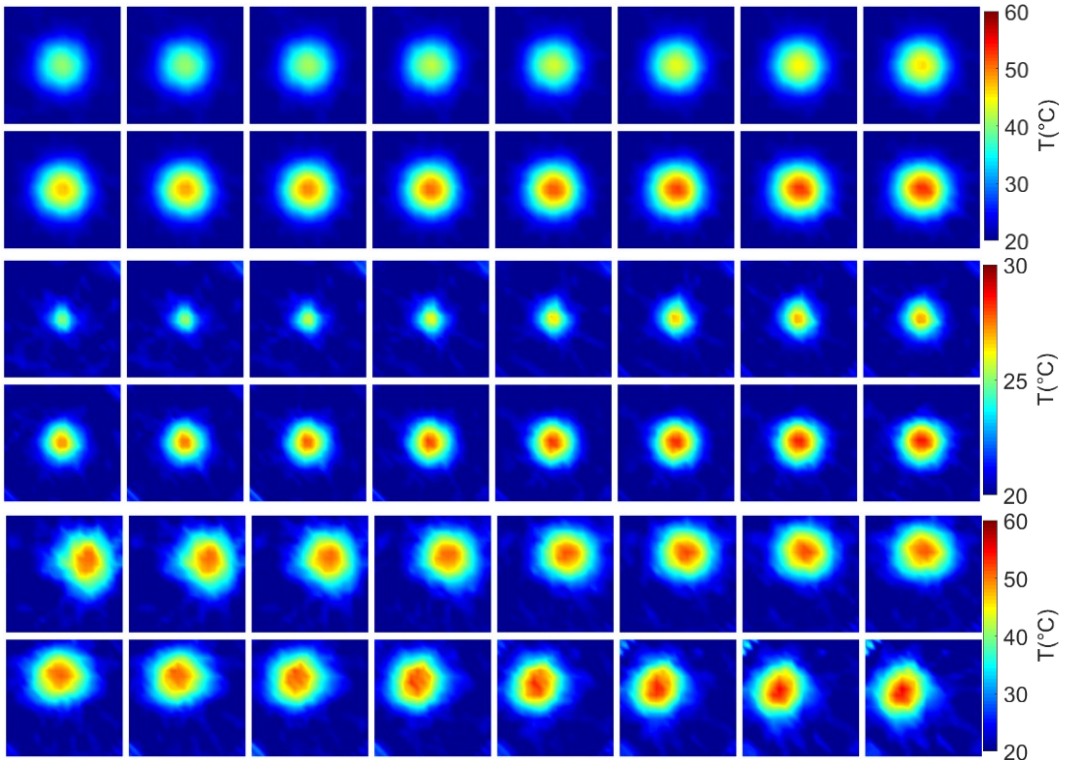

Figure 4-8: Reconstruction of the first 16 frames using OTRR method

In conclusion, the simulation results show that the proposed OTRR method has better reconstruction accuracy, better noise tolerance, and a faster convergence rate than the Kalman filter method. Although the OTRR method has a longer computational time, 6.51 s for 200 frames compared to the 0.57 s of Kalman filter method. This computational time of OTRR is still fast enough for the online monitoring requirement. The OTRR achieved an improvement in temporal resolution. Compared to the fully sampled reconstruction, the measuring time per frame is reduced from 640 ms to 120 ms.

4.4.2 Experimental results

The performance of OTRR is further validated through real data experiments. A hair dryer was placed 5 cm above the sensing plane to blow hot air downwards into the sensing area and create a hotspot. The acoustic tomography system was then used to reconstruct the temperature field. During the experiment, the hair dryer was placed in 7 different positions. For each

position, after the hair dryer was switched on and the temperature had stabilised, several measurements (20 frames) were taken to test the repeatability of the temperature field reconstruction and record all the 192 TOFs. Similar to the numerical simulations, the change in position took place during each 120 ms period. 36 TOFs from 3 transmitters were used for the reconstruction of the under-sampled frame. The fully sampled tomographic images using all the 192 TOFs will be reconstructed based on the conventional SIRT method.

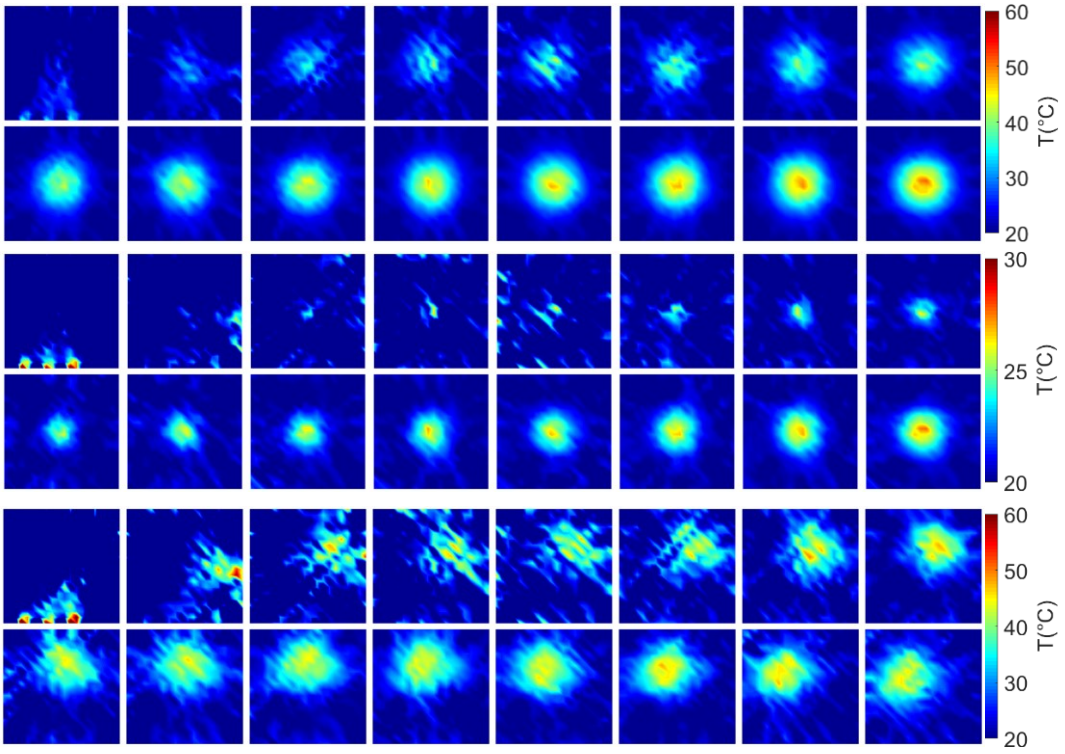

Figure 4-9: Reconstruction of the first 16 frames using Kalman filter method

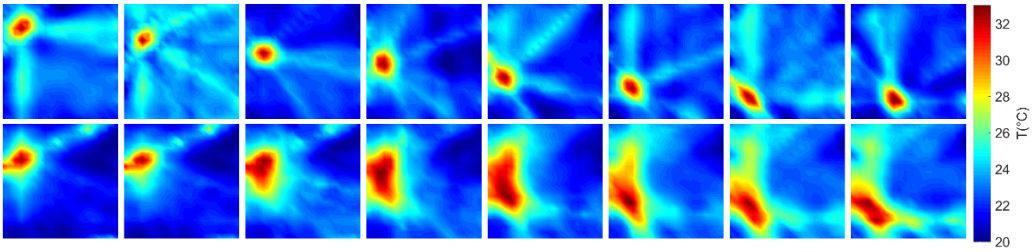

Figure 4-10: Fully sampled reconstruction results (first row) and the under-sampled reconstruction using OTRR (second row)

The comparison between the fully sampled tomographic reconstructions and the under-sampled reconstructions are presented in Figure 4-10. The comparison indicates that the under-sample images using OTRR method is able to resolve the position change of the hot spot, but the reconstructed image has large distortion compared to the fully sampled images. Using the fully sampled reconstruction results as the ground truth, then the quantitative reconstruction metrics, the IE, PV, DL and WD can be calculated, which are shown in Table 4-4. From the table it is clear that the reconstruction accuracy in terms of PV is very close to the fully-sampled reconstruction, which is 0.96%. However, the averaged WD is relatively large (1.54), which shows that the OTRR method do not have the accuracy to reconstruct the shape of the heated area. The averaged IE and DL are 2.39% and 3.16% respectively, which is acceptable considering the temporal resolution improvement compromises the loss of spatial resolution.

Table 4-4: The averaged quantitative reconstruction metrics of the experiment results.

IE (%)	PV (%)	DL (%)	WD
2.39	0.96	3.16	1.54

A thermocouple was placed 5 cm beneath the sensing plane and at the centre of the heated air stream to validate the temperature reconstruction accuracy. The relative mean square error is 16.92% (with respect to Celsius) or 1.91% (with respect to Kelvin degree) at the centre of the reconstructed hotspot using 36 TOF measurements and the OTRR method. On the other hand, the relative mean square error is much smaller using 192 TOFs and SIRT method, which is 5.12% (with respect to Celsius) or 0.58% (with respect to Kelvin degree).

4.5 Summary

In this chapter, an online time-resolved reconstruction (OTRR) method is developed for real-time monitoring system. OTRR uses a reduced number of

TOFs for reconstruction of each frame. As a result, the measuring time per frame is reduced from 640 ms to 120 ms. Numerical simulations and experiments show the OTRR method provides satisfactory results in tracking the dynamic changes of the temperature field. Compared to the existing dynamic reconstruction method, such as Kalman filter reconstruction, OTRR has a higher quantitative accuracy, faster convergence rate and better noise robustness.

Chapter 5 Nonlinear temperature field reconstruction based on bent ray model

5.1 Introduction

As illustrated in section 2.2 of Chapter 2, geometric acoustic theory is used in the forward problem of the acoustic tomography. According to the geometric acoustic theory, the sound waves are considered to propagate along ray paths between transducer pairs. Provided the sound propagation ray paths and the corresponding TOF measurements are made along these ray paths, the temperature field can be reconstructed.

The difficulty of the tomographic reconstruction is the dependency of the ray path on the unknown distribution of the temperature field. For simplicity, in some applications when the acoustic tomographic system is used in near surface atmosphere [1, 17-19, 54], acoustic propagations between the transducer pairs are approximated as straight paths. However, in some situations, like the combustion process in furnace environment[23, 24], the gradient of the temperature field can be relatively large, and the sound speed distribution is highly heterogeneous. The corresponding ray path will be curved around the heated area due to the refraction effect, and the commonly used straight ray model may cause large reconstruction error.

This chapter focuses on reducing the reconstruction inaccuracy of using a straight ray model under the large gradient temperature field. Instead of using the straight ray model and linear reconstruction, the bent ray model and nonlinear reconstruction algorithm are applied, which allows the sound propagation ray paths and temperature distribution to be reconstructed iteratively from the TOFs. The reconstruction process consists of two parts: (1) the nonlinear conjugate gradient descent method to efficiently update the solution of the temperature field; and (2) the Fast Marching Method (FMM) to determine the corresponding ray paths given the temperature field estimation.

Numerical simulations have been carried out to validate the performance of the proposed method.

5.2 Modelling error due to refraction effect

The conventional acoustic tomographic reconstruction assumes that the ray path is known *a priori*. For example, the acoustic tomography system for near surface atmosphere imaging assumes that the ray paths are straight lines between transducers. For the ocean tomography, the ray paths are pre-calculated based on the ocean characteristics [2, 3].

However, for some furnace environments, the gradient of temperature distribution can be considerably large. As a result, the propagation ray path between transmitters and receivers will be curved due to the refraction effect. An example of the temperature field with a large gradient is simulated and its corresponding ray paths is shown in Figure 5-1.

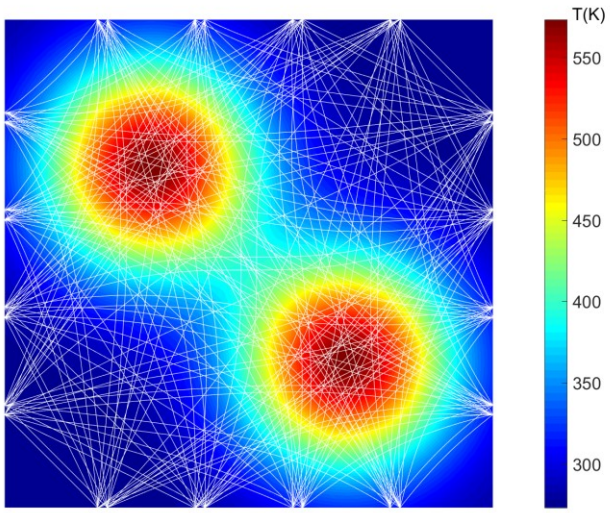

Figure 5-1: The temperature field and the corresponding ray paths

Next, the example in Figure 5-1 can be used to quantitatively illustrate the inaccuracy due to the refraction effect. $\boldsymbol{s_\lambda}$ and $\tilde{\boldsymbol{s}}_{\boldsymbol{\lambda}}$ represent the reconstructed temperature field using the bent ray model and the straight ray model

respectively. The modelling error of reconstruction is due to the refraction effect, more precisely the relative mean square error $\frac{\|\tilde{s}_\lambda - s_\lambda\|_2}{\|s_\lambda\|_2}$ between $\tilde{s}_\lambda$ and s_λ shows how sensitive the solution is to the modelling error. For simplicity, the measurement noise is ignored. The reconstruction comparison of $\tilde{s}_\lambda$ and s_λ is shown in Figure 5-2 below:

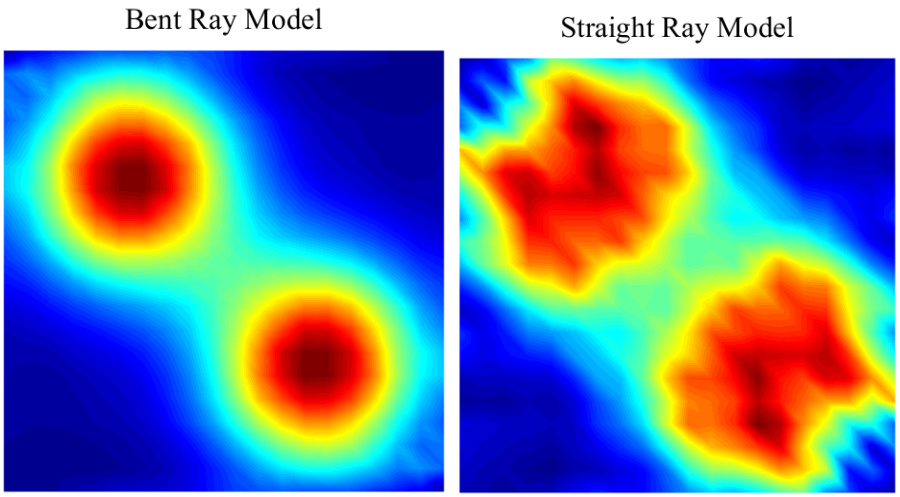

Figure 5-2: The reconstructed temperature field using the bent ray model (s_λ) and the straight ray model ($\tilde{s}_\lambda$), the image errors are 2.73% and 12.74% respectively. The regularisation parameter $\lambda = 0.1$ and the noise level is set to be 45 dB

The reconstructed image results in Figure 5-1 demonstrate the significant increase of image error, from 2.73% of using the bent ray model to 12.74% using the straight ray model. Besides, the reconstructed image using the inaccurate straight ray model results in large distortion in the image space. Compared to the reconstructed image using the bent ray model, the shape and the heat centre position of the temperature field are not correctly reconstructed when the straight ray model is applied. It can be concluded that the modelling error of using the straight ray model when the temperature field has a large gradient will lead to a large quantitative image error and distortion. Instead of the inaccurate straight ray model, the bent ray model should be used in the reconstruction.

5.3 Nonlinear reconstruction

5.3.1 Problem statement

The use of straight ray model will affect the accuracy of the tomographic reconstruction. Instead, the bent ray model is applied here. In this case, the ray paths are unknown but the dependence between the paths and the unknown fields is acknowledged based on geo-acoustic theory. The forward problem of acoustic tomography is defined in equation(2.6), and the reconstruction process is to find the optimal slowness distribution $\boldsymbol{s}$ which agrees with the TOF measurement through the nonlinear forward problem equation.

For the tomographic reconstruction, the regularised least square solution is commonly used. The inverse problem is solved by minimising the objective function as is defined in equation(2.19).

5.3.2 Nonlinear conjugate gradient descent

The nonlinear conjugate gradient descent (NCGD) is an effective tool for solving the nonlinear inverse problem. It uses the gradient of the cost function alone to iteratively search for the local minimal value of the cost function. In each iteration, the slowness distribution $\boldsymbol{s}$ is updated along the conjugate direction with a line searched step size.

Generally, the nonlinear conjugate gradient descent solves the tomographic reconstruction problem in the form:

$$\boldsymbol{s}_{k+1} = \boldsymbol{s}_k + \lambda_k \boldsymbol{d}_k \tag{5.1}$$

Every time, the search will continue along this conjugate direction until a line minimum is found.

Here $\boldsymbol{d}_k$ is the conjugate search direction to minimise the cost function and λ_k is the appropriate step size to reach the line minimum along this direction.

To initialise the searching direction, the negative gradient of the cost function is used, which is the same as the Gauss-Newton method. Then all the searching directions $\boldsymbol{d}_k$ are constructed to be conjugate to previous directions. As a result, the minimisation in this iteration will preserve previous work. This gives the following expression:

$$d_k = \begin{cases} -\nabla \boldsymbol{C}(\boldsymbol{s}_k), & \text{for } k = 1 \\ -\nabla \boldsymbol{C}(\boldsymbol{s}_k) + \beta_k \boldsymbol{d}_{k-1}, & \text{for } k \geq 2 \end{cases} \tag{5.2}$$

The calculation of the gradient is the key step when the conjugate searching direction is determined. The gradient is given by:

$$\begin{aligned} \nabla \boldsymbol{C}(\boldsymbol{s}_k) &= 2\frac{\partial \boldsymbol{r}(\boldsymbol{s}_k)}{\partial \boldsymbol{s}_k}\boldsymbol{r}(\boldsymbol{s}_k) + 2\alpha \boldsymbol{Q}^T \boldsymbol{Q}\boldsymbol{s}_k \\ &= 2\boldsymbol{J}_r(\boldsymbol{s}_k)\boldsymbol{r}(\boldsymbol{s}_k) + 2\alpha \boldsymbol{Q}^T \boldsymbol{Q}\boldsymbol{s}_k \end{aligned} \tag{5.3}$$

where $\boldsymbol{J_r}(\boldsymbol{s_k}) = \frac{\boldsymbol{\partial r}(\boldsymbol{s_k})}{\boldsymbol{\partial s_k}}$ is the Jacobian matrix and $\boldsymbol{r}(\boldsymbol{s_k}) = \boldsymbol{\tau} - \boldsymbol{A}(\boldsymbol{s_k})\boldsymbol{s_k}$ is the residual term[29].

Recall the forward modelling equation in (2.5), the relationship between TOF and sound speed slowness is defined as:

$$\tau_i(\boldsymbol{s}) = \int_{\Gamma_i(\boldsymbol{s})} s(x,y)dl \tag{5.4}$$

where $\Gamma_i(\boldsymbol{s})$ is the i-th ray path according to the slowness distribution $\boldsymbol{s}$ and $\tau_i(\boldsymbol{s})$ is the TOFs for given slowness distribution along this ray path.

Based on the Fermat's principle, the travel time is stationary along the actual ray path [101].

Let $\boldsymbol{s} = \boldsymbol{s_0} + \boldsymbol{\Delta s}$,

$$\int_{\Gamma_i(\boldsymbol{s}_0+\Delta \boldsymbol{s})} s_0(x,y) + \Delta s(x,y)\, dl = o(\|\Delta \boldsymbol{s}\|_2^2) + \int_{\Gamma_i(\boldsymbol{s}_0)} s_0(x,y) + \Delta s(x,y)\, dl \tag{5.5}$$

Therefore, equation (2.5) can be rewritten as

$$\begin{aligned}\tau_i(\boldsymbol{s}) &\approx \int_{\Gamma_i(s_0)} s_0(x,y)+\Delta s(x,y)\,dl \\ &= \tau_i(\boldsymbol{s}_0)+\boldsymbol{a}_i(\boldsymbol{s}_0)\Delta\boldsymbol{s}\end{aligned} \tag{5.6}$$

where $\boldsymbol{a_i}$ is the i-th row of the ray length matrix.

Therefore, the Jacobian matrix $\boldsymbol{J_r}(\boldsymbol{s_k})$ around current solution is approximated using the corresponding ray length matrix $\boldsymbol{A}_k$,

$$\boldsymbol{J}_r(\boldsymbol{s}_k)=\frac{\partial \boldsymbol{r}(\boldsymbol{s}_k)}{\partial \boldsymbol{s}_k}=\frac{\tau_i(\boldsymbol{s}_k+\Delta\boldsymbol{s})}{\Delta\boldsymbol{s}}=\boldsymbol{A}_k \tag{5.7}$$

Therefore, the gradient is given by:

$$\nabla \boldsymbol{C}(\boldsymbol{s}_k)=2\boldsymbol{A}_k\boldsymbol{r}(\boldsymbol{s}_k)+2\alpha\boldsymbol{Q}^T\boldsymbol{Q}\boldsymbol{s}_k \tag{5.8}$$

The ray length matrix is obtained by conducting the ray tracing given the slowness distribution $\boldsymbol{s_k}$. Details will be presented in section 5.3.3.

To ensure the directions $\boldsymbol{d}_k$ are conjugate to all previous directions, the conjugate gradient parameter β^k, based on Polak–Ribière method, is used here[102].

$$\beta_k=\frac{\boldsymbol{g}_k^T\left(\boldsymbol{g}_k-\boldsymbol{g}_{k-1}\right)}{\boldsymbol{g}_{k\text{-}1}^T\boldsymbol{g}_k} \tag{5.9}$$

The step size λ_k is obtained by the line search, and details will be presented in section 5.3.4.

$$\lambda_k=\min_{\lambda_k}\boldsymbol{C}(\boldsymbol{s}_k+\lambda_k\boldsymbol{d}_k) \tag{5.10}$$

The details of implementing the NCGD method to solve the inverse problem is illustrated in Table 5-1.

Table 5-1: The nonlinear conjugate gradient descent (NCGD) reconstruction method

Algorithm 5-1: the nonlinear conjugate gradient descent method

Initialise: $\boldsymbol{s_0} = \mathbf{0}$, $\epsilon = 10^{-6}$, $\mathrm{k} = 0$, n=1.4, R=287

Iteration

Step 1: Do ray tracing based on the current slowness estimation $\boldsymbol{s}_k$ calculate the ray length matrix $\boldsymbol{A_k}$

Step 2: Calculate the gradient $\boldsymbol{\nabla C(s_k)}$ with $\boldsymbol{A_k}$

Step 3: Calculate the conjugate gradient parameter β^k and conjugate direction $\boldsymbol{d}_k$

Step 4: Do line search and find the appropriate step size λ_k

Step 5: Update the solution $\boldsymbol{s}_{k+1} = \boldsymbol{s}_k + \lambda_k \boldsymbol{d}_k$

Until the stopping criterion is satisfied

$$\frac{\|\boldsymbol{s}_{k+1} - \boldsymbol{s}_k\|_2}{\|\boldsymbol{s}_k\|_2} \leq \epsilon$$

Output the reconstructed temperature field

$$\boldsymbol{T} = \frac{1}{nR\boldsymbol{s}^2}$$

5.3.3 Ray tracing

Given the sound speed distribution, the ray path of the sound propagation should be firstly determined using the ray tracing method. Then, the ray length matrix $\boldsymbol{A_k}$ can be updated in each iteration for calculating the gradient $\boldsymbol{g}_k$. The sound propagation between transmitter and receiver is governed by the wave equation:

$$\nabla^2 \boldsymbol{\Phi} = \frac{1}{c^2} \frac{\partial^2 \boldsymbol{\Phi}}{\partial t^2} \tag{5.11}$$

where Φ is the wave scalar potential and c is the sound speed.

The harmonic solution to equation (5.11), assume $\Phi = \mathrm{A}(\boldsymbol{r})\mathrm{e}^{-\mathrm{i}\omega\mathrm{t}}$, leads to the Helmholtz equation.

$$\nabla^2 \boldsymbol{A} + k\boldsymbol{A} = 0 \tag{5.12}$$

where $k = 2\pi/\lambda$ is the wave number.

Focusing on the sound propagation ray path, where the amplitude solution $\mathrm{A}(\boldsymbol{r})$ is defined as

$$A(\boldsymbol{r}) = F(\boldsymbol{r})e^{-iP(\boldsymbol{r})} \tag{5.13}$$

where $F(\boldsymbol{r})$ and $P(\boldsymbol{r})$ are the amplitude and phase functions. Substitute equation (5.13) into equation (5.12), and ignore the imaginary part,

$$\frac{\nabla^2 F}{F} - \left(\nabla P(\boldsymbol{r})\right)^2 + k^2 = 0 \tag{5.14}$$

The high frequency assumption of the geometric ray theory indicates that $k^2 \gg \frac{\nabla^2 F}{F}$, which basically assumes that the sound speed is approximately constant over one wavelength. Therefore, equation (5.14) becomes the Eikonal equation

$$\left(\nabla P(\boldsymbol{r})\right)^2 = k^2 \tag{5.15}$$

The wave front is defined as the surface with constant phase and the sound propagation ray paths are perpendicular to the wave front.

Using the notation $P(\boldsymbol{r}) = \omega T(\boldsymbol{r})$, equation (5.15) becomes

$$\left|\nabla T(\boldsymbol{r})\right| = \frac{1}{\boldsymbol{c}(\boldsymbol{r})} \tag{5.16}$$

where $T(\boldsymbol{r})$ denotes the arrival time of the wave front, which is the TOF from the source to the current position $\boldsymbol{r}$. Given the sound speed distribution and

the transmitter source position, TOF map is calculated by solving the equation (5.16). Based on the TOF map, the ray path can be determined.

Several methods have been developed to solve the Eikonal equation (5.15). One of the most robust and computational efficient methods among those techniques is the fast marching method (FMM). Based on FMM, the discrete approximation of equation (5.16) is:

$$\max(\nabla_x^+ T_{m,n}, \nabla_x^- T_{m,n}, 0)^2 + \max(\nabla_y^+ T_{m,n}, \nabla_y^- T_{m,n}, 0)^2 = \frac{1}{c_{m,n}^2} \qquad (5.17)$$

where ∇_x^+ and ∇_x^- denote the discrete forward and backward differentials along the x direction, and so do the ∇_y^+ and ∇_y^-. $\boldsymbol{c}_{m,n}^2$ is the discrete sound speed and (m, n) denotes the coordinates.

The FMM ray tracing accuracy also depends on the meshing size of sound speed distribution. The reconstructed distribution mesh grids, with the use of 192 TOFs for given transducer setup, will not be more than 40 by 40. Therefore, interpolation and up-sampling of the sound speed distribution is necessary before the ray tracing process. Here the RBF basis is used for interpolation with a factor of 10.

The FMM method divides all the pixels into three categories: (1), the ‘known’ pixels, the TOF at this pixel determined and will not be changed later; (2), the ‘narrow band’ pixels, the TOF may be changed later; and (3), the ‘far’ pixel, the TOF is not yet computed.

Generally, given the sound speed distribution and the position of the transmitter and receiver, the FMM method is illustrated in Table 5-2.

Table 5-2: The fast marching method (FMM) for ray tracing

Initial with the source point (transmitter), mark it as the 'known' with $t = 0$
Iteration: Step 1: Mark the nearest neighbours of the 'known' to 'narrowband' Step 2: Calculate the arrival time t of the pixels in the 'narrowband' with equation (5.17) Step 3: Extract the pixel in the 'narrowband' with minimum arrival time, mark it as the 'known' Until the all the receivers' pixels are marked as 'known'
Compute the ray path using the Runge-Kutta gradient descent method on the arrival time field
Output the ray path

Usually the FMM approximates the gradient using the first order differential scheme. As a result, the FMM is not accurate along diagonal directions, and its computational complexity is not optimal. Therefore, the Multistencils Fast Marching (MSFM) is used to improve the accuracy. The main difference compared to the FMM is the way in which the discrete differentials are approximated. More details are described in [103].

Based on the MSFM, the ray paths from one transmitter to all the other receivers according to the current sound speed distribution can be determined, and an example is shown in Figure 5-3.

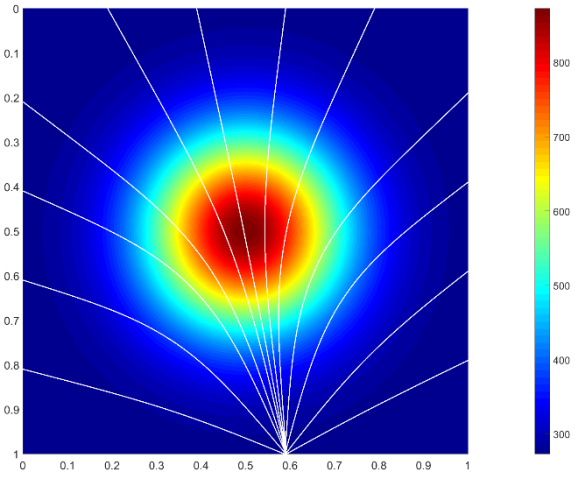

Figure 5-3: Ray paths from transmitter (0.6, 0) to all the other 12 receivers

5.3.4 Line search for optimal step size

During each iteration, the step size λ_k is obtained by solving a one dimensional minimisation problem, which is also known as the 'line search in scalar form to search along the conjugate gradient direction $\boldsymbol{d}_k$ for the best $\boldsymbol{s}_{k+1}$. The common line search method can be categorised into two main groups, the inexact line search and the exact line search. The exact line search is to find the optimal step size to minimise the cost function along $\boldsymbol{d}_k$, which is defined as follows:

$$\lambda_k = \min_{\lambda_k} \boldsymbol{C}(\boldsymbol{s}_k + \lambda_k \boldsymbol{d}_k) \tag{5.18}$$

However, the exact line search to find the optimal step size is computational demanding. Instead, the inexact line search is preferred. During each step it is only necessary to approximately minimise the cost function along $\boldsymbol{d}_k$, or reduce the cost function sufficiently [104]. In particular, one simple and efficient line search procedure is the backtracking line search based on the Armijo's rule, which is expressed in Table 5-3. Here the subscript *t* denotes the iteration index of the line search algorithm.

Table 5-3: The backtracking line search method based on Armijo-Goldstein's rule

Initialization: $0 < \alpha < 0.5, 0 < \beta < 1$, $\lambda_{k,0} = -\boldsymbol{g}_k^T \boldsymbol{d}_k / \|\boldsymbol{d}_k\|_2^2$

Repeat $\lambda_{k,t} = \beta \lambda_{k,t-1}$

Until the stopping condition:

$$\boldsymbol{C}(\boldsymbol{s}_k) - \boldsymbol{C}\left(\boldsymbol{s}_k + \lambda_{k,t}\boldsymbol{d}_k\right) \geq \alpha \lambda_{k,t} \boldsymbol{g}_k^T \boldsymbol{d}_k$$

Output the step size $\lambda_{k,t}$

The use of Armijo's inequality requires to guarantee that

$$\boldsymbol{C}(\boldsymbol{s}_k + \lambda_{k,t}\boldsymbol{d}_k) < \boldsymbol{C}(\boldsymbol{s}_k) \tag{5.19}$$

For this reason, the algorithm is always a descent algorithm. Besides, it should be noted that an increased number of line search iterations helps to improve the line search accuracy, but at the same time it will also increase the computational cost to evaluate the cost function values (using the ray tracing method). There should be a balance between these two factors. And this balance can be obtained with appropriate selection of the two control parameters α and β. Typically, it takes $\gamma \in [.5, .8]$ while $c \in [.001, .1]$ with adjustments depending on the cost of function evaluation and degree of nonlinearity.

5.4 Connection with previous works

To solve the nonlinear inverse problem, another simple way is to use the nonlinear gradient descent (NGD) method. The reconstruction is based on the local linearity assumption to simplify the nonlinear inverse problem, which assumes that the small changes for the residual term are approximately linear.

$$\boldsymbol{r}(\boldsymbol{s}_k + 1) = \boldsymbol{r}(\boldsymbol{s}_k) + \boldsymbol{A}_k(\boldsymbol{s}_{k+1} - \boldsymbol{s}_k) = \boldsymbol{A}_k \boldsymbol{s}_{k+1} - \boldsymbol{\tau} \tag{5.20}$$

During each iteration, the solution is given as:

$$\boldsymbol{s}_{k+1} = \min_{s} \|\boldsymbol{\tau} - \boldsymbol{A}_k \boldsymbol{s}\|_2^2 + \|\boldsymbol{Q}\boldsymbol{s}\|_2^2 \tag{5.21}$$

Therefore, with the use of local linear assumption, the update of $\boldsymbol{s}_{k+1}$ requires only the ray length matrix $\boldsymbol{A_k}$, which only depends on previous solution $\boldsymbol{s}_k$, and can be calculated using the aforementioned FMM based ray tracing method. Then the reconstruction becomes a linear inverse problem as shown in equation (5.21), which can be solved by the GSVD or SIRT method.

Generally, the nonlinear tomographic reconstruction is illustrated in Table 5-4.

Compared to the NCGD method, the NGD method is quite simple and easy to understand. However, it has two drawbacks: (1) the reconstruction performance will be largely affected due to the complexity of the medium since the local linearity assumption is not valid when large perturbation of the ray length matrix occurs.; and (2) without the conjugate gradient direction and line search step size, the NGD method requires a much higher computational cost for more iterations, and its convergence performance is not guaranteed.

Table 5-4: The NGD method to solve the nonlinear inverse problem

Initiation: A^0 is calculated based on the straight ray model, tolerance ε
Iteration: Step 1: linear reconstruction; calculate $\boldsymbol{s^{k+1}}$ by solving equation (5.21) given $\boldsymbol{A^k}$. Step 2: ray tracing; calculate the ray length matrix $\boldsymbol{A^{k+1}}$ given the slowness estimation $\boldsymbol{s^{k+1}}$.
Until the stopping criterion is satisfied: $\left\|\boldsymbol{\tau} - \boldsymbol{A^{k+1}s^{k+1}}\right\|_2^2 < \varepsilon$
Output the reconstructed temperature field $T = \frac{1}{nRs^2}$

5.5 Simulation results and discussion

5.5.1 Simulation setup

In this section, the performance of the proposed NCGD method is evaluated with a series of numerical simulations. The performance of NCGD was compared with that of the conventional SIRT method using the straight ray model (4.1), the NGD method (5.4) using the bent ray model which have been popularly applied in the acoustic tomography image reconstruction problems. The sensor array setup is illustrated in Figure 3-2.

Three representative dynamic phantoms of the temperature field are used to evaluate the reconstruction performance, as shown in Figure 5-4. The first two phantoms feature one or two Gaussian peaks on top of a flat plane. These two temperature fields have a relatively large gradient, with a maximum gradient of $3.24 \times 10^3\ K/m$ and $3.31 \times 10^3\ K/m$. The third phantom approximates a sectioning image of the flame temperature field in a combustion chamber, which has lower average temperature in the inner zone than the outer zone. The phantom has a smaller temperature gradient with $642.33\ K/m$. The 4th phantom is more complex than the other three phantoms. It has four Gaussian peaks with different shapes. The maximum temperature gradient is $3.91 \times 10^3\ K/m$.

Figure 5-4 also gives the calculated ray trajectories for the three phantoms. For phantoms 1 and 2, the ray paths are bent towards the heat sources clearly due to the large temperature field gradient. For phantom 3, when the gradient is relatively small, the calculated ray path is much closer to straight lines. It is also noticeable that, due to the refraction effect, the ray trajectories are more likely concentrated around the heat sources. The acoustic rays prefer to travel through heated areas, therefore the TOF measurements are more sensitive to this area.

5.5.2 Reconstruction results

To quantitatively evaluate the overall reconstruction quality, four metrics, namely, image relative error (IE), Dislocation (DL), Peak value (PV), and Widening (WD) are adopted. IE evaluates the overall quantitative accuracy of the image reconstruction, while PV focuses on the local reconstruction accuracy of the temperature peaks. DL evaluates the performance of the reconstruction algorithm on localising the centre of the heat source. WD assesses the extent of reconstruction image distortion in shape. Detailed definitions about these four image reconstruction metrics can be found in section 4.4.1.

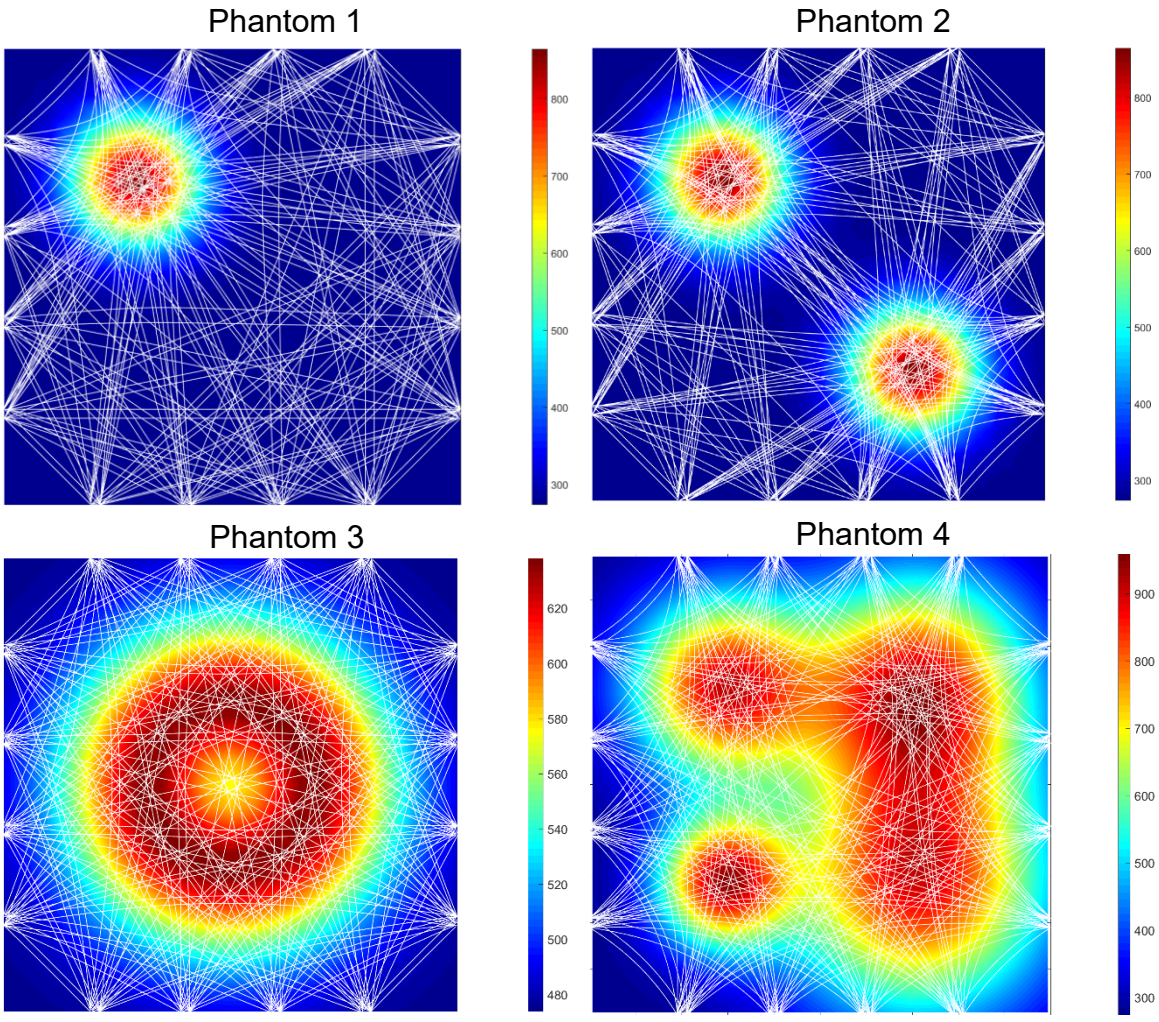

Figure 5-4: The four temperature field phantoms for simulation test (temperature in Kelvin)

In this simulation, the measurement SNR is set to be 40 dB for the simulation tests, which is close to the measurement noise level in the lab-scale experiments. The calculation of PV and DL is based on the heat centre information of the phantoms. To calculate WD, the median value of the reconstruction temperature field is used as the threshold. Simulation is repeated 20 times for each phantom and the mean values of the 4 quantitative metrics are presented in Table 5-5. The image reconstruction results are presented in Figure 5-5.

Table 5-5: The quantitative reconstruction metrics

		Phantom 1	**Phantom 2**	**Phantom 3**	**Phantom 4**
IE (%)	SIRT	14.01	18.38	1.65	10.08
	GD	5.88	8.53	1.35	6.44
	NCGD	4.05	5.84	0.64	3.42
PV (%)	SIRT	29.74	20.84	2.6	4.74
	GD	6.77	6.77	1.83	4.17
	NCGD	4.25	4.25	1.39	0.32
DL (%)	SIRT	7.07	37	43	0.14
	GD	5	19.6	17.4	0.1
	NCGD	5	6.3	3.5	0.05
WD	SIRT	2.52	2.05	1.19	1.89
	GD	1.32	1.23	1.03	1.06
	NCGD	1.21	0.73	1.06	0.97

Firstly, for the reconstruction results of phantom 1, both the proposed NCGD method and the NGD method achieved a significant improvement in the quantitative metrics compared to the conventional SIRT method. With the use of bent ray model, the NCGD and NGD can accurately recover the shape, heat centre location and peak value of the temperature field and the overall image error is reduced to 5.31% and 6.58% respectively for the IE for overall accuracy. On the contrary, due to the use of the straight ray model, large image distortion occurs in the SIRT reconstruction, which results in a large error in PV and WD.

For the reconstruction of phantom 2, only the NCGD method can achieve satisfactory reconstruction results, that the overall IE is 6.04% and the shape, peak value and heat centre location can be accurately recovered. The NGD method can still provide good temperature field reconstruction with IE of 8.79%. However, it cannot be used to accurately locate heat centre and recover the shape of the heated area. The reconstruction performance of the NGD method is largely affected when the temperature field is slightly more complex.

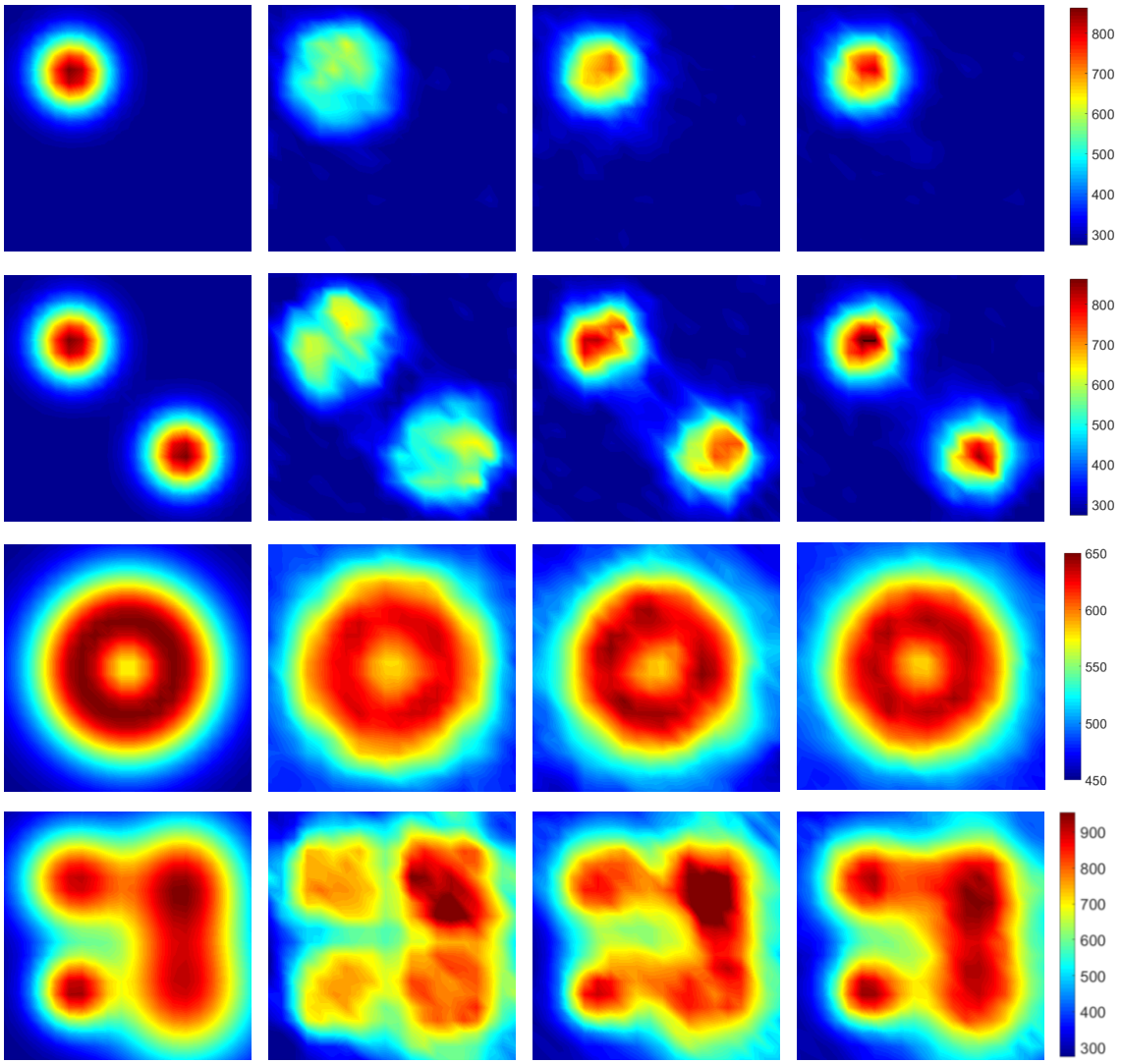

(a) *(b)* *(c)* *(d)*

Figure 5-5: The original temperature phantoms (a) and the reconstructed image results with the noisy simulation data (SNR=40 dB) using the conventional SIRT method (b), the GD method (c), and the NCGD method (d) From top to bottom are the reconstruction results for phantoms 1, 2, 3 and 4 respectively (temperature in Kelvin)

The third phantom is a simple simulation for the temperature of the flame temperature, which is relatively lower in the inner zone. From the reconstruction results, the improvement of using NGD and NCGD is not obvious. All three methods have good accuracy for the temperature field reconstruction in terms of shape, peak value, heat centre location and overall image reconstruction accuracy. This is due to the fact that the original

temperature field has a much smaller gradient compared to the first two phantoms, and that the nonlinear reconstruction using the bent ray model may not have the advantage of better modelling accuracy since the ray paths are very close to straight lines.

For the fourth phantom, both GD and NCG method are able to recover the general shape of the heated area, with WDs of 1.06 and 0.97 respectively. On the contrary, the reconstructed image using the SIRT method suffers from large image distortion, with a WD of 1.89. For the reconstruction of heat centre information, the NCG method outperformed other two methods in terms of DL and PV. The image errors for SIRT, GD and NCG are 10.08, 6.44, and 3.42 respectively. Again, the NCG method provided a better image than other two methods.

To evaluate the noise tolerance of the reconstruction methods, measurements at different noise levels are used in the simulation. The averaged metrics of the phantoms 1 and 2 under different SNR condition are plotted in Figure 5-6. The metrics of the phantoms 3 and 4 are not included.

From the results shown in Figure 5-6, it can be concluded the proposed NCGD method has a better noise tolerance performance than the NGD method for IE, DL, and PV, especially for the noisy tests of SNR under 40 dB. For the shape metric WD, neither can provide an accurate estimation for low SNR cases. The SIRT method based on the straight ray model suffers from the large modelling error due to the refraction effect. It can be seen from the simulation results that the SIRT method cannot provide an accurate estimation of the temperature field, even with the use of a high SNR or noiseless measurements.

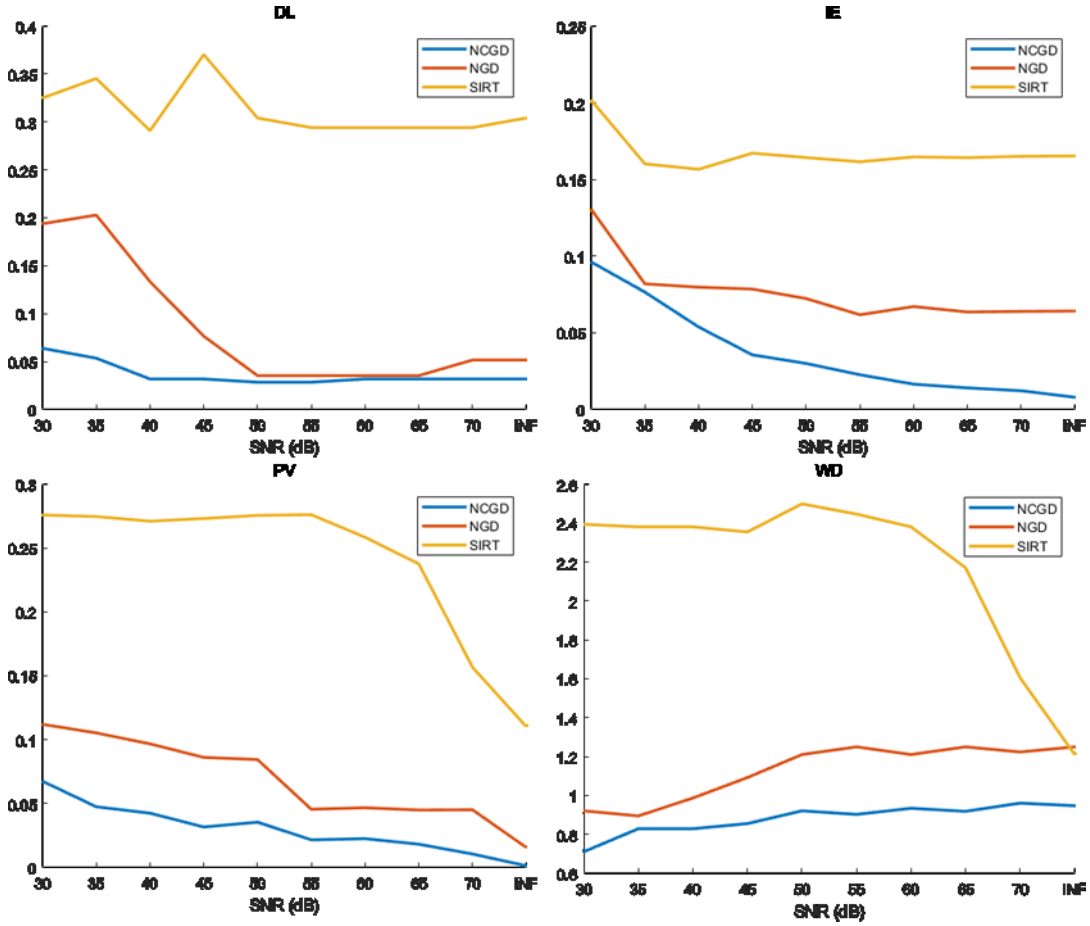

Figure 5-6: Averaged quantitative metrics for different noise level for phantom 1 and 2

The comparison of the computation times between SIRT, NGD and NCGD method is illustrated in Table 5-6. The reconstruction was performed using Matlab 2018b installed on a Windows desktop with an Intel Xeon CPU (E5-1660 v3 @ 3GHz, 8 cores) and 32 GB RAM memory. The computation time using SIRT method is less than 1 seconds, which proves that the SIRT method is more suitable for real-time implementation of acoustic tomography system than the other two methods. Among the two nonlinear reconstruction methods, the computation time using NCGD is less than 40 seconds for the first three phantoms and less than 80 seconds for phantom 4, while the NGD method requires more than 100 seconds.

Table 5-6: Computation time of image reconstruction for each phantom

Method	Phantom 1	Phantom 2	Phantom 3	Phantom 4
SIRT	0.17	0.21	0.28	0.14
NGD	219.71	235.41	145.73	477.47
NCGD	31.95	39.73	38.11	79.10

In summary, both NGD and NCGD, which use the bent ray model, achieve a significant improvement on the reconstruction quality when the temperature field has a large gradient, in terms of the overall quantitative accuracy, the shape of the heated area, the peak value and the location of the heat centre. However, for the temperature field with a small gradient, the improvement brought by the NGD and NCGD methods is very limited. Compared to the conventional regularised NGD method, the NCGD has various advantages: (1) the improved tolerance to measurement noise and ray length matrix perturbation; and (2) good convergence performance towards the local minimum. These features are important especially for the ill-conditioning of the ray length matrix here, as the conjugate gradient direction can follow narrow (ill-conditioned) valleys, whereas the NGD method slows down and follows a criss-cross pattern.

5.6 Summary

In this chapter, a nonlinear acoustic tomographic reconstruction algorithm using the bent ray model is developed. The proposed NCGD reconstruction algorithm advances (1) the nonlinear conjugate gradient descent method to solve the nonlinear inverse problem; (2) the fast acoustic ray tracing given the sound speed distribution using FMM; and (3) the line search for optimal step size. Simulation results show that, the NCGD method achieves a significant improvement on reconstruction image quality compared to the conventional

SIRT method. It also outperforms the commonly used NGD method in terms of image quality, noise robustness, and computation speed.

Chapter 6 Large scale acoustic tomography for wind velocity field reconstruction

6.1 Introduction

Improved knowledge of the wind velocity field of the near surface atmosphere is of great importance in many applications, such as the boundary layer meteorology, theories of turbulence, visualization of different dynamic processes, studies of sound wave propagation through a turbulent atmosphere, etc [30]. In order to reconstruct the wind velocity field without disturbing these meteorological quantities, remote sensing techniques are required.

Acoustic tomography has proved to be an effective remote sensing technique for the near surface atmosphere monitoring [53, 77, 105]. The first implementation of this technique was in the early 20^{th} century, where the vertical structure of the air due to powerful explosions was recorded based on acoustic tomography. Later, the acoustic tomography was used to investigate the audible zones, especially the atmospheric surface layer [17, 53, 57, 106, 107]. The cross-sectioning image of the wind velocity field can be reconstructed from the TOF measurements. Compared to other remote sensing techniques, for instance, the conventional radar and the volume imaging Lidars [108-110], the acoustic tomography system has the advantages of having a low equipment and maintenance cost, scalable measurement range and the ability to simultaneously reconstruct both the temperature and the wind velocity fields.

However, there remain two main problems before large-scale acoustic tomography can be applied for practical applications:

(1) Compared to applications in the combustion chamber and the lab-scale indoor atmosphere environment, the sensing area of remote sensing acoustic tomography is relatively large. According to Barth's study [105], the

investigation area varies from an extent of tens of square metres to hundreds of square metres. Therefore, one of the major challenges towards employing acoustic tomography for large scale monitoring is the temporal resolution. In order to capture the dynamical changes of the temperature and wind velocity fields, a fully parallel TOF measurement scheme should be used to reduce the measuring time per frame. Further, in order to separate the received waveforms and accurately measure their individual TOFs along different ray path, broadband acoustic waveforms with good auto-correlation property were used [18].

(2) Compared to the scalar field tomographic reconstruction of the temperature field, the vector field tomographic reconstruction of the wind velocity field is generally different. According to Norton's research [111], the unique reconstruction of the bounded vector field required both the longitudinal and transverse line integral measurement, while in the acoustic tomography system, only the longitudinal integral measurements (TOFs) were available. Jovanovic [61] proposed an angle of departure/arrival measurements method to obtain the transversal measurements. However, this technique requires a specially designed transducer array, with three transmitters and receivers to form an acoustic tri-pole in each site, which is generally not practical for large scale monitoring. In this chapter, it will be illustrated that the 2D horizontal wind velocity field can be a divergence-free vector field. On the basis of this, a divergence-free regularised algorithm is used to recover the wind velocity field with good quantitative accuracy.

The previous chapters have explained in detail about the temperature field reconstruction using acoustic tomography techniques, and for large-scale acoustic tomography, the reconstruction of the temperature field is similar. Therefore, this chapter mainly focuses on the fully parallel TOF measurement scheme and the wind velocity reconstruction algorithm. The orthogonal acoustic waveforms based on the filtered and modulated Kasami sequence and divergence-free vector field regularised reconstruction methods are studied to accelerate TOF measurements and improve wind velocity

reconstruction accuracy. Numerical simulations are carried out to validate the performance of the proposed methods.

6.2 Large scale acoustic tomography system

Acoustic tomography mainly utilises the strong dependence of sound propagation on the spatial distribution of air temperature and velocity. A typical setup for large scale acoustic tomography system is illustrated in Figure 6-1. The whole square sensing area is surrounded by 16 acoustic transceivers (for the large-scale sensing area, the transmitter and receiver are placed at the same spot). The TOFs between each transducer pairs are recorded along 96 ray paths. Given the position of the transceivers and the TOF measurements, the corresponding wind velocity field can be recovered. The acoustic transducer array covers a sensing area of 100 by 100 m and the reconstructed image is a 20 by 20 vector field with 5 meter resolution.

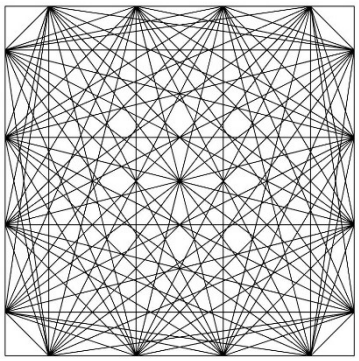

Figure 6-1: Acoustic tomography transducer array setup

The forward problem has been defined in Chapter 2, which uses the back and forth TOF measurements τ_+ and τ_- to measure the line integrals of the wind velocity field, the forward problem in matrix form can be written as

$$\boldsymbol{l} = \boldsymbol{SV} \tag{6.1}$$

The tomographic reconstruction of the temperature and wind velocity is to compute the optimal $\boldsymbol{V} = [\boldsymbol{V_x}, \boldsymbol{V_y}]$ using the TOF measurements.

6.3 Parallel TOF measurement

In conventional acoustic tomography systems, each transceiver is switched on sequentially to transmit acoustic signals to the receivers. The interference for TOF detection is relatively small since acoustic signals from different sources are separated in different time slots at the receiver. However, the temporal resolution of the system is sacrificed, and it may not able to capture the dynamic temperature changes in the sensing area.

To improve the temporal resolution for large scale monitoring, a fully parallel data collection scheme should be used. It requires all the transceivers of the acoustic tomography system to transmit and receive acoustic signals simultaneously. From the received waveforms at each receiver, TOFs according to all different transmitters are estimated separately with good quantitative accuracy. As a result, the measuring time is significantly reduced compared to the pairwise sequential measurement strategy.

The challenging part of the parallel TOF estimation is how to separate the received signal waveforms from different transmitter. To solve this problem, all the waveforms from different transmitters are designed with special signature. Therefore, they are orthogonal to each other. Then TOFs can be estimated based on the cross-correlation method.

6.3.1 Cross-correlation TOF estimation

For the cross-correlation TOF estimation, the TOF is considered as the time delay of the received signal with respect to the reference source signal. This correlation-based method is very robust against uncorrelated additive noise. However, as mentioned before, to extract this time delay from the received signal, the following conditions must be met: (1) the received signal is embedded in White Gaussian Noise (WGN), and (2) the received signal is the time-shifted, amplitude-scaled replica of the reference signal.

For the first condition, since the transmitted waveforms from different transmitters are considered to interfere with each other, it is required that all

the transmitted waveform should be uncorrelated to each other. For the second condition, a better acoustic air transducer should be used for robust sound propagation to reduce waveform distortion at the receiver.

Using the fully parallel data collection scheme, each received signal is a summation of all other 12 delayed source signals.

$$y_j(t) = \sum_{i=1}^{12} x_i\left(t - \Delta t_{i,j}\right) + n_j(t), i \neq j \tag{6.2}$$

where $y_j(t)$ refers to the received signal at *j*-th receiver, $x_i(t)$ is the source signal from *i*-th transmitter and $\Delta t_{i,j}$ represents their corresponding delay time, which is the TOF in *i*-th ray path. $n_j(t)$ is the local noise received at *j*-th receiver.

The summed transmitted waveforms can be firstly separated at the receiver. Then their individual delay time $\Delta t_{k,j}$ can be estimated based on the cross-correlation detection defined below.

$$\begin{aligned} R_{y_j x_k}(l) &= E[y_j(t)x_k(t-l)] \\ &= E[[\sum_{i=1}^{P} x_i(t-\Delta t_{i,j}) + n_j(t)]x_k(t-l)] \\ &= \sum_{i=1,i\neq k}^{P} R_{x_i x_k}(l-\Delta t_{i,j}) + R_{x_k x_k}(l-\Delta t_{i,j}) + R_{n_j x_k}(l) \end{aligned} \tag{6.3}$$

where *l* denotes the correlation delay, P denotes the number of received waveforms, and the noise term $n_j(t)$ is uncorrelated with the source signal x_i, and x_k is the k-th reference signal waveform for cross-correlation detection. $R_{x_i x_k}$ denotes the cross-correlation function between $x_i(t)$ and $x_k(t)$.

Qu [11] used the normalised correlation function for TOF estimation. Although this normalization process will help to provide a scale-free strength of the statistical dependence, in this research the received signal sequence isn't normalised for two reasons: (1) the TOFs are determined by the maximum of the correlation coefficients, therefore their accuracy will not be affected by the

absolute value of the coefficients; and (2) the received signal contains different waveform components from different transmitters and their power levels are quite different from each other. It is actually difficult to scale these components with specific weights.

The global maximum location of the cross-correlation $R_{y_j x_k}(l)$ indicates the delay time. The correlation-based TOF estimation is robust against additive random noise, therefore the conventional denoising technique is not necessary. However, the waveform distortion and interference will largely affect the TOF estimation accuracy. Therefore, a proper window is also necessary to prevent the miss-leading local maximum of the correlation values.

6.3.2 Source signal design

It is important to minimise the interference term $\sum_{i=1,i\neq j,i\neq \mathrm{k}}^{12} R_{x_i x_k}(l-\Delta t_{i,j})$ and noise term $R_{n_j x_i}(l)$ in the cross-correlation TOF estimation. All the source signal waveforms should have good correlation property, such as sharp auto-correlation peak, but low cross-correlation value, for arbitrarily random delay $\Delta t_{i,j}$ and uncorrelated to the noise at the receiver.

The Maximum Length Sequence (MLS) has a good asynchronous orthogonal property, which could be used to separate different source signals with arbitrary delay at the receiver. However, when a large number of simultaneous acoustic sources have to be used, such as the 12 used in this case, the cross-correlation property of the MLS is relatively poor. Selecting and combining the preferred pairs of the MLS together can improve cross-correlation property, like the Kasami sequence. In fact, the Kasami sequence has near optimal cross-correlation values close to the Welch lower bound[112].

Therefore, the Kasami sequence shown in Figure 6-2 is selected to generate acoustic signals for source signal separation and TOF detection. However, it is difficult to practically generate and transmit the Kasami sequence with the acoustic transceivers, because the spectrum of the Kasami sequence is arbitrarily wide with sharp edges and discontinuous in the time domain, but the

transceiver is restricted to a limited bandwidth around a certain frequency. Therefore, before transmission, the Kasami sequence is modulated with fixed carrier frequency, then a band-pass filter is used to smooth the Kasami sequence and control its bandwidth to fit into the transducer's specifications.

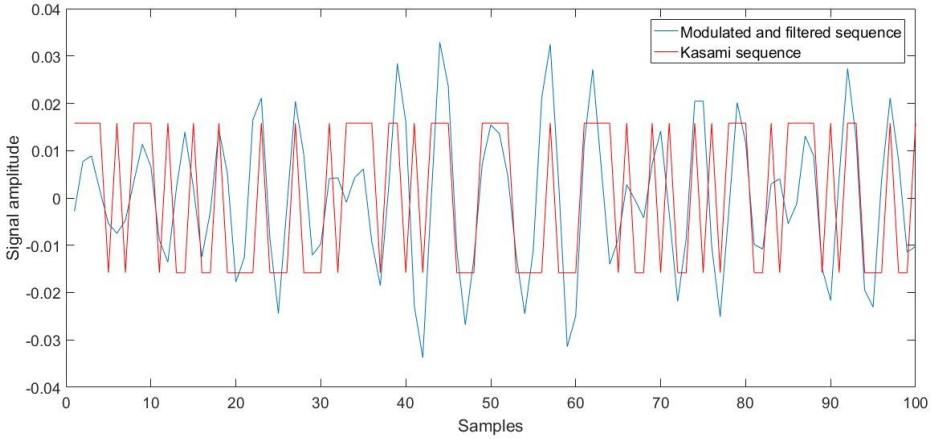

Figure 6-2: Kasami sequence (red) and the output signal (blue) after modulation and band-pass filter.

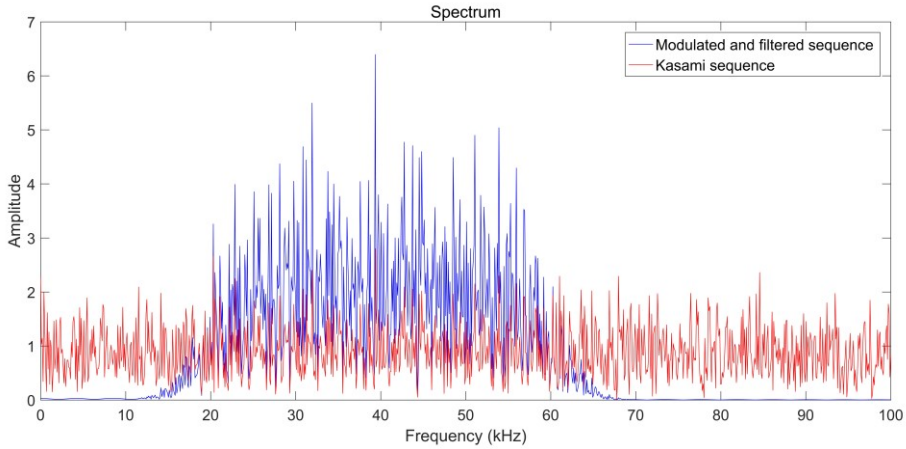

Figure 6-3: Kasami sequence (red) and modulated and filtered output sequence (blue) in frequency domain. After modulation and band-pass filter, the bandwidth of output signal is limited and centred at the 500Hz carrier frequency.

As shown in Figure 6-3, compared with the original Kasami sequence, the modulated and filtered Kasami sequence has a narrower bandwidth, which can

meet the transmission requirement for acoustic transceivers. However, modulation and filtering will also weaken the correlation property of waveform. The auto- and cross-correlation comparison is given in Figure 6-4 and Figure 6-5 respectively. The auto-correlation coefficients of the filtered Kasami sequence is a smoothed version of the original correlation of Kasami sequence. The auto-correlation peak value is reduced while the cross-correlation value, which can be considered as the interference in TOF detection, is increased. Once the interference and noise overwhelm the auto-correlation peak value, it is impossible to detect an accurate travel-time delay from the received signal. Besides, at the receiver, it is difficult to build an inverse filter to remove the smooth effect, as many zeros exist in the impulse response of the band-pass filter. The only way to enhance the auto-correlation property is to increase the length of the Kasami sequence and to produce a sharp auto-correlation peak. Meanwhile a good temporal resolution must remain for the acoustic tomography system.

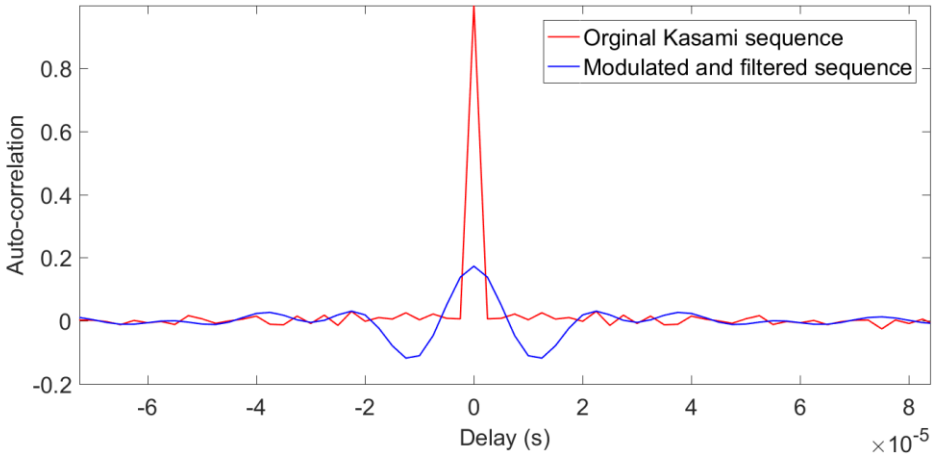

Figure 6-4: Auto-correlation of Kasami sequence (red) and modulated and filtered output sequence (blue). The auto-correlation of the filtered sequence has larger sidelobes and lower peak value than that of the Kasami sequence.

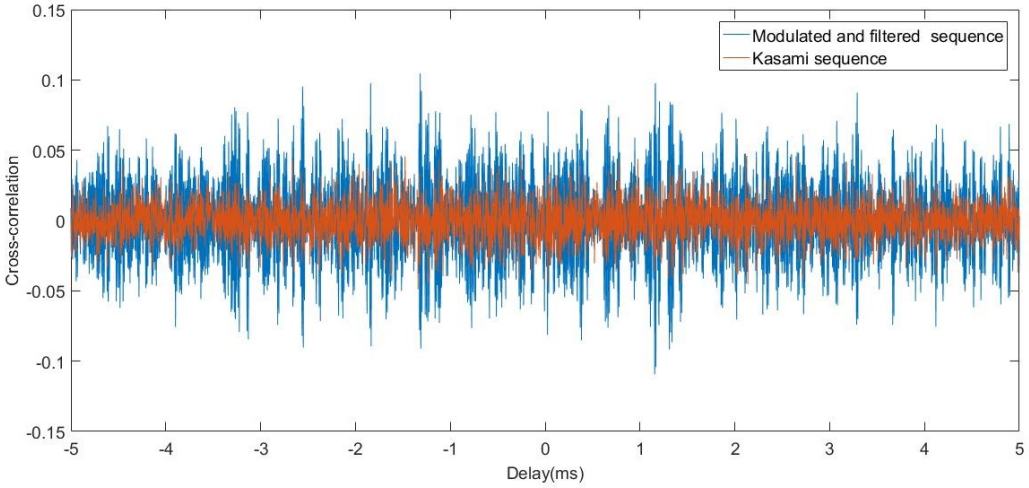

Figure 6-5: Cross-correlation of Kasami sequence (red) and modulated and filtered sequence output (blue). The cross-correlation value of the filtered sequence is much larger than the Kasami sequence, which results in a larger interference in TOF detection.

In summary, in order to improve the temporal resolution of TOF measurement, the wideband acoustic signal waveform is designed based on the modulated and filtered Kasami sequence, which allows simultaneous signal transmission and data collection from all the acoustic ray paths. Then, the accurate TOF measurements along each ray path can be calculated by correlation detection.

6.4 Wind velocity field reconstruction

6.4.1 Invisible field problem

The reconstruction of the wind velocity field from TOF measurements is considered to be a vector tomography problem. According to theoretical analysis of vector tomography, a major challenge in vector tomography is the invisible field problem [57, 61, 111], that the curl-free component of the vector field is ‘invisible’ to the longitudinal integral measurements (TOFs) and that only the divergence-free component can be uniquely reconstructed. To illustrate the ‘invisible’ field effect more clearly, a brief description is given below:

Based on Helmholtz's theorem, a bounded wind velocity field $\boldsymbol{v}$ can be uniquely decomposed into three components.

$$\boldsymbol{v} = \boldsymbol{v}_s + \boldsymbol{v}_I + \boldsymbol{v}_H \tag{6.4}$$

where solenoidal (divergence-free $\nabla \cdot \boldsymbol{v}_S = 0$) component v_S, irrotational (curl-free $\nabla \times v_I = 0$) component v_I, and harmonic ($\nabla \cdot v = 0, \nabla \times v_H = 0$) component v_H.

Apply this to equation (2.10) and use the potential function representation $V_I = \nabla\phi$ and $V_S = \nabla \times \psi$,

$$\begin{aligned} l_\Gamma &= \int_{s_t}^{s_r} \boldsymbol{v}_I + \boldsymbol{v}_S + \boldsymbol{v}_H \, d\boldsymbol{s} \\ &= \int_{s_t}^{s_r} \left[\left(\frac{\partial \phi}{\partial x}, \frac{\partial \phi}{\partial y} \right) + \left(\frac{\partial \psi}{\partial y}, -\frac{\partial \psi}{\partial x} \right) + \left(v_{H_x}, v_{H_y} \right) \right] \cdot (\cos\theta dx, \sin\theta dy) \\ &= \phi(sx_r, sy_r) - \phi(sx_t, sy_t) + \int_{sx_r}^{sx_t} \left(\frac{\partial \psi}{\partial y} + v_{H_x} \right) \cos\theta dx \\ &\quad + \int_{sy_r}^{sy_t} \left(-\frac{\partial \psi}{\partial x} + v_{H_y} \right) \sin\theta dy \end{aligned} \tag{6.5}$$

Equation (6.5) shows that, for the irrotational component ϕ, only the boundary value $\phi(sx_r, sy_r) - \phi(sx_t, sy_t)$ has contribution to the longitudinal line integral measurements. In other words, the irrotational vector field inside the sensing area is invisible according to the TOF measurements, and thus cannot be recovered. For v_S and v_H, which added up as a divergence-free vector field, do not has this invisible field problem.

Besides, the 2D horizontal wind velocity field can be considered as a divergence-free vector field. This assumption is valid as the stratification in the atmosphere caused by gravity makes the horizontal velocity $\boldsymbol{v_{xy}}$ great than the vertical velocity $\boldsymbol{v_z}$ by a factor of 10-100. Usually for the time-averaged data as is used here, $\boldsymbol{v_z}$ can be ignored. Therefore $\boldsymbol{v_{xy}}$ becomes a divergence-free vector field.

$$\nabla \cdot \boldsymbol{v}_{xy} = \frac{\partial \boldsymbol{v}_x}{\partial x} + \frac{\partial \boldsymbol{v}_y}{\partial y} = -\frac{\partial \boldsymbol{v}_z}{\partial z} = 0 \tag{6.6}$$

Among the two divergence-free vector components, v_S and v_H, of the horizontal wind velocity field, it has been proved that [61], without any other information, both can be uniquely recovered from the longitudinal integral measurements.

6.4.2 Divergence-free regularised vector tomography

The inverse problem for the velocity reconstruction has the general form:

$$\min_{\boldsymbol{V}} \left\| \boldsymbol{l} - \boldsymbol{S}\boldsymbol{V} \right\|_2^2 + \lambda R(\boldsymbol{V}) \tag{6.7}$$

where $\|\boldsymbol{l} - \boldsymbol{S}\boldsymbol{V}\|_2^2$ is the data fitting term and $\lambda R(\boldsymbol{V})$ is the regularisation term, which is constructed based on *priori* knowledge of the vector field.

So far, we have shown that the wind velocity field reconstruction is to recover the divergence-free component, both the v_S and v_H, from line integrals. Bringing this *priori* to the reconstruction equation (6.7), it can be further formulated as:

$$\min_{\boldsymbol{V}} \left\| \boldsymbol{l} - \boldsymbol{S}\boldsymbol{V} \right\|_2^2 + \eta \left\| \nabla \cdot \boldsymbol{V} \right\|_1 + \lambda \left\| \boldsymbol{R}\boldsymbol{V} \right\|_2^2 \tag{6.8}$$

where $\|\nabla \cdot \boldsymbol{v}\|_1$ and $\|\boldsymbol{R}\boldsymbol{V}\|_2^2$ are the divergence-free regularisation term and the vector smoothness regularisation respectively. η and λ are the two regularisation parameter.

A discrete 2nd order finite differential approximation is used inside the sensing area and a 1st order differential is used for the boundary pixel.

$$\nabla^{x}_{i,j}\cdot\boldsymbol{v}=\begin{cases}\dfrac{v_x(i-1,j)+v_x(i{+}1,j)\text{-}2v_x(i,j)}{2d}\\ \dfrac{v_x(i-1,j)\text{-}v_x(i,j)}{d},\ \text{left boundary}\\ \dfrac{v_x(i+1,j)\text{-}v_x(i,j)}{d},\ \text{right boundary}\end{cases}\tag{6.9}$$

Therefore a divergence operator can be defined for linear operation as: $\boldsymbol{DV}=\nabla\cdot\boldsymbol{v}$ and $\mathbf{D}=[\boldsymbol{D_x}\quad\boldsymbol{D_y}]$ is the divergence operator and $\boldsymbol{D_x},\boldsymbol{D_y}\in\mathbb{R}^{N*N}$ are the two directional discrete differentials built based on equation (6.9).

The third term $\lambda\|\boldsymbol{R}\mathrm{V}\|_2^2$, is the vector smoothness constraints, and $\boldsymbol{R}$is the vector Laplace operator. The vector Laplace operator is defined as:

$$\begin{aligned}\boldsymbol{RV}=\nabla^2\boldsymbol{v}&=\left(\nabla^2\boldsymbol{v}_x,\nabla^2\boldsymbol{v}_y\right)\\&=\left(\frac{\partial^2\boldsymbol{v}_x}{\partial x^2}+\frac{\partial^2\boldsymbol{v}_x}{\partial y^2},\frac{\partial^2\boldsymbol{v}_y}{\partial x^2}+\frac{\partial^2\boldsymbol{v}_y}{\partial y^2}\right)\\&=\left(\left(\partial^2_{xx}+\partial^2_{xx}\right)\boldsymbol{v}_x,\left(\partial^2_{xx}+\partial^2_{xx}\right)\boldsymbol{v}_y\right)\\&=\left[\boldsymbol{D_xD_x}+\boldsymbol{D_yD_y},\boldsymbol{D_xD_x}+\boldsymbol{D_yD_y}\right]V\end{aligned}\tag{6.10}$$

Therefore, $\boldsymbol{R}=\left[\boldsymbol{D_xD_x}+\boldsymbol{D_yD_y},\boldsymbol{D_xD_x}+\boldsymbol{D_yD_y}\right]$

6.4.3 Tomographic reconstruction

The inverse problem can be rewritten as:

$$\boldsymbol{V}=\min_{\boldsymbol{V}}\left\|\boldsymbol{l}\text{-}\boldsymbol{SV}\right\|_2^2+\eta\left\|\boldsymbol{DV}\right\|_1+\lambda\left\|\boldsymbol{RV}\right\|_2^2\tag{6.11}$$

Augmented pseudo-measurement and ray length matrix can be used to simplify the objection function:

$$V=\min_{V}\left\|\hat{}\qquad\quad\eta\left\|\boldsymbol{DV}\right\|_1\right.\tag{6.12}$$

where

$$\boldsymbol{S} = \begin{bmatrix} \boldsymbol{S} \\ \sqrt{\lambda}\boldsymbol{R} \end{bmatrix} \tag{6.13}$$

To solve the inverse problem, the alternating direction method of multipliers (ADMM) strategy is used to split the inverse problem into easier sub-problems[113]. By introducing an additional variable $\boldsymbol{Z}$.

$$\begin{aligned} &\min_{\boldsymbol{V},\boldsymbol{Z}} \| \qquad \|_2 \quad \eta\|\boldsymbol{Z}\|_1 \\ &\text{s.t. } \boldsymbol{Z} = \boldsymbol{D}\boldsymbol{V} \end{aligned} \tag{6.14}$$

The corresponding augmented Lagrangian function is

$$L_\rho(\boldsymbol{Z},\boldsymbol{V},\boldsymbol{\gamma}) = \bar{\boldsymbol{l}} - \bar{\boldsymbol{S}}\boldsymbol{V}_2^2 + \eta\boldsymbol{Z}_1 + \boldsymbol{\gamma}^T(\boldsymbol{Z} - \boldsymbol{D}\boldsymbol{V}) + \rho\boldsymbol{Z} - \boldsymbol{D}\boldsymbol{V}_2^2$$

where ρ is the positive constraints and $\boldsymbol{\gamma}$ is the multiplexer.

ADMM solves the inverse problem by iteratively solving three sub-problems, and the details are illustrated in Table 6-1.

Table 6-1: ADMM for solving the inverse problem in equation (6.14)

Initialise: $\mathbf{V_0}$, λ, η, ρ, α, ϵ
Iteration
Step 1 solve the **V** sub-problem $$\boldsymbol{V}_{k+1} = \min_{\boldsymbol{V}} L_\rho \left(\boldsymbol{Z}_k, \boldsymbol{V}, \boldsymbol{\gamma}_k \right)$$
Step 2 solve the **Z** subc-problem: $$\boldsymbol{Z}_{k+1} = \min_{\boldsymbol{Z}} L_\rho \left(\boldsymbol{Z}, \boldsymbol{V}_{k+1}, \boldsymbol{\gamma}_k \right)$$
Step 3 update the multiplexer: $$\boldsymbol{\gamma}_{k+1} = \min_{\boldsymbol{\gamma}} L_\rho \left(\boldsymbol{Z}_{k+1}, \boldsymbol{V}_{k+1}, \boldsymbol{\gamma} \right)$$
Until a stopping criterion is satisfied $$\left\| \boldsymbol{V}_{k+1} - \boldsymbol{V}_k \right\|_2^2 \le \epsilon$$
Output the vector field

For the first, the $\boldsymbol{V}$ sub-problem is a quadratic minimisation problem.

$$\boldsymbol{V}_{k+1} = \min_{\boldsymbol{V}} \left\| \hat{} \qquad \right\|_2 \boldsymbol{\gamma}_k^T \left(\boldsymbol{Z}_k \text{ - } \boldsymbol{D}\boldsymbol{V} \right) + \rho \left\| \boldsymbol{Z}_k \text{ - } \boldsymbol{S}\boldsymbol{V} \right\|_2^2 \tag{6.15}$$

which can be easily solved with an exact gradient-based solution.

$$\boldsymbol{V}_{k+1} = \left(\boldsymbol{S}^T \boldsymbol{S} + \rho \boldsymbol{D}^T \boldsymbol{D} \right)^{-1} \left(\boldsymbol{S}^T \hat{} \qquad + \boldsymbol{D}^T \boldsymbol{\gamma}_k \right) \tag{6.16}$$

The $\boldsymbol{Z}$ sub-problem contains the divergence-free regularisation, which can be considered as a lasso problem in its Lagrangian form[114].

$$\boldsymbol{Z}_{k+1} = \min_{\boldsymbol{Z}} \eta \left\| \boldsymbol{Z} \right\|_1 + \gamma_k^T \boldsymbol{Z} + \frac{\rho}{2} \left\| \boldsymbol{Z} - \boldsymbol{D}\boldsymbol{V}_{k+1} \right\|_2^2 \tag{6.17}$$

It has a naive solution using a shrinkage operator.

$$\boldsymbol{Z}_{k+1} = \mathcal{T} \qquad -\boldsymbol{\gamma}_k / \rho\big) \tag{6.18}$$

$\mathcal{T}$ is the shrinkage operator defined by

$$\mathcal{T} \qquad |\boldsymbol{Z}| - \eta\big)_+ \operatorname{sgn}(\boldsymbol{Z}) \tag{6.19}$$

Then the multipliers updated as:

$$\boldsymbol{\gamma}_{k+1} = \boldsymbol{\gamma}_k - \alpha(\boldsymbol{Z}_{k+1} - \boldsymbol{D}\boldsymbol{V}_{k+1}) \tag{6.20}$$

where α is the step size.

Finally, several remarks on the reconstruction method are listed below:

1) The horizontal wind velocity field can be considered as a solenoidal vector field due to stratification. This property is utilised as the *priori* knowledge and the divergence-free regularisation is applied to improve the reconstruction quality.

2) Vector Laplacian regularisation is used as the smoothness penalty term.

3) ADMM is used to divide the inverse problem into easier sub-problems, to iteratively solve the sub-problems with accuracy.

6.5 Simulation results and analysis

6.5.1 TOF estimation

For the purpose of real-time measurement, the acoustic signal waveform is designed based on the modulated and filtered Kasami sequence. Correlation detection is used to estimate the TOF. In the simulation, all the transmitted signals reached the receivers with a pre-set delay. According to Jovanovic [61], if the measurement noise is considered to be white Gaussian noise for

simplicity, the Cramer-Rao lower bound for the cross-correlation TOF estimation is:

$$\sigma_t^2 = \frac{1}{8\pi^2}\frac{1}{SNR}\frac{1}{TW}\frac{1}{f_c^2}\frac{1}{\left(1+W^2/12f_c^2\right)^2} \tag{6.21}$$

where the measuring time of TOF is set to be 1 s. The courier frequency $f_c = 500Hz$ and the measurements SNR is set to be 50dB. Jovanovic claimed that the cross-correlation TOF estimator could touch the Cramer-Rao lower bound, which is true only when the following condition is met: (1) the number of samples is sufficiently large with sampling frequency $f_s \to \infty$; and (2) the measurement noise is identical in all the acoustic receivers. However, the Cramer-Rao lower bound is used here to roughly estimate the optimal parameter, i.e. the bandwidth W.

In this simulation, the lower bound changes with the selection of bandwidth W. The relationship between the TOF detection error and the normalised bandwidth W is shown in Figure 6-6. Generally, compared with the pairwise TOF measurement process, the length of the transmitted signal is increased from 5 ms to 10 ms and the total measuring times for each transceiver pair increases from 10 ms to 20 ms. However, because the total measuring time per frame is reduced from 160 ms to 20 ms, therefore the system speed is improved from 6.25 frames per second to 50 frames per second. All the parameters of the transmitted acoustic waveform are listed in Table 6-2. An example of the received signal is shown in Figure 6-7, which is the summation of all 15 sources. The cross-correlation detection of the TOFs is shown in Figure 6-8, where the arrival times of transmitted signal from the transceiver 1 to the transceivers 3, 5, 7 and 9 are indicated on the cross-correlation peaks. The overlaps between the pre-set delay and the detected delay demonstrates the excellent accuracy of the TOF detection.

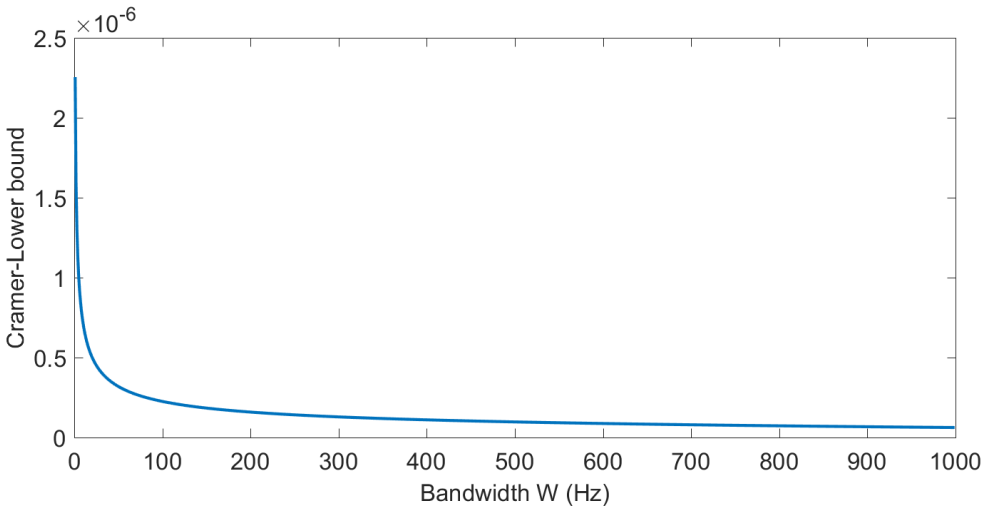

Figure 6-6: Change of CLB for TOF estimation with respect to the normalised band-pass filter bandwidth

Table 6-2: Parameters for generating acoustic waveform

Sampling frequency	10 kHz
Carrier frequency	500 Hz
Band-pass filter bandwidth	300 Hz
Filter normalised bandwidth	0.03
Filter length	81
Filter window	Kaiser
Total measurement time per image	1 s
Pulse duration	0.5 s
Kasami code polynomial	14, 13, 8, 4, 0

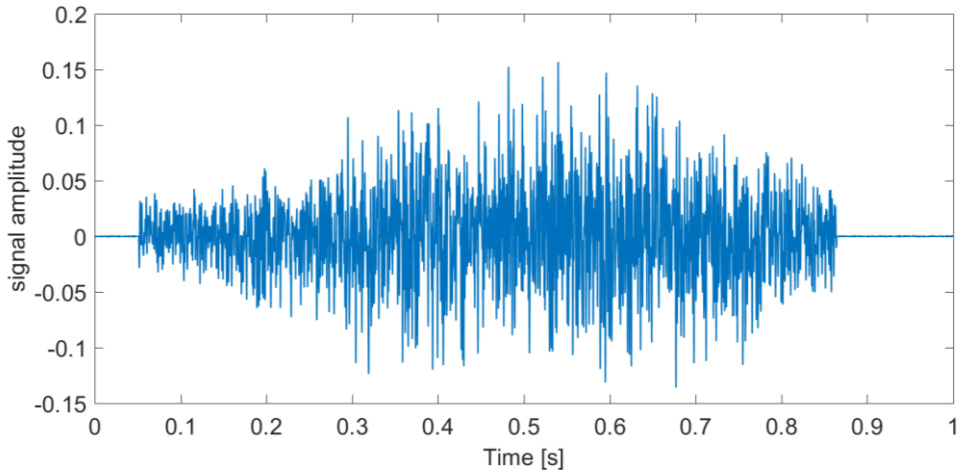

Figure 6-7: Received signal at one transceiver from all other 15 sources. All the transceivers send acoustic signals for 10ms. The measurement time for each image lasts for 20ms.

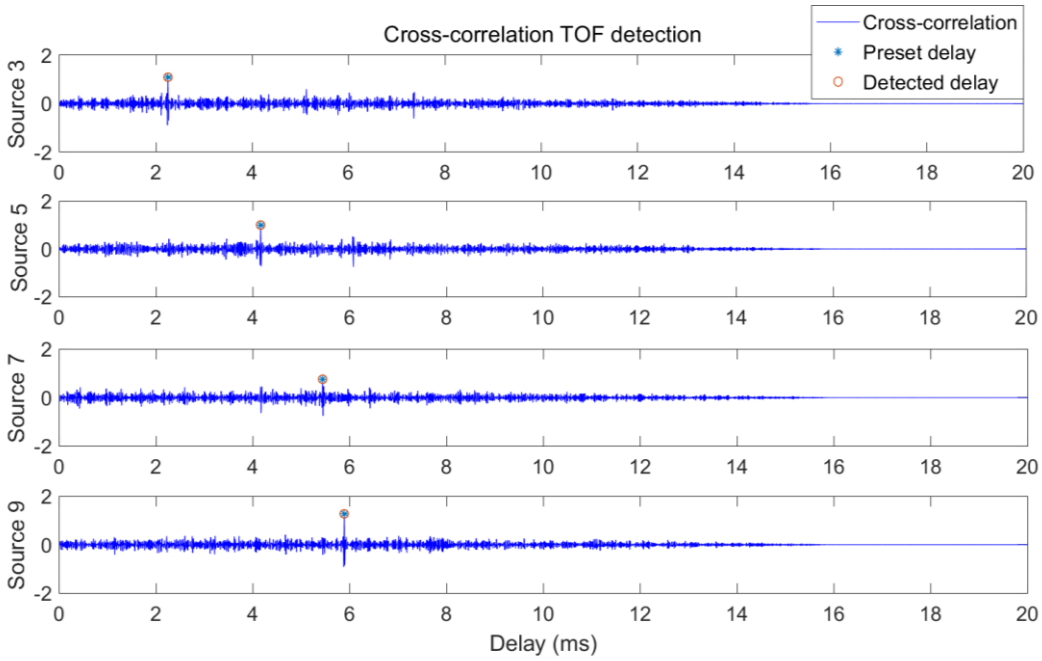

Figure 6-8: Cross-correlation TOF detection results from simulation. The preset delay is marked with '*' and the detected delay is marked in the red circles.

6.5.2 Reconstruction of typical vector field phantoms

The performance of the proposed vector field reconstruction algorithm is tested on three typical vector field phantoms, including the pure solenoidal vector field v_S , the divergence-free vector field containing the harmonic component $v_S + v_H$, and at last, $v_S + v_H + v_I$, which also contains the irrotational vector component when the vertical wind velocity cannot be ignored (much smaller than the solenoidal component by a factor of 10). The three components in the simulation are illustrated in Figure 6-9:

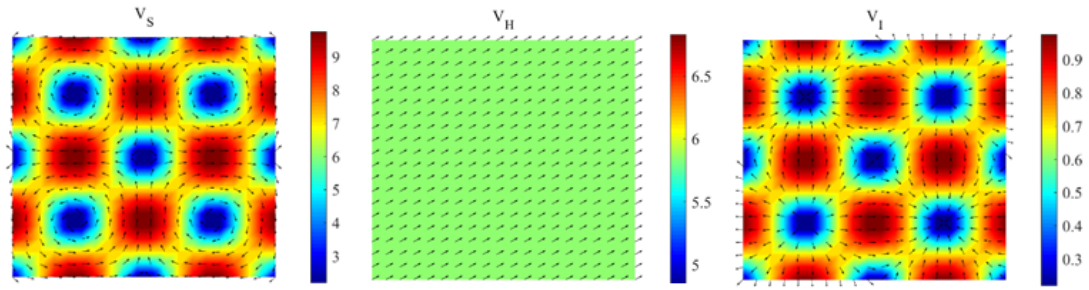

Figure 6-9: Three vector field components, from left to right, the solenoidal vector field v_s , the harmonic vector field v_H and the irrotational vector field. v_I . The wind velocity field unit is m/s

The algorithm parameters, such as the weight parameter λ and η for the divergence-free regularisation and vector Laplacian regularisation, are empirically determined based on a series of practices and the same parameters are applied to the test phantoms, which are 0.1 and 0.01 respectively. To quantitatively evaluate the accuracy of the reconstructed vector field, the relative image error between the reconstructed wind velocity and the true phantom are employed, which is defined as follow:

$$E_{\text{image}} = \frac{\left\| \boldsymbol{V}_{re} - \boldsymbol{V}_{ori} \right\|_2^2}{\left\| \boldsymbol{V}_{ori} \right\|_2^2} \tag{6.22}$$

In the simulation, all the TOF measurements contain white Gaussian noise with different SNR. For each SNR value, 40 reconstructions with different noise

vectors are performed. The averaged image reconstruction error is used to evaluate the reconstruction performance.

Figure 6-10 illustates the wind velocity reconstruction results and the relative image error with 40 dB noise. The first phantom is designed to evaluate the reconstruction accuracy on a pure solenoidal vector field, where the velocity vanishes at the boundary. The reconstruction result correctly shows the vortex shape and center positions. There seems to be some artefacts and small discontinuities on the magnitude of the velocity field, and the relative reconstruction error is 8%, which may be related to the modelling error due to the discretisation of the domain and the lack of measurements (96 ray paths for 16 transceivers).

The second phantom is designed to evaluate the reconstruction accuracy for the source-free vector field with non-zero boundary velocity, which is a more general case. The velocity field contains the harmonic components, which is both source-free and curl-free. Curl-free means that it also has an invisible field problem. Norton [111] has concluded that measurements of the normal velocity on the boundary can be used to resolve the ambiguity of the harmonic part, and therefore v_S and v_H can be recovered separately. Later, Jovanovic further proved that no extra measurements are needed to determine the source-free vector field $v_S + v_H$, although the separation of the two components is not capable in that case. The simulation results here prove this conclusion. The relative reconstruction of the simulation is 0.14, which is acceptable.

The third phantom tests the velocity field when the irrotational component cannot be ignored. The relative image error increases to 0.16 in this case, and the reconstruction accuracy is slightly affected by the irrotational component, since the source-free component is much larger than the irrotational vector field by a factor of 10. This shows the potential of acoustic travel-time tomography, that it can be robust against the irotational wind velocity components be used for the horizontal slice of wind velocity in the stratified atmosphere, where the wind velocity is a 2D source-free vector field.

Generally, for the reconstruction of all three phantoms, the orientation of the recovered fields are similar to the correct field with very few small deviations and the same can be said about the magnitude when the additive measurement noise is not prominent. Specifically, the last case which is the most challenging has practical importance because it corresponds to the real horizontal slicing image of the wind velocity field.

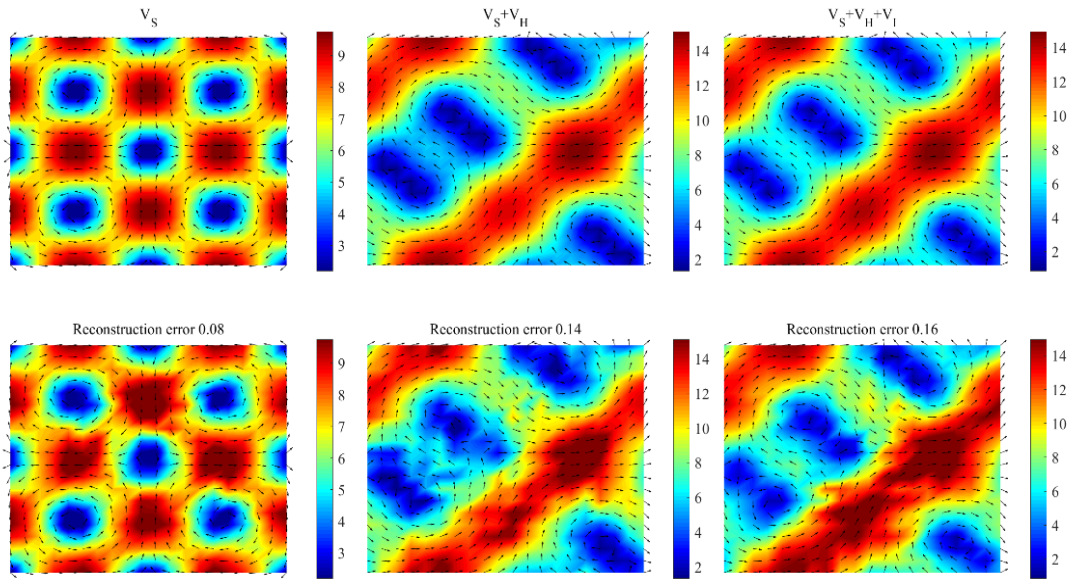

Figure 6-10: Simulation scenarios (first row) and reconstructed wind velocity fields (second row). The arrows represent the direction of the wind and the colours indicate its amplitude (m/s).

To evaluate the noise tolerance of the proposed method, measurements with different noise levels are used in the simulation. The averaged reconstruction error under different SNR condition is plotted in Figure 6-11. From the figure, it can be concluded the proposed method has a better noise tolerance for the first phantom of the solenoidal vector field than the other two phantoms. The irrotational vector field v_I will largely affect the reconstruction accuracy, especially for the low SNR cases. Besides, it should be noted that the harmonic vector field v_H, which is both divergence-free and curl-free, behaves like v_I and disturbs the reconstruction accuracy when the SNR is low. But when the SNR is larger than 45dB, the harmonic vector field v_H act as the solenoidal vector

field and reconstruction error is close to the error rate of the pure solenoidal vector field.

In summary, the simulation results confirmed the performance of the proposed divergence-free vector field reconstruction under practical setup. The proposed method can generate high quality tomographic images especially for the applications requiring good spatial resolution and enhanced noise deduction performance. Although it aims to reconstruct the divergence-free wind velocity field, results show that the relatively small irrotational component will not affect the reconstruction accuracy too much.

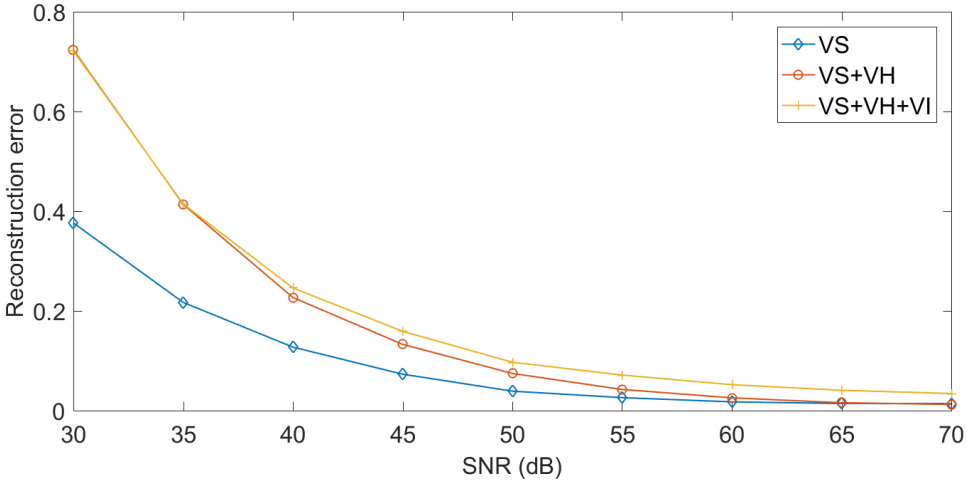

Figure 6-11: Evolution of reconstruction error with respect to different noise level

6.5.3 Reconstruction of votex shedding wind velocity field

Wind energy has become one of the fastest-growing renewable energy sources in the world for its cost-effective and environmental-friendly nature. As wind turbines are being installed at an ever-increasing rate today, power production optimisation and turbine reliability assessments have raised a growing demand for monitoring the wind velocity for the whole rotor blade area. Therefore, a novel wind velocity monitoring technique such as the acoustic tomography is highly desirable and will prove to be beneficial for wind energy systems.

In low turbulence, the tall wind turbine will create the Kármán Vortex Street due to the vortex shedding process, if the structure is uniform along its height. For the conventional wind turbine, the vortex shedding wind velocity field will affect the wake process and cause periodically varying aerodynamic loads on the blade structure of the turbines behind. In case of a severe resonance situation, extreme and destructive blade deflections might occur. For the bladeless turbine, it directly harnesses wind energy from the vortex shedding wind velocity field. Generally, knowing the vortex wind velocity field is of great importance for wind energy systems, because it can help to estimate working efficiency and assess the working risk in response to wind conditions more precisely. An example of the vortex shedding wind velocity field after a cylinder is shown in Figure 6-12, which is calculated using the Gerris Flow Solver's Kármán vortex street example[115].

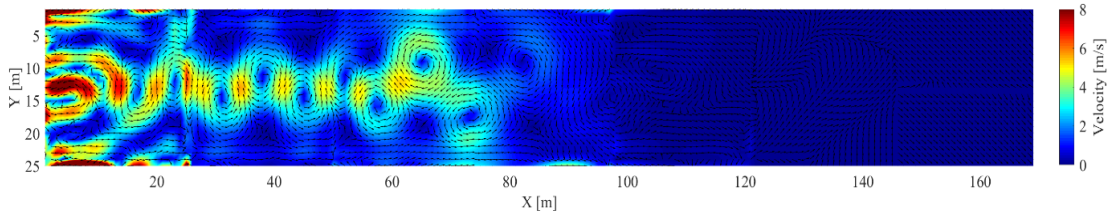

Figure 6-12: The simulated shedding vortex velocity field behind a cylinder with 2 m radius. The cylinder is placed outside the acoustic sensing area at the position [-4,13]. This 2D wind velocity is calculated using the Gerris Flow Solver.

In this simulation, the proposed vector field reconstruction algorithm is evaluated for the vortex shedding wind velocity field based on the setup illustrated in Figure 6-1. The original wind velocity field was split into 7 subfield frames for reconstruction, each covers a 25 m*25 m square area. This section bypasses the TOF estimation process and focuses on the vector field reconstruction. The TOFs are directly calculated using the line integrals of the wind velocity with a finer mesh, and then deliberately corrupted with additive white Gaussian noise. Then the proposed divergence-free vector field reconstruction method is applied, and the reconstruction quality is evaluated

by looking at the IE between the true and reconstructed sound speed distributions.

The reconstruction for all 7 frames are shown in Figure 6-13, Figure 6-14, and Figure 6-15. The corresponding measurement noise levels are set to be 40 dB. Generally, for the first 6 frames, the reconstructed wind velocity field successfully recovers the general structure of the original field. Especially for the middle frames from frame 2 to frame 5, the vortex is reconstructed with good quantitative accuracy. Large reconstruction error occurs in frames 1 and 7. For the frame 1, the original wind velocity field contains a lot of details that cannot be resolved by the 16-transducer sensing array. Increasing the transducer number from 16 to 32 will improve the reconstruction quality, as shown in Figure 6-16. For the frame 6 and 7, the original wind velocity field is mostly the harmonic and irrotational vector field, which is very difficult to reconstruct using the simulated TOFs.

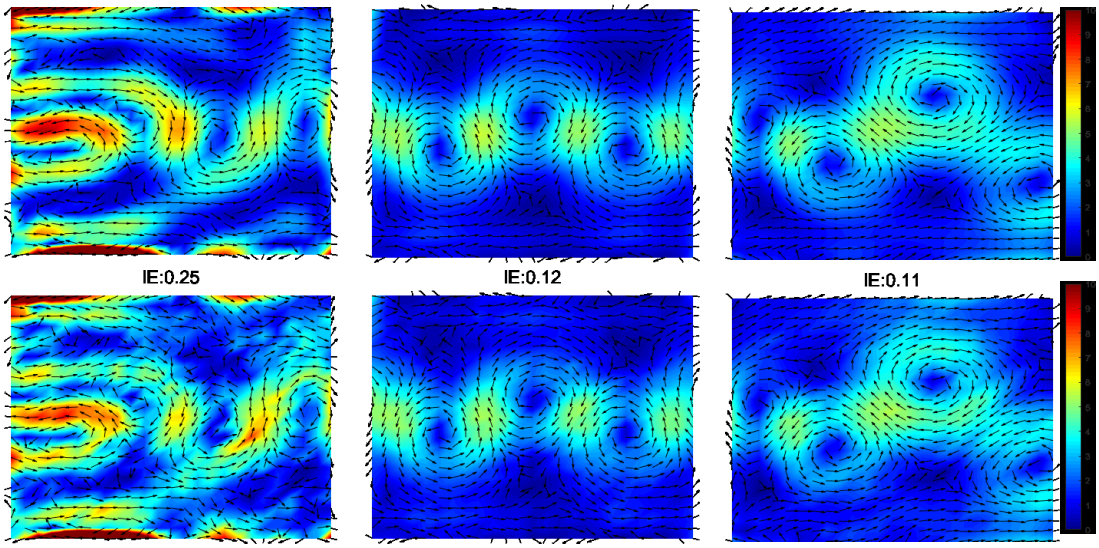

Figure 6-13: The original (first row) and the reconstructed (second row) velocity field for the first three frames. From left to right are the frames 1, 2 and 3.

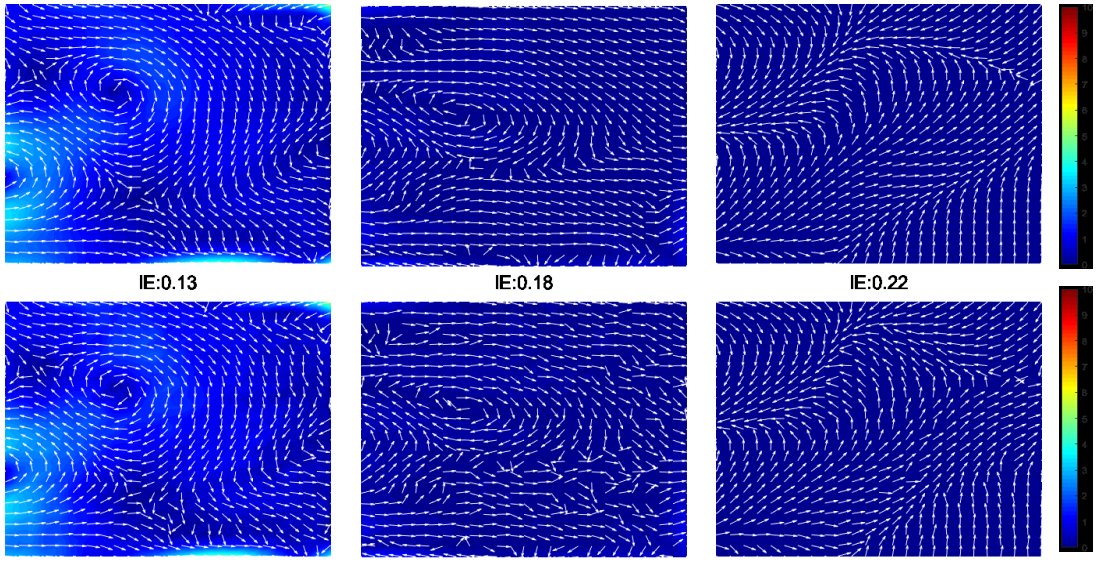

Figure 6-14: The original (first row) and the reconstructed (second row) velocity field for the middle three frames. From left to right are the frames 4, 5 and 6.

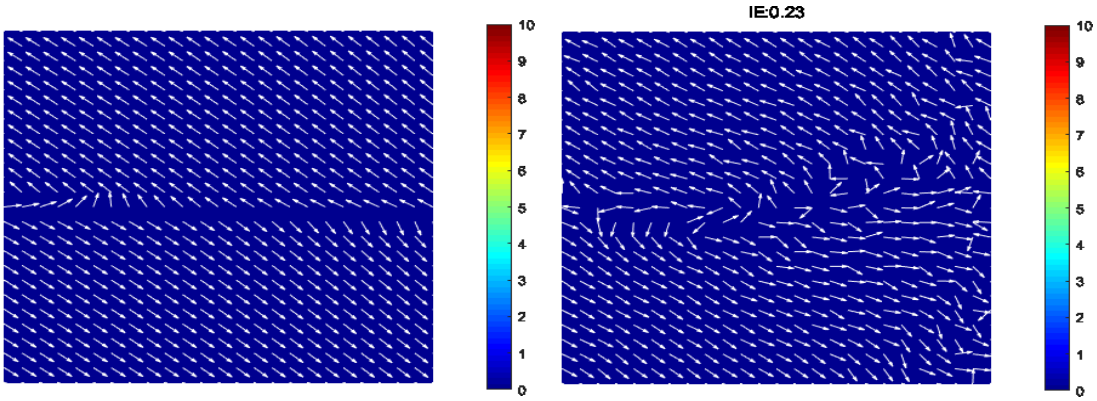

Figure 6-15: The original (left) and the reconstructed (right) velocity field for the last frames.

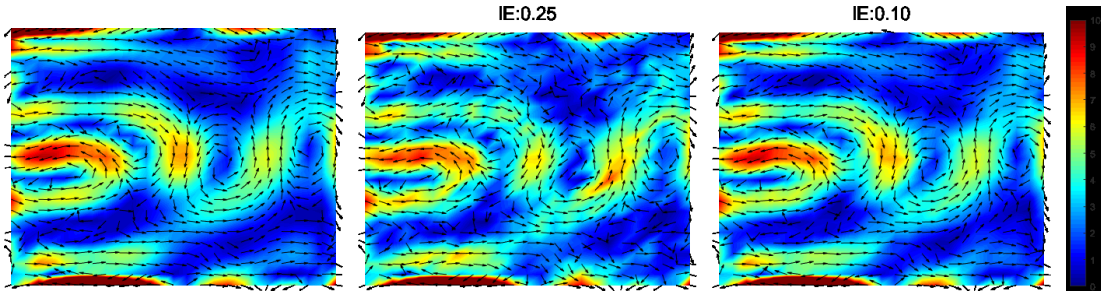

Figure 6-16: The original wind velocity field of frame 1 (left), reconstruction using 16-transducer array (middle) and reconstruction using 32-transducer array (left)

To evaluate the noise tolerance of the proposed method, measurements at different noise level is used in the simulation. The averaged reconstruction error under different SNR condition is plotted in Figure 6-17. It can be seen from the figure that the reconstruction results for frames 2, 3, 4 and 5 are much better compared to the other three frames for all noise levels. An interesting case is frame 5, which has a relatively large IE when the measurement SNR is low but a significant improvement in IE with higher a TOF measurement SNR. This is due to the harmonic component within the wind velocity field, which agrees with the conclusion of previous simulation.

In summary, acoustic tomography using the proposed divergence-free vector field reconstruction method has the capability to recover the shedding vortex wind velocity field from the TOF measurements with good quantitative accuracy for most cases. However, there are limitations in the cases: (1) the wind velocity field contains a lot of details that cannot be resolved with a limited number of transducers; (2) the wind velocity field may contain an irrotational vector component, which largely affects the reconstruction accuracy; and (3) the wind velocity field may contain a large harmonic vector component which will also affect the reconstruction accuracy when low SNR measurements are used.

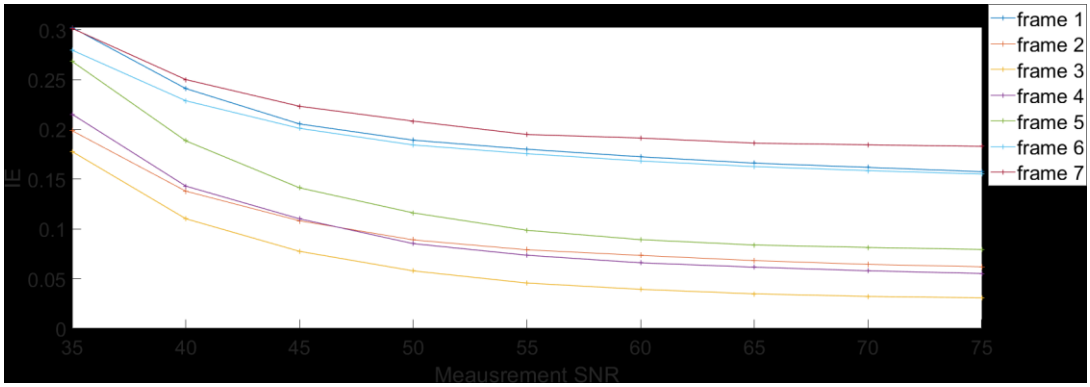

Figure 6-17: Evolution of reconstruction error with respect to different noise level

6.6 Summary

This chapter investigates the large scale acoustic tomography for wind velocity monitoring. Specifically, the 2D horizontal wind velocity of the near surface atmosphere. For this purpose, two approaches are presented: (1) reduction of processing time of TOF estimation; and (2) improving the reconstruction accuracy of the wind velocity field. For the first approach, the TOF measuring process for different paths is performed simultaneously based on cross-correlation detection using code division techniques. For the wind velocity reconstruction, the inverse problem is modelled with a divergence-free and vector Laplacian regularisation, which efficiently utilises the underlying divergence-free and smoothness property of the horizontal wind velocity field. ADMM is used to solve the inverse problem with good quantitative accuracy. Simulation results show that, for the 2D horizontal wind velocity field, the proposed reconstruction method has a good quantitative accuracy by utilizing the divergence-free property.

Chapter 7 Conclusions and future work

7.1 Conclusions

Whist challenging, acoustic tomography is a promising sensing technique for atmospheric imaging with the advantages of being non-invasive, low-cost, and easy to implement. Acoustic tomography also has benefit of being able to simultaneously measure the air temperature and the wind velocity. The key challenges include obtaining an accurate TOF estimation, using an appropriate imaging temporal and spatial resolution, and the quantitative accuracy of reconstruction. Aiming at exploiting acoustic tomography for the atmospheric imaging of temperature and wind velocity fields, a comprehensive study was carried out by developing a lab-scale acoustic tomography system, investigating a TOF estimation algorithm, and designing a tomographic image reconstruction algorithm. The detailed work, contributed by this thesis, is summarised as follows:

The foundations of acoustic tomography, the existing acoustic tomography systems for atmospheric imaging, the state-of-the-art acoustic tomography reconstruction algorithms, and the emerging applications of acoustic tomography, were firstly reviewed. The review helped to build understanding of recent developments in acoustic tomography systems and provided the background for the innovative work demonstrated in this thesis.

The primary target of this thesis was to develop a lab-scale acoustic tomography system and further, develop a robust and accurate TOF estimation algorithm. The design of the acoustic tomography system was illustrated from the perspectives of the system architecture and the functional modules. The key features of the presented system include: (1) 192 TOFs per frame using the array of 16 transmitters and 16 receivers; (2) a semi-parallel data acquisition scheme using a switching circuit; (3) configurable excitation signal generation and received waveform measurement using the NI DAQ; and

(4) a central control software for system control, received waveform monitoring and data storage. In addition, a PCAIC TOF estimation method was developed. Two improvements were studied in comparison with conventional weighted AIC TOF estimation methods to reduce cross-talk interference and sound reflections: (1) an adaptive window was applied for accurate AIC TOF estimation; and (2) a phase correction method was developed to further improve the temporal resolution and noise robustness of the TOF estimation. Experimental study shows that the proposed PCAIC picker has good quantitative accuracy (with an overall rRMSE of less than 0.2%), high temporal resolution (0.25 μs) and robustness against the crosstalk interference and additional random noise. In summary, the acoustic tomography system and PCAIC TOF estimation method can be used to perform a lab-scale experimental study and validate different tomographic reconstruction algorithms.

This thesis also worked on the improvement of the temporal resolution of acoustic tomography. A novel online time-resolved reconstruction method was proposed, which was able to reconstruct high quality time-resolved images by using fewer TOFs per frame. This method exploits the redundancy of information in the temporal domain and designs a temporal regularisation based on an adaptive AR model to reduce the required amount of TOF data per frame. A sliding overlapping window is applied to further improve the reconstruction accuracy Instead of conducting iterative calculation upon each data set until convergence, the recursive reconstruction process performs a sliding iteration over each data segment. For the reconstruction of each frame, the online computation is non-iterative. Based on the simulation results, the proposed OTRR methods have a higher quantitative accuracy, a faster convergence rate and better noise robustness compared to the conventional Kalman filter reconstruction method. From the experiments, the OTRR method provides satisfactory results in tracking the dynamic changes of the temperature field.

Moreover, another novel image reconstruction method named NCGD was presented. Instead of the commonly used straight ray model, this method uses the bent ray model to reduce the modelling error when the temperature field has a large gradient. During the reconstruction process, both the sound propagation ray paths and temperature distribution can be reconstructed iteratively from the TOFs. The reconstruction process of NCGD consists of two parts: (1) the nonlinear conjugate gradient descent method to efficiently update the solution of the temperature field; and (2) the FMM to update the corresponding ray path given the temperature field estimation. Numerical simulations have been carried out to validate the performance of the proposed method. Compared to the conventional SIRT method using the straight ray model, the proposed NCGD method has better performance in terms of the overall image quality, less distortion in the shape of the heated area, and the quantitative accuracy of the peak value and the heat centre location. Compared to the common NGD methods using the bent ray model, the proposed NCGD method has the advantages of using less computational time, better noise tolerance and better image quality.

Thereafter this thesis continued with the study of applying acoustic tomography for large scale atmospheric imaging. To accelerate the data collection process, a parallel TOF measurement scheme was investigated, including the cross-correlation TOF estimation and the design of an orthogonal waveform set for the excitation signal based on the filtered and modulated Kasami sequence. Besides, a novel vector tomography reconstruction method was developed for the reconstruction of the wind velocity field. It efficiently uses the divergence-free property of the 2D horizontal wind velocity field as the *priori* knowledge and formulates the inverse problem with the divergence-free regularisation and vector Laplacian regularisation for enhanced imaging performance. In order to solve the problem with a faster convergence rate, an accelerated alternating direction method of multipliers was applied. Simulation results show that the proposed reconstruction method has a good quantitative accuracy to reconstruct the 2D horizontal wind velocity field.

In conclusion, the methodologies developed in this thesis are very promising for enhancing the performance of acoustic tomography system, in terms of improving the TOF estimation accuracy and noise robustness using PCAIC TOF estimation method, improving the temporal resolution with the OTRR method, improving the image quality of large gradient temperature field using NCGD method, improving the image quality of 2D horizontal wind velocity field using the divergence-free regularised reconstruction method. There are also many further extensions and potential applications of these methods, which will be discussed in the next section.

7.2 Future work

Although this thesis has significantly improved the performance of acoustic tomography imaging with the developed techniques, investigation is still necessary to further advance this work in the following areas

- With regards to the development of the acoustic tomography system, an improvement in the sampling frequency is worth studying. Currently, the 12 received waveforms are measured in two groups. A higher sampling rate would enable simultaneous data collection for all the received waveforms. Recording the received waveforms in each channel using a higher sampling rate would also help to improve the TOF estimation accuracy.

- With regards to the transducer array, multiple acoustic transceivers should be used instead of standalone transmitters and receivers. For each transmitter, its corresponding receiver can be put nearby. However, the transmitter and the receiver cannot be considered to be at the same position for small scale experiments (1 m^2 sensing area in this thesis). If each transmitter is at a different position compared to its corresponding receiver, then the back and forth sound propagations are along different ray paths. The use of transceivers enables reciprocal transmission of acoustic waves along the same ray path, and the time difference of the back and forth TOFs can be used for wind velocity

reconstruction.

- As for the image reconstruction method based on the bent ray model, the presented NCGD method cannot provide good reconstruction on the complex temperature field. This is due to the lack of measurements. The spatial resolution of the reconstructed image is limited by the number of TOFs. The ray tracing accuracy will also be affected if the ray paths are computed based on an under-sampled sound speed distribution. Currently, the spatial resolution is just enough for the simple temperature fields, like the tested phantoms in Chapter 5. One way to solve this problem is to increase the number of TOFs by placing more transducers on the boundary. However, this will add to the implementation difficulty and the equipment cost. Another possible way to solve this problem is to incorporate appropriate information from the *priori* knowledge about the specific temperature field or the measurement information from other techniques.

- The focus of this thesis has been to enhance the performance of acoustic tomography for atmospheric imaging, but these ideas are also applicable beyond this scope. The PCAIC TOF estimation methods can also be used for other applications, such as ocean tomography, ultrasound tomography for medical uses, arrival time estimation for seismic imaging, and ultrasound range detection. The OTRR method can also be used for reconstruction in other dynamic imaging applications, for instance, the 4D CT [116] and dynamic MRI [73].

- Finally, there is a need to extend the presented work for 3D imaging. With the use of multiple layers of transducer arrays, high throughput data acquisition hardware, and fast tomographic reconstruction algorithms, 3D tomographic images of atmospheric volumes can be obtained. 3D tomographic imaging can provide full knowledge of atmospheric volumes in the form of temperature profiles and wind velocity vectors. For instance, accurate 3D temperature profiles would

help to improve the understanding of the combustion process and help to ease the evaluation of combustion efficiency.

References

[1] I. Jovanovic, "Inverse problems in acoustic tomography," 2008.

[2] M. Collins and W. Kuperman, "Inverse problems in ocean acoustics," *Inverse Problems,* vol. 10, p. 1023, 1994.

[3] N. Taniguchi, C.-F. Huang, A. Kaneko, C.-T. Liu, B. M. Howe, Y.-H. Wang*, et al.*, "Measuring the Kuroshio Current with ocean acoustic tomography," *The Journal of the Acoustical Society of America,* vol. 134, pp. 3272-3281, Oct 2013.

[4] T. Wang and W. Xu, "Sparsity-based approach for ocean acoustic tomography using learned dictionaries," in *OCEANS 2016-Shanghai*, 2016, pp. 1-6.

[5] W. Munk and C. Wunsch, "Ocean acoustic tomography: a scheme for large scale monitoring," *Deep Sea Research Part A, Oceanographic Research Papers,* vol. 26, pp. 123-161, 1979.

[6] R. Brossier, S. Operto, and J. Virieux, "Seismic imaging of complex onshore structures by 2D elastic frequency-domain full-waveform inversion," *Geophysics,* vol. 74, pp. XWCC105-WCC118, 2009.

[7] C. Li, N. Duric, P. Littrup, and L. Huang, "In vivo breast sound-speed imaging with ultrasound tomography," *Ultrasound in Medicine and Biology,* vol. 35, pp. 1615-1628, Oct 2009.

[8] C. Li, L. Huang, N. Duric, H. Zhang, and C. Rowe, "An improved automatic time-of-flight picker for medical ultrasound tomography," *Ultrasonics,* vol. 49, pp. 61-72, Jan 2009.

[9] O. Roy, I. Jovanović, A. Hormati, R. Parhizkar, and M. Vetterli, "Sound speed estimation using wave-based ultrasound tomography: theory and GPU implementation," in *SPIE Medical Imaging*, 2010, pp. 76290J-76290J-12.

[10] I. Toši, I. Jovanovi, P. Frossard, M. Vetterli, and N. Duri, "Ultrasound tomography with learned dictionaries," in *2010 IEEE International Conference on Acoustics, Speech and Signal Processing*, 2010, pp. 5502-5505.

[11] X. Qu, T. Azuma, H. Imoto, R. Raufy, H. Lin, H. Nakamura*, et al.*, "Novel automatic first-arrival picking method for ultrasound sound-speed tomography," *Japanese Journal of Applied Physics,* vol. 54, p. 07HF10, Jun 2015.

[12] X. Wang, J. Wiedenbeck, and S. Liang, "Acoustic tomography for decay detection in black cherry trees," *Wood and Fiber Science,* vol. 41, pp. 127-137, 2009.

[13] H. Yan, G. Chen, Y. Zhou, and L. Liu, "Primary study of temperature distribution measurement in stored grain based on acoustic tomography," *Experimental Thermal and Fluid Science,* vol. 42, pp. 55-63, Oct 2012.

[14] E. F. Cox, "Abnormal Audibility Zones in Long Distance Propagation through the Atmosphere," *Journal of the Acoustical Society of America,* vol. 21, pp. 6-16, 1949.

[15] I. P. Chunchuzov, G. A. Bush, and S. N. Kulichkov, "On acoustical impulse propagation in a moving inhomogeneous atmospheric layer," *Journal of the Acoustical Society of America,* vol. 88, pp. 455-461, 1990.

[16] D. Keith Wilson and D. W. Thomson, "Acoustic tomographic monitoring of the atmospheric surface layer," *Journal of Atmospheric and Oceanic Technology,* vol. 11, pp. 751-769, 1994.

[17] A. Ziemann, K. Arnold, and A. Raabe, "Acoustic tomography in the atmospheric surface layer," in *Annales Geophysicae*, 1998, pp. 139-148.

[18] P. Holstein, A. Raabe, R. Müller, M. Barth, D. Mackenzie, and E. Starke, "Acoustic tomography on the basis of travel-time measurement," *Measurement Science and Technology,* vol. 15, p. 1420, Jun 2004.

[19] M. Barth and A. Raabe, "Acoustic tomographic imaging of temperature and flow fields in air," *Measurement Science and Technology,* vol. 22, p. 035102, Jan 2011.

[20] S. Liu, S. Liu, and T. Ren, "Acoustic Tomography Reconstruction Method for the Temperature Distribution Measurement," *IEEE Transactions on Instrumentation and Measurement,* 2017.
[21] H. Yan, Z. Ma, and Y. G. Zhou, "Acoustic tomography system for online monitoring of temperature fields," *IET Science, Measurement & Technology,* 2017.
[22] M. Bramanti, E. A. Salerno, A. Tonazzini, S. Pasini, and A. Gray, "An acoustic pyrometer system for tomographic thermal imaging in power plant boilers," *IEEE Transactions on Instrumentation and Measurement,* vol. 45, pp. 159-167, 1996.
[23] S. Zhang, G. Shen, L. An, and G. Li, "Ash fouling monitoring based on acoustic pyrometry in boiler furnaces," *Applied Thermal Engineering,* vol. 84, pp. 74-81, 2015.
[24] S. Zhang, G. Shen, L. An, and Y. Niu, "Online monitoring of the two-dimensional temperature field in a boiler furnace based on acoustic computed tomography," *Applied thermal engineering,* vol. 75, pp. 958-966, 2015.
[25] Y. Yong, Q. Tian, L. Gang, M. M. Hossain, G. Gilabert, and L. Shi, "Recent advances in flame tomography," *Chinese Journal of Chemical Engineering,* vol. 20, pp. 389-399, Apr 2012.
[26] R. Sheh, N. Jamali, M. W. Kadous, and C. Sammut, "A low-cost, compact, lightweight 3d range sensor," in *Australian Conference on Robotics and Automation*, 2006.
[27] V. E. Ostashev and D. K. Wilson, *Acoustics in moving inhomogeneous media*: CRC Press, 2015.
[28] A. Ziemann, K. Arnold, and A. Raabe, "Acoustic tomography as a method to identify small-scale land surface characteristics," *Acta Acustica united with Acustica,* vol. 87, pp. 731-737, 2001.
[29] A. Hormati, I. Jovanovic, O. Roy, and M. Vetterli, "Robust ultrasound travel-time tomography using the bent ray model," in *Proc. SPIE*, 2010, p. 76290I.
[30] V. E. Ostashev, S. N. Vecherin, K. D. Wilson, A. Ziemann, and G. H. Goedecke, "Recent progress in acoustic travel-time tomography of the atmospheric surface layer," *Meteorologische Zeitschrift,* vol. 18, pp. 125-133, 2009.
[31] S. Green, "Acoustic temperature and velocity measurement in combustion gases," in *Eight International Heat Transfer Conference*, 1986.
[32] I. Jovanovic, L. Sbaiz, and M. Vetterli, "Acoustic tomography method for measuring temperature and wind velocity," in *2006 IEEE International Conference on Acoustics Speech and Signal Processing Proceedings*, 2006, pp. IV-IV.
[33] H. Yan, Z. Peng, K. Cui, and L. Zhang, "Acoustic travel-time measurement in acoustic temperature field monitoring," in *Intelligent Control and Automation, 2008. WCICA 2008. 7th World Congress on*, 2008, pp. 4947-4951.
[34] T. Wiens and P. Behrens, "Turbulent flow sensing using acoustic tomography," *Proceedings of Innovations in practical Noise Control,* vol. 2009, Aug 2009.
[35] S. Kolouri, M. R. Azimi-Sadjadi, and A. Ziemann, "A statistical-based approach for acoustic tomography of the atmosphere," *The Journal of the Acoustical Society of America,* vol. 135, pp. 104-114, 2014.
[36] C. Medina, J. C. Segura, and A. De la Torre, "Ultrasound indoor positioning system based on a low-power wireless sensor network providing sub-centimeter accuracy," *Sensors,* vol. 13, pp. 3501-3526, Mar 2013.
[37] J. Qi and G.-P. Liu, "A Robust High-Accuracy Ultrasound Indoor Positioning System Based on a Wireless Sensor Network," *Sensors,* vol. 17, p. 2554, Nov 2017.
[38] R. Demirli and J. Saniie, "Model-based estimation of ultrasonic echoes. Part I: Analysis and algorithms," *IEEE transactions on ultrasonics, ferroelectrics, and frequency control,* vol. 48, pp. 787-802, May 2001.

[39] Q. Han, P. Wang, and H. Zheng, "Modified ultrasonic time-of-flight diffraction testing with Barker code excitation for sizing inclined crack," *Applied Acoustics,* vol. 140, pp. 153-159, Nov 2018.
[40] Z. Lu, C. Yang, D. Qin, Y. Luo, and M. Momayez, "Estimating ultrasonic time-of-flight through echo signal envelope and modified Gauss Newton method," *Measurement,* vol. 94, pp. 355-363, Dec 2016.
[41] A. Egaña, F. Seco, and R. Ceres, "Processing of ultrasonic echo envelopes for object location with nearby receivers," *IEEE Transactions on Instrumentation and Measurement,* vol. 57, pp. 2751-2755, Dec 2008.
[42] M. R. Hoseini, X. Wang, and M. J. Zuo, "Estimating ultrasonic time of flight using envelope and quasi maximum likelihood method for damage detection and assessment," *Measurement,* vol. 45, pp. 2072-2080, Oct 2012.
[43] M. Withers, R. Aster, C. Young, J. Beiriger, M. Harris, S. Moore*, et al.*, "A comparison of select trigger algorithms for automated global seismic phase and event detection," *Bulletin of the Seismological Society of America,* vol. 88, pp. 95-106, Feb 1998.
[44] C. D. Saragiotis, L. J. Hadjileontiadis, I. T. Rekanos, and S. M. Panas, "Automatic P phase picking using maximum kurtosis and/spl kappa/-statistics criteria," *IEEE Geoscience and Remote Sensing Letters,* vol. 1, pp. 147-151, Jul 2004.
[45] L. Han, J. Wong, and J. Bancroft, "Time picking and random noise reduction on microseismic data," *CREWES Research Reports,* vol. 21, pp. 1-13, 2009.
[46] J. I. Sabbione and D. Velis, "Automatic first-breaks picking: New strategies and algorithms," *Geophysics,* vol. 75, pp. V67-V76, Jul 2010.
[47] F. Li*, J. Rich, K. J. Marfurt, and H. Zhou, "Automatic event detection on noisy microseismograms," in *SEG Technical Program Expanded Abstracts 2014*, ed: Society of Exploration Geophysicists, 2014, pp. 2363-2367.
[48] H. Zhang, C. Thurber, and C. Rowe, "Automatic P-wave arrival detection and picking with multiscale wavelet analysis for single-component recordings," *Bulletin of the Seismological Society of America,* vol. 93, pp. 1904-1912, Oct 2003.
[49] J. Akram, D. Eaton, and A. S. Onge, "Automatic event-detection and time-picking algorithms for downhole microseismic data processing," in *4th EAGE Passive Seismic Workshop*, 2013.
[50] R. Sleeman and T. Van Eck, "Robust automatic P-phase picking: an on-line implementation in the analysis of broadband seismogram recordings," *Physics of the earth and planetary interiors,* vol. 113, pp. 265-275, Jun 1999.
[51] N. Maeda, "A method for reading and checking phase times in autoprocessing system of seismic wave data," *Zisin,* vol. 38, pp. 365-379, 1985.
[52] N. Polydorides, S.-A. Tsekenis, H. McCann, V.-D. Prat, and P. Wright, "An efficient approach for limited-data chemical species tomography and its error bounds," *Proceedings of the Royal Society A: Mathematical, Physical and Engineering Sciences,* vol. 472, p. 20150875, 2016.
[53] A. Ziemann, K. Arnold, and A. Raabe, "Acoustic tomography as a remote sensing method to investigate the near-surface atmospheric boundary layer in comparison with in situ measurements," *Journal of Atmospheric and Oceanic Technology,* vol. 19, pp. 1208-1215, 2002.
[54] T. Wiens and P. Behrens, "Turbulent flow sensing using acoustic tomography," in *INTER-NOISE and NOISE-CON Congress and Conference Proceedings*, 2009, pp. 336-344.
[55] Y. Liu, S. Liu, J. Lei, J. Liu, H. I. Schlaberg, and Y. Yan, "A method for simultaneous reconstruction of temperature and concentration distribution in gas mixtures based on acoustic tomography," *Acoustical Physics,* vol. 61, pp. 597-605, 2015.

[56] Y. Bao and J. Jia, "Nonlinear temperature field reconstruction using acoustic tomography," presented at the Imaging Systems and Techniques (IST), 2017 IEEE International Conference on, Beijing, 2017.
[57] H. Sielschott, "Measurement of horizontal flow in a large scale furnace using acoustic vector tomography," *Flow measurement and instrumentation,* vol. 8, pp. 191-197, Apr 1997.
[58] Y.-Q. Li and H.-C. Zhou, "Experimental study on acoustic vector tomography of 2-D flow field in an experiment-scale furnace," *Flow Measurement and Instrumentation,* vol. 17, pp. 113-122, Apr 2006.
[59] T. Wiens, "Ray Tracing Using Radial Basis Function Networks," *Journal of Vibration and Acoustics,* vol. 138, p. 024502, 2016.
[60] I. Jovanovic, A. Hormati, L. Sbaiz, and M. Vetterli, "Efficient and stable acoustic tomography using sparse reconstruction methods," in *19th International Congress on Acoustics*, 2007.
[61] I. Jovanovic, L. Sbaiz, and M. Vetterli, "Acoustic tomography for scalar and vector fields: theory and application to temperature and wind estimation," *Journal of Atmospheric and Oceanic Technology,* vol. 26, pp. 1475-1492, 2009.
[62] Y. Bao, J. Jia, and N. Polydorides, "Real-time temperature field measurement based on acoustic tomography," *Measurement Science and Technology,* vol. 28, p. 074002, Jun 2017.
[63] P. C. Hansen, *Discrete inverse problems: insight and algorithms* vol. 7: Siam, 2010.
[64] Y. Yang, J. Jia, N. Polydorides, and H. McCann, "Effect of structured packing on EIT image reconstruction," in *2014 IEEE International Conference on Imaging Systems and Techniques (IST) Proceedings*, 2014, pp. 53-58.
[65] R. van Sloun, A. Pandharipande, M. Mischi, and L. Demi, "Compressed sensing for ultrasound computed tomography," *IEEE Transactions on Biomedical Engineering,* vol. 62, pp. 1660-1664, 2015.
[66] M. A. Figueiredo, R. D. Nowak, and S. J. Wright, "Gradient projection for sparse reconstruction: Application to compressed sensing and other inverse problems," *IEEE Journal of selected topics in signal processing,* vol. 1, pp. 586-597, 2007.
[67] S.-J. Kim, K. Koh, M. Lustig, S. Boyd, and D. Gorinevsky, "An Interior-Point Method for Large-Scale l1-Regularized Least Squares," *IEEE journal of selected topics in signal processing,* vol. 1, pp. 606-617, 2007.
[68] P. L. Combettes and V. R. Wajs, "Signal recovery by proximal forward-backward splitting," *Multiscale Modeling & Simulation,* vol. 4, pp. 1168-1200, 2005.
[69] I. Daubechies, M. Defrise, and C. De Mol, "An iterative thresholding algorithm for linear inverse problems with a sparsity constraint," *Communications on Pure and Applied Mathematics: A Journal Issued by the Courant Institute of Mathematical Sciences,* vol. 57, pp. 1413-1457, 2004.
[70] A. Beck and M. Teboulle, "A Fast Iterative Shrinkage-Thresholding Algorithm for Linear Inverse Problems," *SIAM J. Img. Sci.,* vol. 2, pp. 183-202, 2009.
[71] S. Becker, J. Bobin, and E. J. Candès, "NESTA: A fast and accurate first-order method for sparse recovery," *SIAM Journal on Imaging Sciences,* vol. 4, pp. 1-39, 2011.
[72] J. Yang and Y. Zhang, "Alternating direction algorithms for l1-problems in compressive sensing," *SIAM journal on scientific computing,* vol. 33, pp. 250-278, 2011.
[73] S. G. Lingala, Y. Hu, E. DiBella, and M. Jacob, "Accelerated dynamic MRI exploiting sparsity and low-rank structure: kt SLR," *IEEE transactions on medical imaging,* vol. 30, pp. 1042-1054, May 2011.
[74] H. Rauhut, R. Schneider, and Z. Stojanac, "Low rank tensor recovery via iterative hard thresholding," *arXiv preprint arXiv:1602.05217,* 2016.

[75] S. N. Vecherin, V. E. Ostashev, G. H. Goedecke, D. K. Wilson, and A. G. Voronovich, "Time-dependent stochastic inversion in acoustic travel-time tomography of the atmosphere," *The Journal of the Acoustical Society of America,* vol. 119, pp. 2579-2588, 2006.
[76] S. N. Vecherin, V. E. Ostashev, A. Ziemann, D. K. Wilson, K. Arnold, and M. Barth, "Tomographic reconstruction of atmospheric turbulence with the use of time-dependent stochastic inversion," *The Journal of the Acoustical Society of America,* vol. 122, pp. 1416-1425, 2007.
[77] S. Kolouri, M. R. Azimi-Sadjadi, and A. Ziemann, "Acoustic tomography of the atmosphere using unscented Kalman filter," *IEEE Transactions on Geoscience and Remote Sensing,* vol. 52, pp. 2159-2171, 2014.
[78] J. Kaipio and E. Somersalo, *Statistical and computational inverse problems* vol. 160: Springer Science & Business Media, 2006.
[79] M. Soleimani, M. Vauhkonen, W. Yang, A. Peyton, B. S. Kim, and X. Ma, "Dynamic imaging in electrical capacitance tomography and electromagnetic induction tomography using a Kalman filter," *Measurement Science and Technology,* vol. 18, p. 3287, Sep 2007.
[80] R. Gerhard Pratt, L. Huang, N. Duric, and P. Littrup, "Sound-speed and attenuation imaging of breast tissue using waveform tomography of transmission ultrasound data," in *Progress in Biomedical Optics and Imaging - Proceedings of SPIE*, 2007.
[81] M. Pérez-Liva, J. Herraiz, J. Udías, E. Miller, B. Cox, and B. Treeby, "Time domain reconstruction of sound speed and attenuation in ultrasound computed tomography using full wave inversion," *The Journal of the Acoustical Society of America,* vol. 141, pp. 1595-1604, 2017.
[82] N. Duric, C. Li, O. Roy, and S. Schmidt, "Acoustic tomography: promise versus reality," in *2011 IEEE International Ultrasonics Symposium*, 2011, pp. 2033-2041.
[83] C. Dong, Y. Jin, M. Ferrara, and K. Priddy, "A study of multi-static ultrasonic tomography using propagation and back-propagation method," in *SPIE Defense, Security, and Sensing*, 2011, pp. 805106-805106-13.
[84] C. Dong and Y. Jin, "MIMO nonlinear ultrasonic tomography by propagation and backpropagation method," *IEEE Transactions on Image Processing,* vol. 22, pp. 1056-1069, 2013.
[85] R. G. Pratt, "Seismic waveform inversion in the frequency domain, Part 1: Theory and verification in a physical scale model," *GEOPHYSICS,* vol. 64, pp. 888-901, 2019.
[86] L. Li, X. Wang, L. Wang, and R. B. Allison, "Acoustic tomography in relation to 2D ultrasonic velocity and hardness mappings," *Wood Science and Technology,* vol. 46, pp. 551-561, 2012.
[87] E.-J. Wagenmakers and S. Farrell, "AIC model selection using Akaike weights," *Psychonomic bulletin & review,* vol. 11, pp. 192-196, Feb 2004.
[88] I. J. Moon and S. H. Hong, "What is temporal fine structure and why is it important?," *Korean journal of audiology,* vol. 18, p. 1, Apr 2014.
[89] L. Svilainis, K. Lukoseviciute, V. Dumbrava, and A. Chaziachmetovas, "Subsample interpolation bias error in time of flight estimation by direct correlation in digital domain," *Measurement,* vol. 46, pp. 3950-3958, Dec 2013.
[90] D. Kazantsev, G. Van Eyndhoven, W. Lionheart, P. Withers, K. Dobson, S. McDonald*, et al.*, "Employing temporal self-similarity across the entire time domain in computed tomography reconstruction," *Phil. Trans. R. Soc. A,* vol. 373, p. 20140389, Jun 2015.
[91] Y. Li, S. Liu, and S. H. Inaki, "Dynamic Reconstruction Algorithm of Three-Dimensional Temperature Field Measurement by Acoustic Tomography," *Sensors,* vol. 17, p. 2084, Jun 2017.

[92] B. Chen, J. F. Abascal, and M. Soleimani, "Electrical Resistance Tomography for Visualization of Moving Objects Using a Spatiotemporal Total Variation Regularization Algorithm," *Sensors,* vol. 18, p. 1704, May 2018.
[93] Z. Tian, X. Jia, B. Dong, Y. Lou, and S. B. Jiang, "Low‐dose 4DCT reconstruction via temporal nonlocal means," *Medical physics,* vol. 38, pp. 1359-1365, Mar 2011.
[94] K. A. Mohan, S. Venkatakrishnan, J. W. Gibbs, E. B. Gulsoy, X. Xiao, M. De Graef*, et al.*, "TIMBIR: A method for time-space reconstruction from interlaced views," *IEEE Trans. Computational Imaging,* vol. 1, pp. 96-111, 2015.
[95] A. Majumdar and R. K. Ward, "Causal dynamic MRI reconstruction via nuclear norm minimization," *Magnetic resonance imaging,* vol. 30, pp. 1483-1494, Dec 2012.
[96] Z.-P. Liang, "Spatiotemporal imaging with partially separable functions," in *Biomedical Imaging: From Nano to Macro, 2007. ISBI 2007. 4th IEEE International Symposium on*, 2007, pp. 988-991.
[97] H. Pedersen, S. Kozerke, S. Ringgaard, K. Nehrke, and W. Y. Kim, "k‐t PCA: temporally constrained k‐t BLAST reconstruction using principal component analysis," *Magnetic resonance in medicine,* vol. 62, pp. 706-716, 2009.
[98] D. Liang, E. V. DiBella, R. R. Chen, and L. Ying, "k‐t ISD: dynamic cardiac MR imaging using compressed sensing with iterative support detection," *Magnetic resonance in medicine,* vol. 68, pp. 41-53, 2012.
[99] L. Kleeman, "Understanding and applying Kalman filtering."
[100] U. Sumbul, J. M. Santos, and J. M. Pauly, "A practical acceleration algorithm for real-time imaging," *IEEE transactions on medical imaging,* vol. 28, pp. 2042-2051, 2009.
[101] A. Tarantola, *Inverse problem theory and methods for model parameter estimation* vol. 89: siam, 2005.
[102] W. W. Hager and H. Zhang, "A survey of nonlinear conjugate gradient methods," *Pacific journal of Optimization,* vol. 2, pp. 35-58, 2006.
[103] M. S. Hassouna and A. A. Farag, "MultiStencils Fast Marching Methods: A Highly Accurate Solution to the Eikonal Equation on Cartesian Domains," *IEEE Transactions on Pattern Analysis and Machine Intelligence,* vol. 29, pp. 1563-1574, 2007.
[104] N. Andrei, "Open problems in nonlinear conjugate gradient algorithms for unconstrained optimization," *Bulletin of the Malaysian Mathematical Sciences Society,* vol. 34, 2011.
[105] M. Barth, G. Fischer, A. Raabe, A. Ziemann, and F. Weiße, "Remote sensing of temperature and wind using acoustic travel-time measurements," *Meteorologische Zeitschrift,* vol. 22, pp. 103-109, 2013.
[106] J. L. Spiesberger and K. M. Fristrup, "Passive localization of calling animals and sensing of their acoustic environment using acoustic tomography," *American Naturalist,* pp. 107-153, 1990.
[107] I. Chunchuzov, A. Otrezov, I. Petenko, V. Tovchigrechko, A. Svertilov, A. Fogel*, et al.*, "Travel-Time and Duration Fluctuations of Acoustic Pulses in the Atmospheric Boundary Layer," *Izv. Akad. Nauk, Fiz. Atmos. Okeana,* vol. 33, pp. 324-338, 1997.
[108] C. B. Hasager, A. Peña, M. B. Christiansen, P. Astrup, M. Nielsen, F. Monaldo*, et al.*, "Remote sensing observation used in offshore wind energy," *IEEE Journal of Selected Topics in Applied Earth Observations and Remote Sensing,* vol. 1, pp. 67-79, 2008.
[109] M. F. van Dooren, D. Trabucchi, and M. Kühn, "A Methodology for the Reconstruction of 2D Horizontal Wind Fields of Wind Turbine Wakes Based on Dual-Doppler Lidar Measurements," *Remote Sensing,* vol. 8, p. 809, 2016.

[110] C. Weitkamp, *Lidar: range-resolved optical remote sensing of the atmosphere* vol. 102: Springer Science & Business, 2006.
[111] S. J. Norton, "Unique tomographic reconstruction of vector fields using boundary data," *IEEE Transactions on image processing,* vol. 1, pp. 406-412, 1992.
[112] L. Welch, "Lower bounds on the maximum cross correlation of signals (corresp.)," *IEEE Transactions on Information theory,* vol. 20, pp. 397-399, 1974.
[113] M. Fukushima, "Application of the alternating direction method of multipliers to separable convex programming problems," *Computational Optimization and Applications,* vol. 1, pp. 93-111, 1992.
[114] R. J. Tibshirani, *The solution path of the generalized lasso*: Stanford University, 2011.
[115] *Gerris Flow Solver*. Available: http://gfs.sourceforge.net/wiki/index.php/Main_Page
[116] D. Kazantsev, E. Guo, A. Kaestner, W. R. Lionheart, J. Bent, P. J. Withers*, et al.*, "Temporal sparsity exploiting nonlocal regularization for 4D computed tomography reconstruction," *Journal of X-ray science and technology,* vol. 24, pp. 207-219, Jan 2016.